Development of a bioresorbable patch to treat aortic dissection

Noemí Balà Palasí

http://hdl.handle.net/10803/674105

DOCTORAL THESIS

Title	Development of a bioresorbable patch to treat aortic dissection
Presented by	Noemí Balà Palasí
Centre	IQS School of Engineering
Department	Chemical Engineering and Material Sciences
Directed by	Dr. Jordi Martorell López Dr. Salvador Borrós Gómez

A la meva família,
i tots els que m'han recolzat en aquest llarg camí

Acknowledgements

En primer lloc, m'agradaria agrair-li a la meva família el suport que m'han estat donant durant tots aquests anys, en especial als meus pares. Sou dues persones increïbles que sempre em feu costat i m'heu proporcionat les eines per arribar fins on soc ara. Gràcies per tot el que feu per mi, i per a tota la família. Espero poder tornar-vos tot allò que heu fet per mi durant tants anys.

El projecte d'aquesta tesi realment comença un any abans, el 2016, amb el meu projecte de màster. Allà comença la relació que realment ha marcat la meva vida durant els últims anys, la meva relació amb tu, Jordi. Ha estat un camí intens, amb entrebancs, amb alguna discussió però sobretot amb reptes, il·lusió, riures, amistat. Gràcies. Gràcies per confiar en mi sempre. Crec que hem format un bon equip i desitjo de tot cor continuar endavant, amb Aortyx i amb els reptes que se'ns posin per davant. Aprofito també per donar-li les gràcies a la Xuxi, ella que et fa costat, també m'ha ajudat en part en aquest llarg camí. Espero que la vida només us porti coses bones, com el Fugu o el mini-Martu.

A tu Salvador, que tot i que no estàs present en el dia a dia més immediat, sempre has estat allà donant-me els millors consells de ciència i també de vida. Gràcies per dedicar-me el teu temps i compartir amb mi, i amb nosaltres, tantes i tantes històries. He de dir que no enyoraré les esperes al banc de fora del teu despatx, però sí les reunions a la terrassa i les teves bromes, gràcies per tot.

També m'agradaria parlar del Vicenç. Gràcies per la teva amabilitat i la teva disponibilitat sempre. Per totes les hores que sempre em dediques, tots els consells i l'ajuda que em i ens dones sempre. Espero que el nostre projecte arribi ben lluny.

A tota la gent d'Aortyx. Per començar, a l'Àlex. Ha estat un any dur, però en el qual no has perdut mai el somriure, t'admiro moltíssim, des de sempre. Ets la persona que no pot faltar mai en un equip, per descomptat, no pots faltar al nostre, i t'has convertit en un gran amic en tots aquests anys. A la Carlota i al Paquito, m'heu robat el cor en poc temps i vull continuar compartint moments junts, per molts anys (i per molts més vins). Al Pau, Carlos, Germán, Inés, Juan, Laura, Sandra, Ivet i Anna. Són molts els moments que compartim, així que gràcies a tots per escoltar-me en algun moment de cansament, pels cafès compartits i les xerrades de la vida. Sou un pilar molt important a la meva vida.

Abans d'Aortyx també són molts els moments que hem compartit al laboratori de Supra. A l'Albeeeert(o). Soc feliç que formis part de la meva vida (i del vainilla), gràcies per tots els moments compartits i tots els que queden per arribar. Per les rises que ens hem fet amb l'Andrea, ets única i especial, i t'estimo més del que penses. A tu Oriol, m'encanta que t'hagis traslladat al CTPTi amb nosaltres. Aportes pau i picardia a parts iguals. I a la resta de l'altre lab, van ser temps molt divertits amb el porquet i les paraules prohibides, les xerrades amb el David, i tantes i tantes històries. Gràcies a tots, en especial al Gabi i Iris, i a tots els TFGs i TFMs amb els que hem compartit espai. Sobretot a la Blanca, que la vida ha fet que formis part de nosaltres i sincerament me n'alegro moltíssim.

M'agradaria també donar les gràcies a tots els meus amics fora d'IQS. Heu hagut d'aguantar molt i heu contribuït a fer-me aquest camí molt més planer. Els amics són la família que s'escull i jo he escollit als millors. Als de Vilassar: Marta, Sara, Carla, Ari, Ysa, Alba, Carlos, Moxi, Mortes, Aurora, Sergi, Joel i Raquel. A les meves amigues del cole: Ona, Marta, Anna, Helena i Núria. A les meves amigues de la UB que són sempre una alegria (i una birra darrera l'altra): Mar, Eva i Vinyi (i mini-Mar per descomptat). Volia agrair també a la Mercè i al Sergi per les hores que m'han hagut d'aguantar entre birres i vins.

A la Bermu, la Gemma i l'Oscar per la part que els hi toca. I segur que em deixo a moltes altres persones, gràcies a tothom que ha format part del camí.

I ara sí que vaig acabant. M'agradaria mencionar per últim (que no menys destacat) a tu, Edu. Sense cap dubte, ets el pilar més important de la meva vida i tot això que estic aconseguint és també gràcies a tu. Em fa extremadament feliç poder compartir amb tu els meus neguits personals i laborals. No és fàcil trobar una persona que t'entengui i et faci costat, amb qui discutir de la vida i de ciència, i jo tinc la sort d'haver-ho trobat. Gràcies per escoltar-me i donar-me sempre els millors consells. M'aportes la tranquil·litat i el seny que em falta i ho remates aportant-me una alegria i felicitat immenses. Per les nostres *tonteries*, el nostre gatet i tots els nostres projectes (d'emprenedoria) i de vida. T'estimo moltíssim.

0.1   Index

0.2   List of abbreviations

AD   Aortic Dissection

AAD   Acute Aortic Dissection

AAS   Acute Aortic Syndrome

CD   Corona Discharge

CFD   Controlled Force Deployer

CPB   Cardiopulmonary Bypass

CT   Computed Tomography

DMSO   Dimethyl sulfoxide

E   Young's Modulus

EC   Endothelial Cells

ECM   Extracellular Matrix

EGM-2   Endothelial Growth Medium-2

Echo   Echography

FBS   Fetal Bovine Serum

FL   False Lumen

Fn   Fibronectin

HAoEC   Human Aortic Endothelial Cells

HAoSMC   Human Aortic Smooth Muscle Cells

HE&S   Hematoxylin-Eosin & Saffron

IMMR   Institute Mutualiste Montsouris Recherche

IRAD   International Registry of Acute Aortic Dissection

MRI	Magnetic resonance imaging
N/A	Not applicable
NBF	Neutral Buffered Formalin NBF
PCL	Poly (ε-caprolactone)
PBS	Phosphate buffer saline
RGD	Arginine-Glycine-Aspartic acid peptide
SD	Standard deviation
SIAL	Serveis Integrats d'Animals de Laboratori
SMC	Smooth Muscle Cells
Sq	Squalene
STS	Society of Thoracic Surgeons
SVS	Society for Vascular Surgery
TE	Tissue Engineering
TEE	Transesophageal echography
TOE	Transesophageal echocardiography
YIGSR	Tyrosine-isoleucine-glycine-serine-arginine peptide
VGVAPG	Valine-glycine-valine-alanine-proline-glycine peptide
E	Young's Modulus

0.3 Abstract

Aortic dissection (AD) is one of the most catastrophic events that can occur in the aorta. In AD, the inner layer of the aorta tears, causing blood to flow through it. The dissection is often fatal if the blood-filled channel ruptures through the outer aortic wall. Aortic rupture may also happen but is up to 3 less common than AD. The estimated worldwide incidence is between 3 to 12 cases per 100,000 patient per year, with a global mortality of up to 50%, depending on the dissection type and patient conditions. Despite its relatively high incidence, AD has historically received less attention by medical device companies than other cardiovascular diseases. Since current solutions have not been specifically developed for AD but for aortic aneurysm, current treatments present very high mortality, morbidity, and reintervention rates.

In this thesis, we hypothesize that a treatment completely focused on AD would improve the outcomes of the surgery, in terms of survival, lifespan, and freedom from secondary effects. Instead of covering a substantial length of the aorta with a stented graft that is biomechanically very different than the aortic tissue, we propose using a small scaffold, with biomechanical properties very similar to the aorta's, to cover only the entry tear. To do so, we have designed a scaffold in the shape of a patch, made of polycaprolactone, a bioresorbable polymer, manufactured using electrospinning. This technique has allowed to create the patch with two different layers aiming to achieve different migration environments for the two types of cells present in the aortic wall: endothelial and smooth muscle cells. Moreover, the patch has been designed to have very similar mechanical properties to those found in healthy and dissected arteries.

Then, an *in vitro* study using different proteins and peptides and two types of surface treatments have been used to evaluate the endothelial cell response. The morphology helps guiding endothelial cells towards the aligned fibers. Moreover, even though the use of some proteins and peptides resulted in

enhancing the migration and proliferation of endothelial cells through the patch, the patch itself was enough to lead this process. Therefore, it was decided to avoid the use of additives for *in vivo* testing.

Finally, the patch was tested in an *in vivo* environment, demonstrating that it causes very low inflammatory response and that it adapts to the aorta in every heartbeat cycle. Moreover, cells have been able to colonize the patches, with reendothelialization and arterial remodeling in all the chronic tests performed.

0.4 Resum

La dissecció aòrtica (AD) és un dels esdeveniments més catastròfics que pot ocórrer a l'aorta. Quan es produeix una dissecció, apareix un forat a la paret de l'artèria que fa que la sang entri a través de la paret, separant-ne les capes. La dissecció és, amb freqüència, fatal si el nou canal es trenca per la part externa. Tot i que amb menys probabilitat és possible que la paret es trenqui per la part interna, causant danys menys dràstics. La incidència mundial d'aquesta malaltia s'estima entre 3 i 12 casos per cada 100,000 habitants a l'any, amb una mortalitat de fins al 50% depenent del tipus de dissecció i la condició del pacient. Tot i la relativament alta incidència d'aquesta malaltia, les companyies de dispositius mèdics hi han dedicat menys atenció que a d'altres malalties cardiovasculars. És per això que les solucions actuals no han estat dissenyades per tractar la dissecció sinó per a tractar els aneurismes de l'aorta. A més, els tractaments actuals segueixen tenint una taxa de mortalitat i morbiditat altes, i molts pacients necessiten ser re-intervinguts amb el temps.

En aquesta tesi es planteja la hipòtesi que un tractament dissenyat específicament per tractar la AD milloraria els resultats dels tractaments actuals en quant a supervivència, qualitat de vida del pacient i reduiria els efectes secundaris d'aquestes operacions. Enlloc d'utilitzar un llarg empelt fet d'un material que és mecànicament molt diferent de l'aorta, es planteja utilitzar un dispositiu petit, amb propietats mecàniques molt similars a les de l'artèria i que només tapi el forat. Per aconseguir-ho, s'ha dissenyat un dispositiu, un pegat, fet d'un polímer bioabsorbible, la policaprolactona, i utilitzant la tècnica d'electrospinning. Aquesta tècnica ha permès crear un pegat amb dues capes per buscar una diferent interacció amb els dos tipus de cèl·lules presents a l'artèria: les cèl·lules endotelials i les musculars. A més, s'ha aconseguit que el pegat tingui les mateixes propietats mecàniques de artèries sanes i dissecades.

A continuació, s'ha realitzat un estudi *in vitro* utilitzant diferents proteïnes i pèptids, i dos tipus de tractaments superficials per avaluar la resposta de les cèl·lules endotelials. La morfologia del pegat ajuda a guiar les cèl·lules cap a les fibres alineades. A més, tot i que l'ús d'algunes proteïnes o pèptids hagi resultat en una millora de la migració i proliferació cel·lular, el pegat per sé ha estat suficient per aconseguir assolir aquest procés. Així doncs, es va decidir procedir amb els experiments *in vivo* sense l'ús d'additius a la superfície del pegat.

Per últim, el pegat va ser testat *in vivo* demostrant que causa molt poca reacció inflamatòria i que s'adapta perfectament a l'artèria en cada batec. A més, les cèl·lules han estat capaces de colonitzar els pegats, aconseguint re-endotelització i remodelació arterial en tots els assajos prolongats.

0.5 Resumen

La disección aórtica (AD) es uno de los acontecimientos más catastróficos que puede ocurrir en la aorta. Cuando se produce una disección, aparece un agujero a la pared de la arteria que hace que la sangre entre a través de la pared, separando las capas. La disección es, con frecuencia, fatal si el nuevo canal se rompe por la parte externa. Aunque con menos probabilidad también es posible que la pared se rompa por la parte interna, causando daños menos drásticos. Su incidencia mundial se estima entre 3 y 12 casos por cada 100,000 habitantes al año, con una mortalidad de hasta el 50% dependiendo del tipo de disección y la condición del paciente. Todo y la relativamente alta incidencia de esta enfermedad, las compañías de dispositivos médicos han dedicado menos atención que a otras enfermedades cardiovasculares. Es por eso por lo que las soluciones actuales no han sido diseñadas para tratar la disección sino para tratar los aneurismas de la aorta. Además, los tratamientos actuales siguen teniendo una tasa de mortalidad y morbilidad altas, y muchos pacientes necesitan ser re-intervenidos con el tiempo.

En esta tesis se plantea la hipótesis que un tratamiento diseñado específicamente para tratar la AD mejoraría los resultados de los tratamientos actuales en cuanto a supervivencia y calidad de vida del paciente y reduciría los efectos secundarios de estas operaciones. En lugar de utilizar un largo injerto hecho de un material que es mecánicamente muy diferente de la aorta, se plantea utilizar un dispositivo pequeño, con propiedades mecánicas muy similares a las de la arteria y que solo tape el agujero. Para conseguirlo, se ha diseñado un dispositivo, un parche, hecho de un polímero bioreabsorbible, la policaprolactona, y a través de la técnica de electrospinning. Esta técnica ha permitido crear un parche con dos capas que busca una diferente interacción con los dos tipos de células presentes a la arteria: las células endoteliales y las musculares. Además, se ha conseguido que el parche tenga las mismas propiedades mecánicas tanto de arterias sanas como disecadas.

A continuación, se ha realizado un estudio in vitro utilizando diferentes proteínas y péptidos, y dos tipos de tratamientos superficiales para evaluar la respuesta de las células endoteliales. La morfología del parche ayuda a guiar las células hacia las fibras alineadas. Además, a pesar de que el uso de algunas proteínas o péptidos haya resultado en una mejora de la migración y proliferación celular, el parche per se es suficiente para lograr este proceso. Así pues, se decidió proceder con los experimentos *in vivo* sin el uso de aditivos a la superficie del parche.

Por último, el parche fue testado *in vivo* demostrando que causa muy poca reacción inflamatoria y que se adapta perfectamente a la arteria en cada latido. Además, las células han estado capaces de colonizar los parches, consiguiendo reendotelitzación y remodelación arterial en todos los ensayos prolongados.

1 INTRODUCTION

1.1 Anatomy of the Aorta

The aorta is the largest artery in the body. It measures more than one meter in length and up to three centimeters in diameter in a healthy adult[1]. The aorta is one of the principal organs of the cardiovascular system, constituted also by the heart, blood and other vessels. Heart pumps fresh blood to the aorta through the aortic valve and this distributes oxygen and nutrient-rich blood through all tissues in the body[2]. Besides its conduit function, the aorta plays a major role in controlling the systemic vascular resistance and heart rate[3]. Through its elasticity, the aorta acts as a "second pump" during diastole, feeding the coronary arteries that provide blood to the heart.
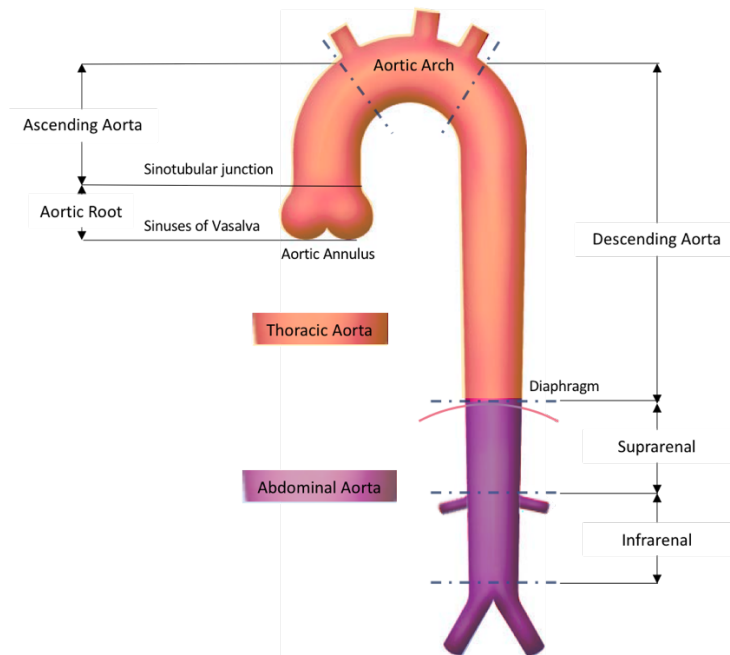
Figure 1. Anatomical parts of the aorta[2].

The aorta is divided into two regions located above and below the diaphragm, the thoracic and the abdominal aorta[2,3]. Each region is divided into different components (Figure 1). The thoracic aorta arises from the heart at the aortic root and continues through the ascending aorta, a 2.6 ± 0.3 cm in diameter segment that is the one of the most prone to being diseased due to being the

first receiver of the pulse wave originated at systole. The aorta then curves at the aortic arch, where three branches arise: the right brachiocephalic artery, the left carotid artery, and the left subclavian artery. They are responsible for supplying blood to both arms and the head. The descending aorta starts right after the arch, and it is the last part of the thoracic aorta, carrying blood downwards through the chest[1]. The abdominal aorta is formed by the suprarenal and infrarenal segments. The diseases involving the abdominal aorta normally include atherosclerosis and aneurysms. In fact, the abdominal aorta is the most frequently aneurismal site of the aorta.

1.1.1 Aortic wall composition

Blood vessels are formed by two parts: the lumen, which consists in the corridor through which blood flows, and the wall, which holds the artery's structure and resists the heart pressure. Arterial lumen is smaller than venous to help maintaining blood pressure throughout the system. Walls of larger blood vessels, such as the aorta, are thicker than veins since they receive blood surging directly from the heart and, consequently, greater pressure[4].

The vessel wall contains three distinct layers or *tunicae* with different composition and function (Figure 2)[5]. The three layers, starting with the outermost, are:

1. *Tunica adventitia*. It is the outer layer, and it is separated from the tunica media by an external elastic lamina. It is usually half the width of the tunica media, and it is mainly constituted by collagenous tissue which supports fibroblasts and nerves. The adventitia also contains the *vasa vasorum*, a network of small blood vessels that penetrates the outer portion of the tunica media and supply the vascular wall with oxygen and nutrients.

2. *Tunica media*. It is a thick middle layer which contains smooth muscle cells (SMC) embedded in an extracellular matrix (ECM). The media of

elastic arteries, such as the aorta, consists of 40 to 70 layers of elastic sheets alternating with thin layers of SMC, circularly arranged; collagen and elastic fibers. These cells are organized and supported by a framework of elastic fibers. This layer strengthens the vessel and prevents blood pressure from rupturing it.

3. *Tunica intima*. It is the *tunica* exposed to blood. The layer consists of a monolayer of endothelial cells (EC) called endothelium, supported by connective tissue[6]. These cells secrete vasoactive substances and serve as a barrier, playing a crucial role in controlling vascular permeability, vasoconstriction, angiogenesis, and regulation of homeostasis. Its thickness is less than 0.2 μm and can reach up to 1 kg in total in an adult. Underneath this layer, a variable number of elastic fibers in the internal elastic lamina separates the intima and the media. This layer is particularly important in atherosclerosis formation despite its minor contribution to the mechanical properties of the aorta[7]. It is interesting that, although the amounts of connective tissue and smooth muscle cells in the vessel wall vary according to vessel's diameter and function, the endothelial lining is always present[8].
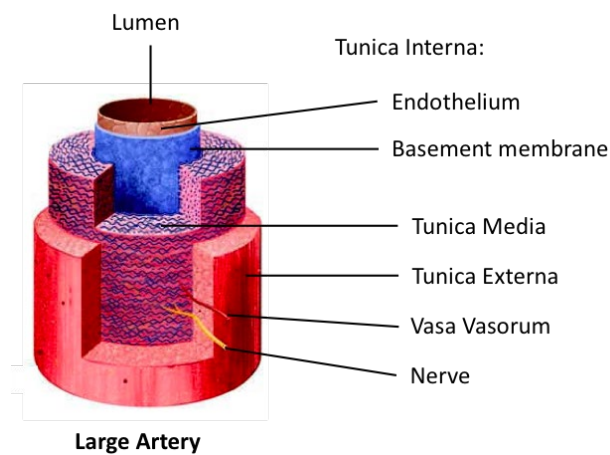
Figure 2. Arterial vessel wall[9]

Among the three layers, the *tunica intima i*s the most interesting for this thesis due to the importance, because the endothelium lines the entire vascular system and virtually controls every cardiovascular function. The endothelium is usually described as a dynamic organ that regulates its environment and responds to external stresses[10]. This dynamism is given by the EC that adapt their phenotype to the tissue needs and local environment[11]. EC can detect several types of input and can generate several types of output; while most sensory systems detect only one input and generate one output. Among the vascular EC functions, one can find the maintenance of blood fluidity, the regulation of blood flow, the control of vessel-wall permeability and quiesce leukocytes.

In the event of an acute inflammation (over a period of hours), ECs are "activated", resulting in a rapid recruitment of neutrophils. This activation may be divided into two different responses, stimulation and activation, depending on if there is new gene expression or not. Both types of activation response have four signs in common: an increase of local blood flow, a localized leakage of plasma-protein-rich fluid into the tissue, localized recruitment and activation of circulating leukocytes induced to enter the infected or damaged tissues, and pain, caused by mediators released by leukocytes.

If acute inflammatory reactions fail to eradicate the triggering stimulus, and especially if an adaptive immune response is activated by persistent stimulation, the inflammatory process evolves to a more chronic form, in which specialized effector cells are involved. EC might participate in this process by presenting antigens to circulating effectors.

In a non-inflamed aorta, the maintenance of blood fluidity is crucial to avoid clot formation, which may become fragmented, forming emboli. These emboli follow blood circulation and may cause damage if they obstruct other vessels, lead to infarcts or ictus in the worst-case scenario. Therefore, the inhibition of

the coagulation cascade is important, and EC are involved in several anti-coagulation mechanisms[12].

In addition to EC, the ECM, the non-cellular component that is also present in all tissues and organs is of utmost importance. It is an active and highly dynamic structure that serves as a supporting network for blood vessels[13] and their biological function such as cell adhesion, migration, proliferation, phenotype, and tissue architecture. Changes in the ECM structural components result in variations in their function and, therefore, may compromise the aortic wall function and structure[14].

The ECM constitutes more than half of the aorta's wall mass, being collagen and elastin the two major components. Other elements found in the ECM are fibronectin, microfibrils, abundant amorphous or soluble proteoglycans, and leucine-rich glycoproteins[14,15]. The protein distribution is not linear among all the walls; some components are secreted and modulated by EC, some by SMC and others by fibroblasts and their abundance is driven by the presence of these cells in each tunica.

As said before, damage in the aortic wall, including ECM components, compromises the aortic integrity, triggering the development of several vascular diseases like aortic dissection. The ECM state hence plays a fundamental role in disease progression.

1.2   Aorta's mechanical properties

The aorta, unlike other blood vessels, cannot be considered only a passive conduit for the bloodstream[16,17], but also as an elastic reservoir, enabling the arterial tree to undergo large volume changes with little pressure changes[7]. Without elastic vessels, the tremendous pressure created as blood is ejected from the heart would prevent the heart from emptying, and the pressure in the vessels would fall so rapidly that the heart would not be able to refill. The aorta stores a portion of the stroke volume of each systole and discharges it during diastole. This phenomenon is known as the Windkessel effect[18]. This is possible thanks to specialized ECM molecules uniquely designed to provide elastic recoil in the vessel wall[19].

Elasticity is hence one of the most important physical properties of the aorta. It is defined as the material property that resists permanent deformation under tension. Elasticity coefficients are defined as the ratio between this resisting force and the deformation produced[20]. Young's modulus, represented by E, is a classic representation of the elastic modulus of a material, and is extracted from the stress-strain curve[19]. The stress is the force applied to a material or tissue per unit of its cross-sectional area; the strain is the deformation of the material.

In the aorta, elastic resistance, also named stiffness, describes the resistance set by the aorta against its distention when an additional volume is injected, and the intraluminal pressure increases. The inverse of stiffness is compliance, which describes the ease with which the aorta expands during systole[21]. The mechanical properties of a vessel depend strongly on the anatomy they rely on, because they are dependent on the magnitude and types of stress that the wall is subjected to[17,22]. Even in the same segment, properties vary along the circumferential and longitudinal direction. For example, *in vivo* longitudinal

strain varies from 10 to 70% depending on location in the arterial tree, with distal vessels generally being more stretched than proximal vessels[23]. More precisely, the proximal ascending aorta has an *in vivo* strain starting at ~10%, but this increases to 15-20% at points in the cardiac cycle due to motion of the heart. That is because of the nonlinearity in blood vessel elasticity and the mechanical anisotropy of the aorta[24]. This can be observed in experimental stress-strain curves (for example in Figure 3); where the nonlinear elastic behavior is represented by increase in artery stiffness with increasing strain[25].
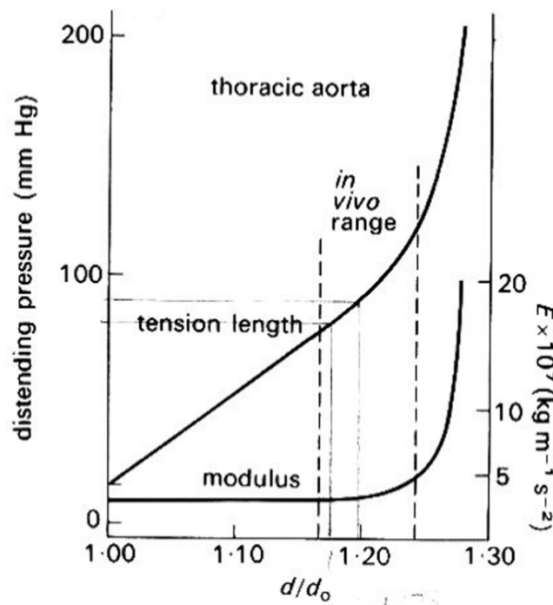
Figure 3. Graph of distending pressure in relation to diameter for a piece of artery of fixed length. The effective (incremental) Young's Modulus is also plotted and relates the circumferential stress to circumferential strain. This increases dramatically for distending pressures greater than normal[26].

There are different methods to test the mechanical anisotropy of the aorta, such as the uniaxial and biaxial tensile tests, physiologically simulated test and digital image correlation (DIC) technology[27]. Wide attention on the first method is made in the following chapters of the thesis for its simplicity, because it is widely used to test biological tissues and it gives precise information when searching for local properties of soft tissues[17].

1.2.1 Viscoelasticity of the aorta

The aorta is not a purely elastic material. It is not only able to dilate under pressure, but its fibers realign to slowly recoil to its initial shape when blood pressure falls[18]. Since there is a hysteresis in the pressure-volume curve, the aorta is not purely elastic but viscoelastic.

Defining the viscoelastic behavior of the aorta starts by identifying the viscoelastic features, which are creep, relaxation, and hysteresis. Creep happens when a body is suddenly stressed in the elastic range for a long period of time and the strain increases very gradually. This implies that a very slow flow is taking place. If the stress is withdrawn, the strain does not reduce exactly to zero. Instead, a small value remains because the body continues to deform. It differs from plastic flow in that it is reversible: if a compressive stress was then applied for a long time, a reverse slow flow would be observed, and eventually the strain measured when no stress is applied could be reduced to zero. Creep does not irreversibly destroy the molecular structure of a material in the way that plastic flow does. An associated phenomenon occurs when constant displacement is maintained for a long time[26]. Stress relaxation, or relaxation for short, happens when a body is suddenly strained, the strain is maintained constant afterwards and the corresponding stresses induced in the body decrease over time (Figure 4).
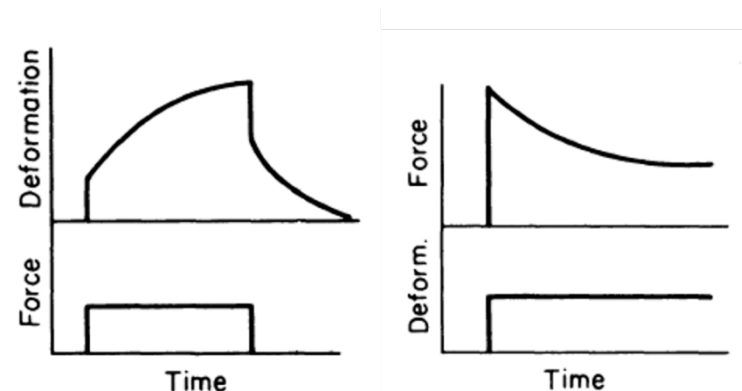
Figure 4. Creep and relaxation functions of standard linear solid[19].

Finally, when the body is subjected to cyclic loading, the stress-strain relationship in the loading process is usually somewhat different from that in the unloading process, and the phenomenon is called hysteresis[19]. Different mechanical models are used to characterize the viscoelastic behavior of materials, including Maxwell, Voigt and Kelvin models. The Kelvin model (or standard linear model) is the most general relationship that includes load, deflection, and their first derivatives.

1.2.2 The role of ECM molecules in the aorta's mechanical properties

The variation of arterial elasticity and viscoelasticity along the arterial tree can be explained qualitatively by the composition and structure of the arterial wall[19]. About 70% of the arterial wall weight consists of water, which is not elastic. However, the rest of the weight contains a wide variety of elements, among which a mesh of fibers with elastic properties[20]. This fiber mesh is primary composed by elastin and collagen, and, in a lesser amount, of SMC. These components are very different; elastin provides reversible elasticity to the aorta while, in contrast, collagen provides strength and limits distention at high pressures[28]. Elastin is a rubber-like substance, with a Young's Modulus of approximately 0.3 MPa and collagen is much stiffer than elastin (E≈100 MPa). Although elastin is so compliant that it can be stretched to twice its unstretched length, the stress at which it eventually breaks (its tensile strength) is less than 5% of that of collagen. Smooth muscle cells have an elastic modulus like that of elastin; however, the exact value measured in an experiment depends on the level of physiological activity. It varies *in vivo* from 0.1 MPa when the muscle is completely relaxed to 2 MPa when active[26].

Aortic walls lose elasticity over time and this process results in increased arterial stiffness. This process is characterized by an alteration in the ECM composition, in particular, of both elastin and collagen fibers[29]. Arterial stiffening, at least in part, reflects gradual fragmentation and loss of elastin fibers due to ages of fatigue and accumulation and deposition of stiffer collagen fibers in the arterial wall[30]. This results in the alteration of both the mechanical properties of the vascular wall and of the intraluminal blood pressure, and thus also the mechanical forces to which EC and SMC are exposed. Damage in the aortic wall, and that includes ECM components, compromises the aortic integrity, triggering the development of several vascular diseases like aortic dissection.

1.3   Aortic dissection

An aortic dissection (AD) is the most frequent and catastrophic manifestation of the so-called acute aortic syndrome (AAS) which also includes intramural hematoma, penetrating aortic ulcer, and ruptured thoracic aortic aneurysm[3]. . In the case of AD, its incidence is estimated between 2 to 12 out of 100.000 patients per year, with a 66.9% male preponderance[31]. The most frequent risk factors to develop aortic dissection are age (the mean age is 63), hypertension (76.6% of the patients), atherosclerosis (26.5% of the patients), previous cardiac surgery (16.1% of the patients), and iatrogenic cause due to previous catheter-based procedures (2.8% of the patients)[32]. Ever-smokers have a relative risk of 3.28 times higher than never smokers[33]. Some genetic diseases like Marfan syndrome[34], Loeys-Dietz syndrome[35], Ehler-Danlos syndrome and Turner syndrome[36] have a high frequency of AD. Despite advances in imaging techniques, diagnosis is still often delayed[37]. Therefore, AD is a life-threatening condition that remains a challenge to diagnose and to treat[32].
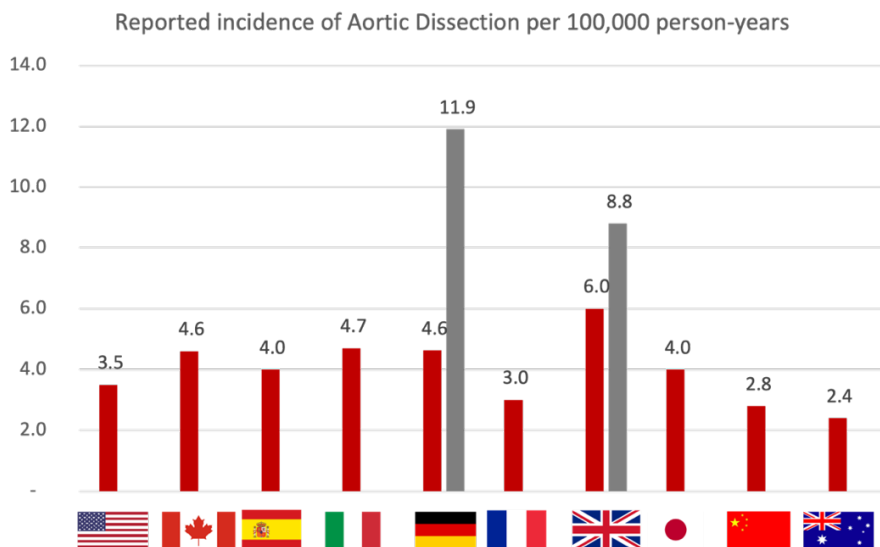
Figure 5. Reported AD worldwide incidence[38,39,40,41,42]

Mainly two events can origin AD. The first and most common is the formation of an intimal tear which allows blood flow through the arterial wall and forces the separation of the layers of the aorta forming an intimal flap. The second event is the rupture of the vasa vasorum, which also causes bleeding and may end up with the formation of an aortic dissection. Both conditions can coexist (Figure 6), resulting in the formation of a secondary channel, namely the false lumen (FL), in which blood flows. The FL can propagate distally in a spiraled manner, which is the most often manifestation, or straight manner. The FL can also propagate proximally all the way to the aortic valve. A frequent complication is the compression of the true lumen (TL) by the pressurized FL, which often collapses and leads to ischemic complications downstream[5, 43].
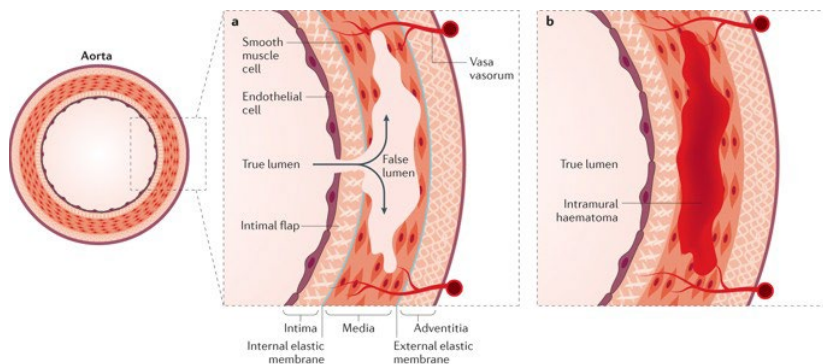
Figure 6. Aortic dissection causes[40]

Anatomically, AD can be classified following two different systems based on the location of the intimal flap. The first classification system, the DeBakey classification, was published back in 1965 and describes AD according to anatomic features. Years later, the Stanford classification was published. It is a system based on whether the ascending aorta is affected or not, and is more widely used nowadays[44]. According to the Stanford classification there are two anatomical types of AD: type A, a dissection in the ascending aorta in spite of the entry site location, and type B, a dissection in the distal aorta to the origin of the left subclavian artery (Figure 7). Approximately two thirds of cases of acute AD are type A, and the rest are type B[45].

Stanford Classification

Type A   Type B
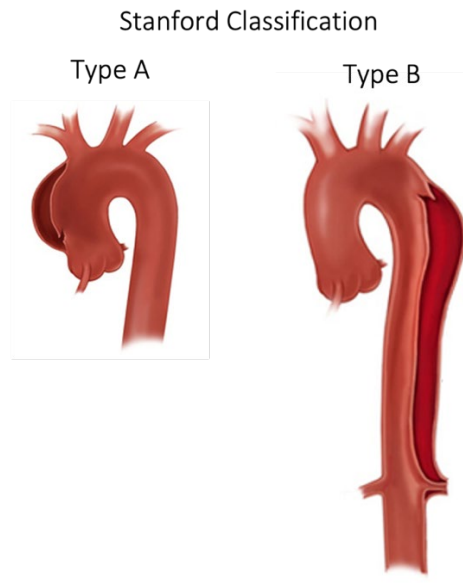
Figure 7. AD Stanford classification[46,47]

Recently, the Society for Vascular Surgery (SVS) and the Society of Thoracic Surgeons (STS) came up together with a new classification for type B AD[44] because, neither classification scheme addresses AD that originate in the arch. Within the new SVS/STS classification, the distinction between type A and type B is predicated on the entry tear location alone. Type B dissections are further characterized by two subscripts ($B_{P,D}$). Subscript P describes the proximal zone of involved aorta, and subscript D describes the distal zone of involved aorta. This new classification standard represents a more practical manner of differentiating AD and their consequent treatment.

In the clinical classification, overall AD is divided into acute and chronic types, depending on the duration of symptoms. Acute aortic dissection (AAD) is diagnosed when the clinical symptoms have lasted 14 days or less, and treatment within this period is regarded as acute. Beyond the second week, the dissection is classified as chronic[48]. More recently, in 2013, a group of vascular and cardiovascular surgeons reinterpreted the timeline

classification[49] after analyzing the data provided by The International Registry of Aortic Dissection (IRAD). The IRAD was established in 1996 with the purpose of recording AD cases around the world. Since the first publication in 2000, 51 referral centers in 12 countries in North America, Europe, Asia, and Australia have contributed to create this database[32]. In this sense, thanks to IRAD's data, they were able to distinguish four different time periods: hyperacute (0-24 hours), acute (2-7 days), subacute (8-30 days), and chronic (>30 days).

1.3.1 Current treatments

In the past, surgical replacement of the dissected section was the only effective treatment, carrying however high risks of mortality and morbidity[50,51]. Numerous studies have reported the safety and efficacy of thoracic endovascular aortic repair (TEVAR), especially for type B aortic dissection[52]. Endovascular interventions using stented grafts reduce mortality and length of hospitalization but not all patients are eligible for surgery. Whether or not a patient from suffering AD undergoes any intervention, medical therapy to control pain and hemodynamic state is essential[2]. Beta blockers have the desired effect of reducing blood pressure and heart rate to the normal range. These medications also protect the myocardium against ischemia[53]. In the least severe cases, this therapy delays intervention, sometimes for years.

AD is treated differently depending on the location of the tear and on the associated complications. Relevant anatomical features, such as the higher elasticity of the ascending aorta compared to the descending aorta, justify the different approaches. The overall mortally after effective treatment in both AD types is represented in Figure 8[49].
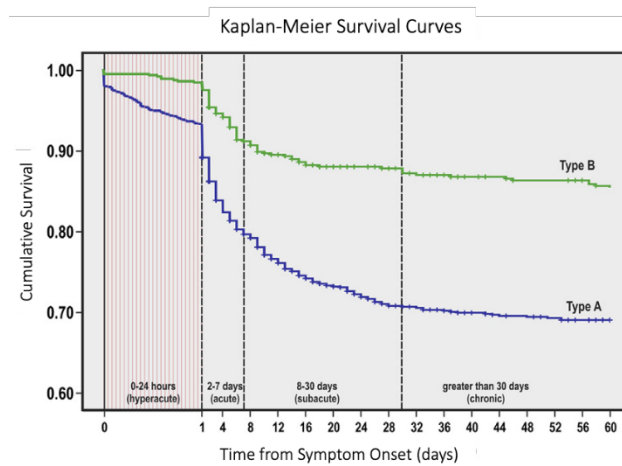
Figure 8. Kaplan-Meier Survival Curves for type A and B AD[49]

AD occurring in the ascending aorta is a catastrophic event which requires immediate surgical intervention. Acute type A AD has a mortality of 57% within the first 48 hours if not operated[2,32]. Despite the improvements on the surgical and anesthetic techniques, both perioperative mortality (25%) and neurological complications (18%) remain high[54]. However, surgery reduces the first month mortality from 90% to 30%.

The surgical intervention involves the resection of the dissected part containing the tear (Figure 9). The damaged segment is then replaced by a synthetic (Dacron) vascular prosthesis. Valve replacement is also needed in most severe cases[31]. This kind of surgery requires cardiopulmonary bypass in hypothermia, keeping the patient between 24 and 30ºC to protect the brain[55]. Thus, the surgical procedure itself compromises survival chance significantly.
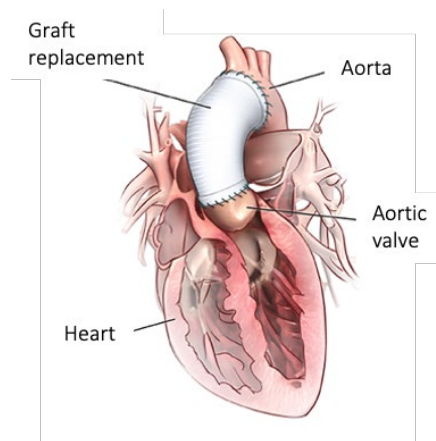
Figure 9. Open repair surgery[56]

In-hospital and early mortality associated with Type A AD range from 15%-32% in surgically treated patients, while those treated medically have an overall in-hospital mortality of 56%- 58% (Figure 10). Based on evidence, all type A AD should undergo surgery. Despite that, more than 15% of all patients can't undergo open repair[57], and are treated medically, but their projections are

significantly worse compared to the surgical replacement. Those managed medically have an in-hospital mortality rate of 60,2% versus 23,6% of those treated surgically (Figure 10[49]). Open surgery implies a high risk for the patient, not only during the intervention but also in the subsequent hospitalization days. Recent studies report a stroke incidence of 2–16% after operation[58]. Preoperative shock status is largely related to the incidence of postoperative stroke. Moreover, the material used for the graft is not optimal. Although the graft replaces the affected section, it does not replace the viscoelastic and damping properties of the original aorta. Despite patients may achieve full recovery, they still need hypotensive medication during their entire lifetime. Furthermore, descending aorta re-interventions are needed in approximately 30% of the cases, 5 to 10 years after successful operation. These reinterventions are caused by the differences in the mechanical properties of the graft compared to the aorta. Since the graft is not compliant with the artery, it does not properly absorb the pulsatile heartbeat, which results in the formation of new aneurysms downstream. Moreover, the open surgery carries high mortality and morbidity rates by the intervention itself which would be drastically reduced by introducing an endovascular treatment.
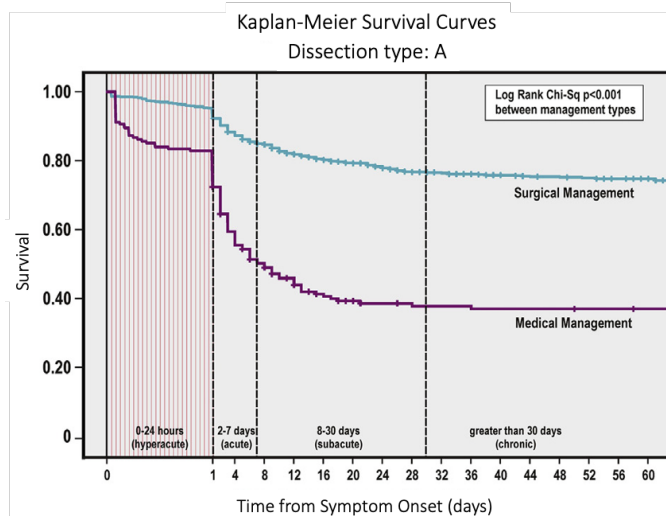
Figure 10. Kaplan-Meier Survival Curves for type A AD[49]

In the case of type B AD, different approaches are followed depending on the complication of the symptoms. Uncomplicated stable type B AD is tackled using a pharmacological approach: drug administration to control blood pressure. The goal of the so-called medical therapy is to avoid short term complications, control pain and heart rate[2]. However, patients receiving long-term pharmacological treatment only tend to suffer from aneurysmal expansion of the false lumen and late complications. Coherently, subsequent intervention is required in 25% to 30% of patients.

Complicated type B AD is usually treated with thoracic endovascular aortic repair (TEVAR). TEVAR was introduced back in 1999 as an alternative treatment for type B AD patients[59]. The method consists in placing a covered stent graft over the entry tear in the descending thoracic aorta (Figure 11). TEVAR is usually performed via femoral artery access. The true lumen is rapidly expanded whereas the false lumen collapses. Complete thrombosis of the false lumen has been associated with an improved outcome. In some cases, TEVAR is not effective as the first-line approach and open surgery replacement is then performed. In other complicated cases, a hybrid procedure is the best option to tackle the AD. Both endovascular and open repair surgery are combined with medical treatment.
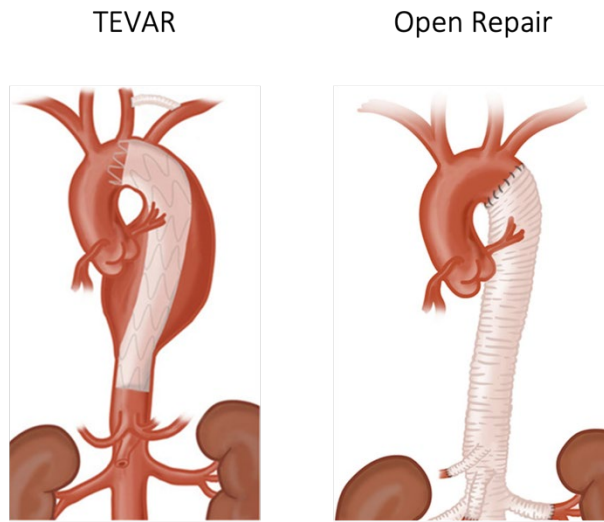
TEVAR   Open Repair

Figure 11. Thoracic Endovascular Aortic Repair (TEVAR) and open repair approach[60]

Conventional open surgery is currently reserved for chronic patients with anatomy unsuitable for endovascular treatment or patients with connective tissue diseases. Open repair is required in about 30% of patients with complicated chronic type B aortic dissection and is associated with higher procedural morbidity and mortality[61].

The course of Type B AD is often uncomplicated so the patient can be safely stabilized under medical therapy alone, to control pain and blood pressure. Mortality in the acute phase does not differ between patients treated medically or with TEVAR (Figure 12). As a result, the perception of TEVAR as a better alternative diminished. Conversely, TEVAR appear to be very appropriate in cases of emerging complications[62], and prove better than surgical and medical management 30 days after the onset of symptoms.
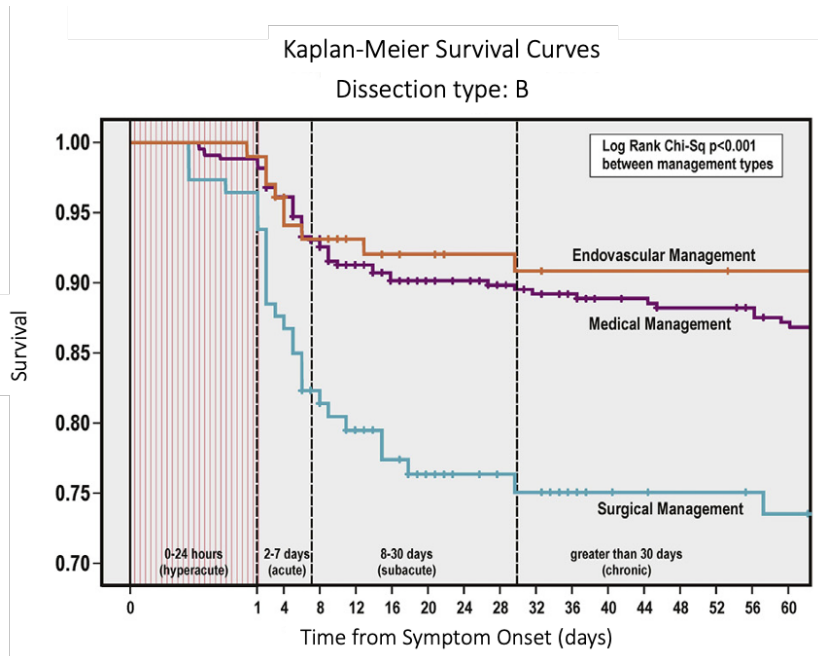
Figure 12. Kaplan-Meier Survival Curves for type B AD[49]

Overall, stents have reported good results but still present many limitations[63,64]. On the negative side, these grafts do not fully conform to the patient's aorta; their apposition is always complicated. If the stent is under expanded, thrombi can form and/or the graft may be displaced over time. If the stent is over expanded, it creates micro-injuries along the lumen that further damage the already jeopardized vessel. Re-intervention on the long-term is hard to avoid. Like with grafts used in open surgical repair, the material used for the graft is not optimal. While grafts fix the tear and stop internal bleeding, their material is inert, non-degradable and with mechanical properties very different to healthy arteries'. None of these grafts actively promotes false lumen clotting and resorption, nor vascular remodeling and regeneration, preventing the endothelium from recovering its complete function.

Therefore, there is a need for devices and methods for the treatment of aortic dissection which focus on regeneration of the damaged vascular tissue which focuses on restoring its original form and function. Ideally, such devices would be minimally invasive (i.e., suitable for endovascular deployment) and the devices would be able to cover a vascular defect to provide immediate structural repair and, after covering the defect, would promote healing, cellular regeneration, and complete vessel recovery. Further, this medical device should be resorbable following complete repair and restoration of vascular function. The cellular regeneration of the vessel would prevent or minimize any graft-related side effects, thereby diminishing re-intervention rates.

1.4 Hypothesis and objectives

Aortic dissection is a life-threatening condition with clear unmet medical needs. Despite the progress in surgical techniques, perioperative complications and mortality remain high. Open and endovascular repair have limitations and risks. The lack of treatments that consider the aorta's morphology and biology opens the opportunity to change the paradigm on how AD is treated.

This thesis hypothesizes that a new endovascular treatment based on a bioresorbable scaffold that mimics the mechanical properties of the aorta would improve current available treatments for AD. This thesis aims at understanding the techniques used to create scaffolds for biomedical applications and that fit the special requirements of an organ as complicated as the aorta. To verify these hypotheses, the objectives are:

1. To create a scaffold with a microstructure able to mimic the aorta's biomechanical environment.
2. To demonstrate, *in vitro,* that the scaffold developed provides a suitable milieu for cell migration and proliferation.
3. To demonstrate, *in vivo,* that the scaffold developed provides with the best environment to promote reendothelialization.

2 CREATING A SCAFFOLD WHICH MIMICS THE AORTA'S BIOMECHANICAL PROPERTIES

2.1 Introduction

The internal organization of the aortic wall allows cells to interact with each other and with the surrounding ECM. The main hypothesis of this thesis is that a scaffold able to partially recapitulate the physical, mechanical and biological properties of the aorta is crucial to induce a regeneration process[65]. Such scaffold should guide cells towards their phenotype and architecture to restore tissue function and induce the cells from the surrounding tissue to infiltrate implanted matrices. Regardless of the tissue type, there are some key considerations when designing or determining the suitability of this particular scaffold[66,67]:

1. Biocompatibility. Cells must adhere, function and migrate onto the surface and through the scaffold. The scaffold must produce negligible immune and thrombogenic reaction after implantation. This would prevent from causing an adverse response that would result in reduced healing and can cause body rejection and/or thrombosis.

2. Biodegradability. The new scaffold is not intended to be a permanent implant. The objective of the scaffold is to allow cells to colonize and eventually replace the implanted scaffold. In the end, cells must produce their own ECM and the resulting products of the scaffold degradation should be non-toxic. This is critical to overcome some drawbacks of current grafts.

3. Mechanical properties. The structure should mimic the mechanical properties of the anatomical site where it is implanted. After studying the complexity of the mechanical behavior of the aorta in previous sections, this is perhaps the most challenging aspect when designing the scaffold.

4. Scaffold architecture. A well-connected porosity network that allows cells to penetrate and grow onto the scaffold. Moreover, it must allow

an adequate diffusion of nutrients to cells within the construct and to the ECM matrix formed by these cells.

5. Manufacturing technology. Clinical and commercial viability as well as cost-effective manufacturing process, are critical for scaffold success. The development of scalable manufacturing processes to good manufacturing practice (GMP) standards must be considered to ensure the translation from benchtop to bedside.

As seen in previous sections, the aorta is a complex organ with highly specific mechanical and biological properties. The process of creating the scaffold implies choosing the right material, or combination of materials, that by using a specific technique allows reaching the aneled properties[68].

Biomaterials play a pivotal role in this process by serving as matrices for cellular ingrowth, proliferation, and new tissue formation in three dimensions[69]. Although there is a wide variety of biomaterials, we decided to choose polymeric materials to create our scaffold considering the nature of the aorta's tissue. Polymers have received increasing attention when creating biological scaffolds thanks to a relatively easy control over biodegradability and processability. Natural polymers facilitate cell attachment and differentiation, but synthetic polymers are more versatile since their physicochemical properties can be tailored during synthesis[70]. Durability is another key property. Current aortic grafts have a long life ahead when implanted, and this can be a problem, although it may sound counterintuitive. The aorta is a living organ that changes, moves and grows, and this dynamism is not matched by the graft. Most graft failures come from this mismatch, so they must be eventually replaced or removed. For this reason, the synthetic polymer matrix of choice must be bioresorbable. In this sense, one of the best options is polycaprolactone (PCL).

PCL is a synthetic polyester with great biocompatibility and processability[70], used in many CE-marked and FDA-approved for medical applications[71,72]. PCL possesses an excellent thermal stability and has a slow degradation rate, thus making it a good choice since the healing of the dissected tear would take longer than, for example, the healing of a wound[73]. The degradation rate of our scaffold should match the tissue regeneration rate[74], so PCL can be resorbed after the appropriate implantation time[75]. Finally, PCL releases nontoxic by-products upon hydrolytic degradation *in vivo*.

PCL properties can be tailored and are extremely dependent on the method of fabrication. One of the main concerns since the begging of this creation process was to design a scaffold porous enough for cells to grow and migrate towards the pores. The selection of the manufacturing method that provides sufficient architecture with balanced stiffness, cost- and time- effectiveness is of greater importance[76]. Several preparation methods are used to produce PCL-scaffolds, some of them were tried in previous projects[77,78]. In an aortic scaffold, the goal is to promote endothelial and smooth muscle cells colonization. EC are generally thin and elongated, 50-70 μm long, 10-30 μm wide; and 0.1-10 μm thick[79]. SMC are spindle-shaped, and their size is more variable from 30 to 200 μm[80]. Coherently, the internal structure should be in the range of micro to nano. Electrospinning is a manufacturing technique that allows the production of polymeric micro- and nanofibrous scaffolds from polymer solutions, blends or melts[81,82]. The fiber morphology and distribution can be tailored by adjusting the technique parameters or solution conditions. Overall, electrospinning is a controllable, simple, continuous, scalable and quite reproducible technique that matches the needs of this thesis.

2.1.1 Electrospinning

The history of electrospinning is dated back to 1934 when Formhals patented the electrospinning method, associated with the process and the apparatus for producing artificial filaments using electric charges[83]. But it is in the end of the twentieth century that the interest in this method has gained more attention.

The process starts by dissolving the polymer, synthetic or natural, in a highly volatile solvent. This solution is exposed to a high electric potential (10 – 30 kV) across a finite distance between a conductive needle and a grounded collector[84]. The electrically charged polymer solution forms a conical shape, called a Taylor cone, at the tip of the needle. When the electric charge at the needle tip overcomes the force due to surface tension and viscosity[85], a whipping polymer jet is ejected from the apex of the cone. The jet is directed towards the grounded collector, the solvent evaporates during the polymer flies from the needle tip to the collector and dry fibers deposit on the collector.

The collector is made of a conductive material which is grounded to create a potential difference with the spinning tip and draw the polymer solution from the spinning tip. The collector may have different configurations, such as a planar plate (producing a randomly oriented web of electrospun filaments) or a rotating drum (producing an aligned web of electrospun filaments, with the degree of alignment depending on the rotational speed of the drum) (Figure 13). The drum is connected to a power bank that enables it to rotate clockwise or counterclockwise between 200 rpm and 2000 rpm. Rotation can modify the fiber diameter and morphology and should allow to evolve from manufacturing random fibers to aligned[86].
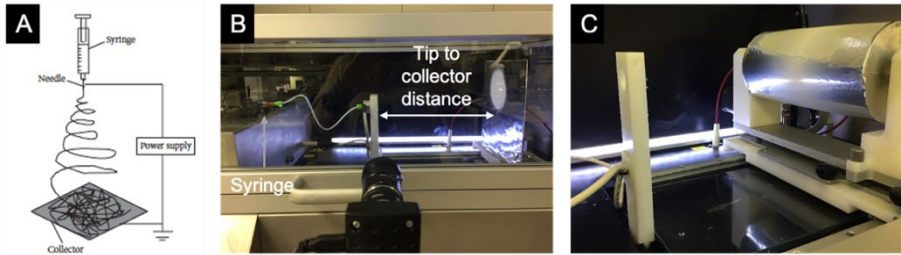
Figure 13. A) Schematic of a laboratory-scale vertical electrospinning setup[83] B) Fluidnatek LE-10 equipped with a flat collector. C) Drum collector.

Under favorable conditions, upon arrival at the collector, the fibers have reached diameters in the nanometer range and are collected as nonwoven fiber mats[87]. Advances in the electrospinning technique allow the production of more complex structures[82] and the electrospun fibers can be collected in various forms such as sheets or tubes for use in engineered skin grafts, blood vessels, heart valves, tendons and muscles, or as single fibers[88].

In general, electrospinning can generate fibers as thin as tens of nanometers in diameter by optimizing some conditions. These can be separated in three groups: ambient conditions, solution or material properties and operational parameters[83]. The ambient conditions are temperature and humidity of the chamber in which the process takes place. The intrinsic properties of the solution are, for example, the polarity and surface tension of the solvent, the molecular weight and conformation of the polymer, the polymer chain entanglement and intermolecular interactions, viscosity and elasticity, and electrical conductivity of the solution.

And, finally, operational parameters include the strength of the electric field (the voltage), the distance between the spinneret and the collector, and the feeding rate for the solution[81,89,84]. Flow rate is considered one of the key parameters when controlling fiber diameter and its distribution, initiating droplet shape, the trajectory of jet, maintenance of Taylor cone and deposition area. At high flow rates, larger droplets are formed, which increase the average fiber diameters and bead[90] size. But the structure of the electrospun fibers is under the influence of a large number of interrelated variables, like the operational parameters or the size of the nozzle orifice, but also like the polymer molecular chain length or the solvents used and the solution properties[84]. Several papers report the effect of the solvent on the fiber morphology[84,91,92].

2.1.2 Electrospinning to create the scaffold with the end-user requirements

The electrospinning process starts by dissolving the PCL into a solvent to generate an electrospinnable solution. The solvents used in an electrospinning process should have low boiling points, to evaporate on the way to the electrospinning collector, and a high dielectric constant to promote fiber stretching[93]. In this sense, the interactions between polymer and solvent critically influence diameter, crystallinity, tensile strength, aspect ratio, and morphology of the electrospun fibers[94]. Chloroform was the solvent chosen based on the spinnability-solubility map for PCL, together with the wide experience on polymers of the research group. Chloroform has a low boiling point of 61.1 ºC and a dielectric constant of 4.81 at 20 ºC[95] (Figure 14).
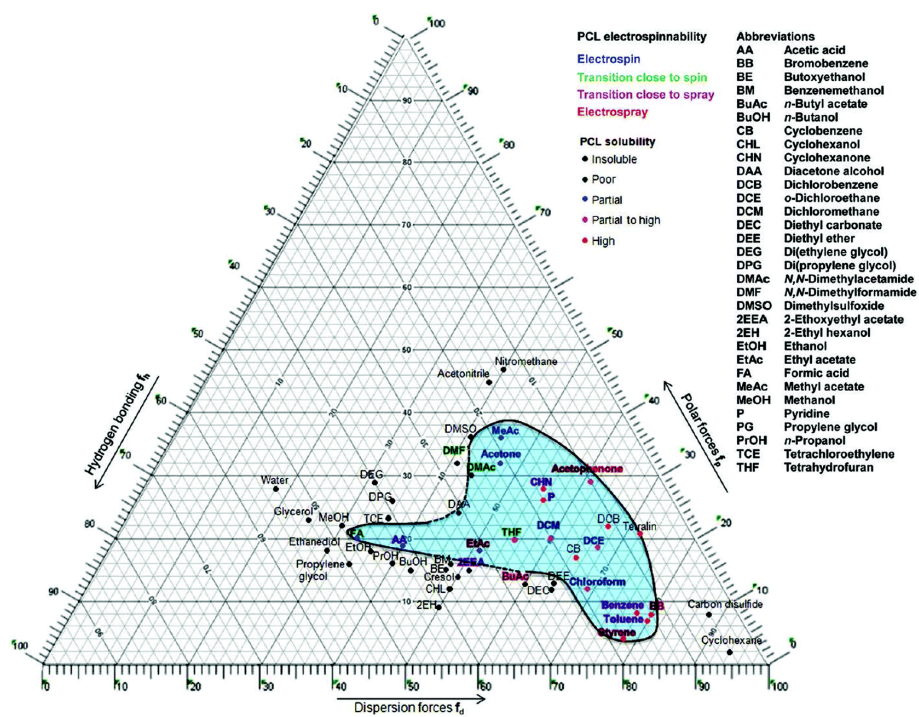
Figure 14. Spinnability-solubility map for PCL solution electrospinning based on the Teas graph, tested at 10% w/w PCL concentration, 1 atmospheric pressure, and ambient temperature of 20-22 ºC. The shaded region enclosed by a contoured outline shows the solubility map of PCL. Dotted lines on this contour indicate the poor solvents on the map shown immediately beyond the shaded region will dissolve PCL and form stable solutions past 30 °C[94].

The scaffold design shall contribute to guiding cells towards its architecture. In this sense, the scaffold should present two different layers, one devoted to the migration of EC and the other one to SMC. EC are distributed as a monolayer in contact with blood, aligned with the bloodstream. Coherently, the upper layer of the scaffold should have its fibers aligned with the bloodstream. SMC constitute a wide network in the aorta's wall. The microstructure of the opposite layer should allow this kind of cells to slowly progress through the pores and colonize the scaffold. In this sense, SMC do not need for a well-organized microstructure to proliferate so fibers in this layer should be randomly distributed.

One of the main reasons for choosing electrospinning to create the scaffold is because it allows creating porous meshes with low stiffness if the operational parameters are well adjusted. Current grafts and endografts are hybrid products composed of a polymer mesh manufactured with either Dacron (polyester) or expanded polytetrafluoroethylene (ePTFE), together with metallic stents that provide radial support[96]. Fibers are knitted or woven together giving the final product a Young's modulus superior to 20 MPa. Such elevated stiffness is one of the main reasons for these treatments to fail over time, because a diseased aorta has a Young's modulus of 3.15 ± 3.31 MPa[97]. The mechanical mismatch that current stent grafts present could be overcome with an electrospinning-based scaffold. To set the range of acceptance of the new scaffold, the Young's modulus of a healthy aorta (1 MPa) was also considered. Therefore, the range of acceptance of the desired scaffold was set to be 2 ± 1 MPa.

2.2   Objectives of the chapter

The main objective of this chapter is to create a scaffold with a microstructure able to mimic the aorta's biomechanical environment. The scaffold should comply with the artery's movements and accompany the aorta in every distention and recoil sequence. The scaffold should promote tissue ingrowth so the surrounding cells should have been able to colonize the space where the scaffold was. The scaffold's microstructure should serve both purposes. Since the phenotype of EC and SMC is different, the microstructure designed for each cell type should be different too. Therefore, the scaffold created should present two different layers to provide the best environment for each cell type.

To do so, three specific goals have been stablished:

1. Define and optimize general electrospinning operational parameters.
2. Optimize the operational parameters that achieve a microstructure that fits the cell environment requirements using a design of experiments.
3. Translate the manufacturing process from a laboratory prototype to an industrially validated process.

2.3 Results

2.3.1 Defining the general parameters

Operational parameters[98], such as tip to collector distance, pump rate, voltage applied to the solution and the collector where the fibers are deposited, can be adjusted to obtain the desired fiber morphology. A complete study of these parameters was performed using PCL and chloroform as polymer and solvent of choice, respectively, and squalene (Sq), as a viscous additive used as a plasticizer, described to possess preventive properties against atherosclerotic lesions among others[99]. Sq could help in creating a more biocompatible and anti-inflammatory microstructure. The samples generated were first analyzed by Scanning Electron Microscopy (SEM) to evaluate more accurately the microstructure and then strain-stress tests were performed to determine their Young's Modulus and compare it to that of the aorta. The solution to test the operational parameters was formed by 12% of PCL dissolved in chloroform and with 2.4% of Sq.

The first operational parameter evaluated was the pump's flow rate. Three different values were tested, 1000 μL/h, 2000 μL/h and 3000 μL/h, while keeping the distance fixed at 23.0 cm (this distance was chosen considering previous results[100]). SEM images are shown in Figure 15 and Figure 16. The top surface of the three samples was dense and compact, but still having interconnected pores in all of them. Inside, the fibers in all samples had heterogeneous sizes. The Young's modulus was in the three cases similar and in the range of acceptance, but the sample's microstructure was far from being suitable for cell growth.
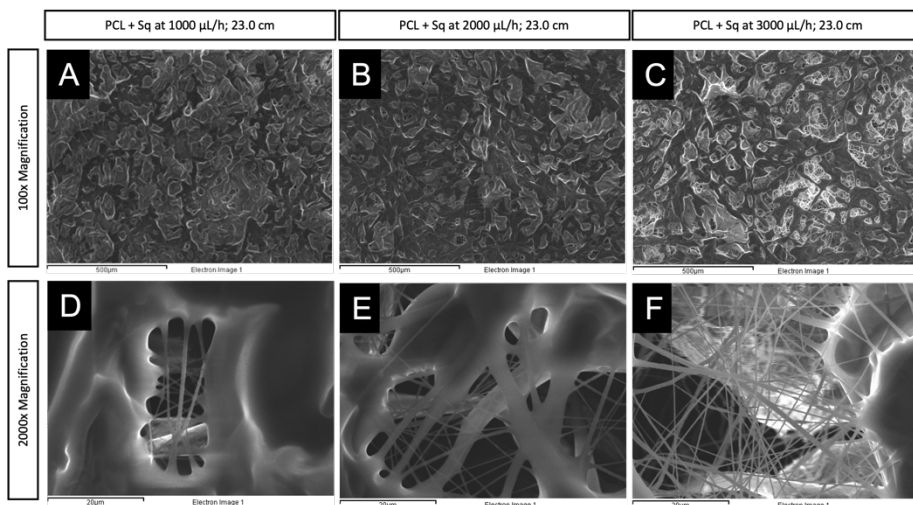
Figure 15. SEM images obtained for pump flow rate testing using PCL and Sq mixture. A, B and C images were taken at 100x magnification and D, E and F were taken at 2000x magnification. A and D correspond to 1000 µL/h, B and E to 2000 µL/h and C and F to 3000 µL/h.

Figure 16. Young's Modulus values obtained for each sample in Figure 15.

The flow rate was fixed at 2000 µL/h to test how distance affects the fiber morphology and its mechanical properties. Results are represented in Figure 17 and Figure 18. Besides, the microstructure using 24.5 cm distance appears to be slightly more homogeneous, fiber diameters were less variable, but the top surface of all samples was still too compact.
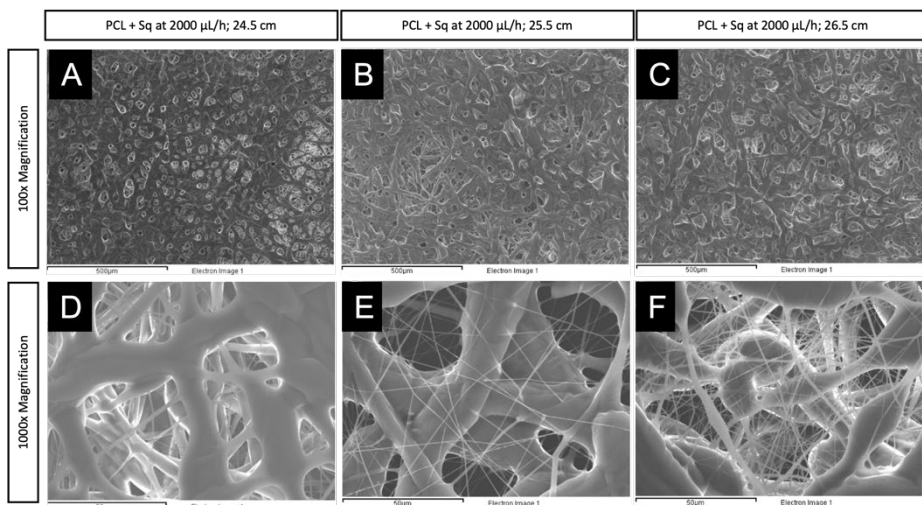
Figure 17. SEM images obtained for the tip to collector distance using PCL and Sq mixture. A, B and C images were taken at 100x magnification and D, E and F were taken at 1000x magnification. A and D correspond to 24.5 cm, B and E to 25.5 cm and C and F to 26.5 cm.
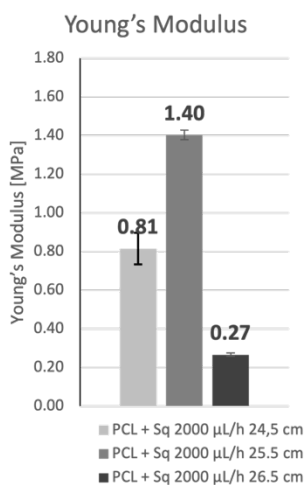
Figure 18. Young's Modulus values obtained for each sample in Figure 17.

The compact surface was thought to be due to the presence of Sq[101] in the electrospun mixture. To demonstrate so, all the tests were repeated using the same operational parameters but this time using a polymeric solution of PCL only. The results for the flow rate test are shown in Figure 19 and Figure 20.
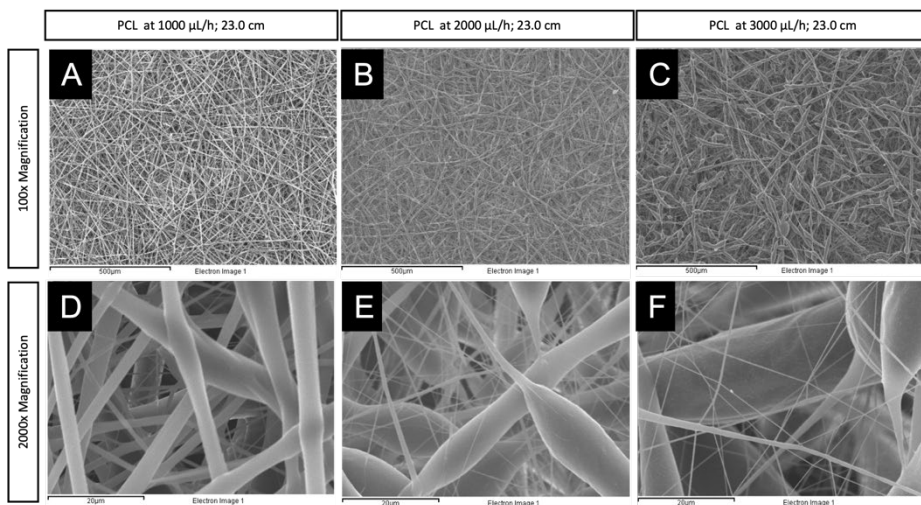
Figure 19. SEM images obtained for pump flow rate testing using PCL-only mixture. A, B and C images were taken at 100x magnification and D, E and F were taken at 2000x magnification. A and D correspond to 1000 µL/h, B and E to 2000 µL/h and C and F to 3000 µL/h.
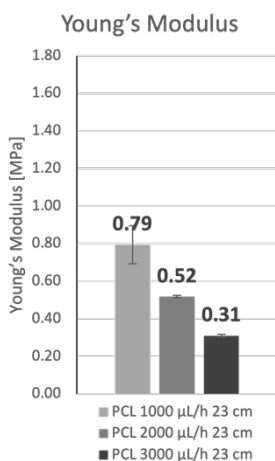
Figure 20. Young's Modulus values obtained for each sample in Figure 19.

Microstructure was clearly more homogeneous after eliminating Sq. The top surface of all samples was less compact, and fibers could be perfectly identified. All samples presented beads but more significantly at 3000 µL/h. This may be caused by incomplete solvent evaporation. Defective fibers with beads and ribbon-like morphology are formed when the solution feed rate is increased beyond its optimum processing window, preventing the solvent to complete its evaporation.

41
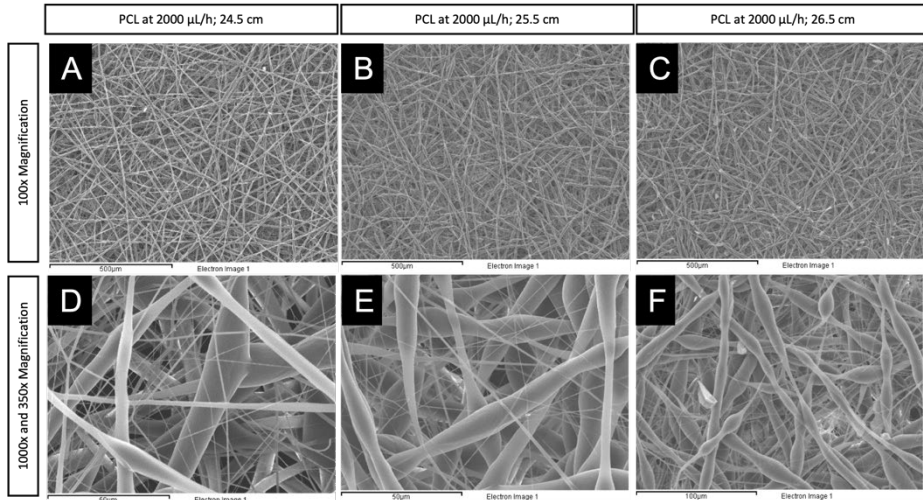
Figure 21. SEM images obtained for the tip to collector distance using PCL-only mixture. A, B and C images were taken at 100x magnification and D and E were taken at 1000x and F was taken at 350x magnification. A and D correspond to 24.5 cm, B and E to 25.5 cm and C and F to 26.5 cm.
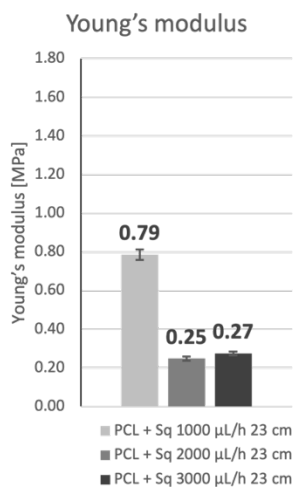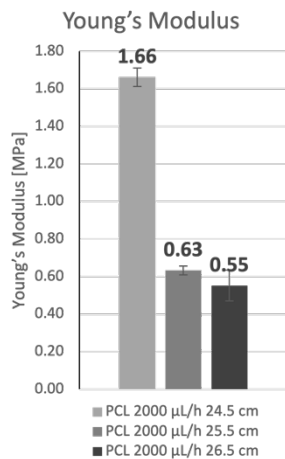

Figure 22. Young's Modulus values obtained for each sample in Figure 21.

The flow rate was fixed again at 2000 µL/h to test how distance affects the fibers' morphology and the mechanical properties. Results are represented in Figure 21 and Figure 22. The microstructure was clearly more homogeneous at 24.5 and 25.5 cm, while presenting beads at 26.5 cm. There was still room

for improvement in the fibers microstructure, but the flow rate was set at 2000 µL/h because fibers appeared to be more homogeneous at all distances.

Moreover, there was a need for a method to better evaluate and quantify the differences in the fibers produced using the different parameters. Hence, from this point on, all SEM images generated were analyzed using ImageJ plugin OrientationJ (see section 5.1.7 for the complete method). This plugin determines fiber diameter, porosity, and fiber orientation for each SEM image. This method was used to evaluate differences in fiber diameter when changing the distance from the tip to the collector (Table 1).

Table 1. Characterization of the samples created using different values of tip to collector distance.

Tip to collector distance (cm)	Thickness ± SD (mm)	E ± SD (Mpa)	Fiber Diameter ± SD (µm)	Porosity ± SD (%)
23.0	0.15 ± 0.01	2.28 ± 0.70	3.19 ± 0.34	51.0 ± 3.0
23.5	0.16 ± 0.01	2.53 ± 0.28	3.05 ± 0.46	50.0 ± 0.7
24.0	0.16 ± 0.01	0.85 ± 0.16	3.71 ± 0.64	51.0 ± 1.0
24.5	0.18 ± 0.01	1.47 ± 0.18	N.A.	N.A.
25.0	0.17 ± 0.01	1.48 ± 0.12	3.13 ± 0.61	51.0 ± 1.0
25.5	0.17 ± 0.01	1.20 ± 0.30	3.45 ± 0.34	51.0 ± 0.9
26.0	0.18 ± 0.01	1.37 ± 0.20	3.56 ± 0.39	50.0 ± 3.0
26.5	0.16 ± 0.01	1.44 ± 0.39	3.96 ± 0.53	51.0 ± 0.9

After processing all SEM images, it was observed that increasing the tip to collector distance did not result in an increase in fiber diameter. At this point, the only operational parameter left to be tested was the collector type since the voltage applied to the sample depends on all the other parameters and must be adjusted at the beginning of every electrospinning process. The collector was changed from flat to rounded to produce aligned fibers.

Considering the results obtained in previous projects developed in our scientific group[100], it was decided to use the previously established parameters with the drum collector at 400 rpm. The results are represented in Figure 23 and Figure 24.
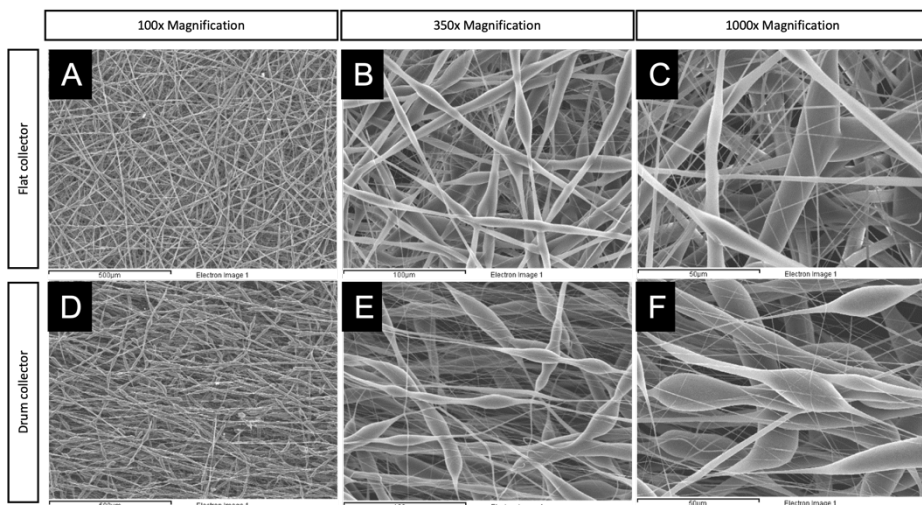
Figure 23. SEM images obtained using two different collectors (using PCL-only mixture). A and D images were taken at 100x magnification, B and E images were taken at 350x magnification and C and F were taken at 1000x magnification. A, B and C correspond to the samples obtained with the flat collector at 24.5 cm distance; and D, E and F correspond to the samples obtained with the drum collector at the same distance.
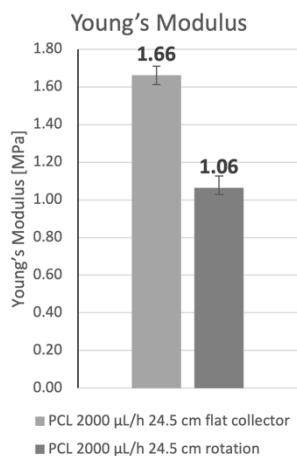
Figure 24. Young's Modulus values obtained for each sample in Figure 23.

Fibers obtained using the drum collector presented a certain tendency to be aligned in one direction while fibers deposited on the flat collector seemed completely randomly distributed along the surface. A wide analysis on fiber orientation of the drum collector fibers was performed in the next

experiment. In both cases though, fibers presented formation of beads along their length, and fiber diameters were not homogeneous.

At this point, other factors had to be explored to understand what may be affecting the fibers' morphology. Ambient conditions were always measured but their variation was minimal (temperature 22.6 ± 1.7 ºC and humidity of 40.6 ± 3.9%). Furthermore, the equipment used could not control ambient conditions inside the chamber. Another factor that may affect fiber morphology could be the pumping syringe. Normally, 2 mL of solution were electrospun for each sample and a 2.5 mL syringe was used. Pumping the solution from a syringe which total volume is very similar to the volume that is being electrospun could cause that the last solution electrospun is not in a steady state which could affect its fiber morphology. Therefore, it was decided to change the syringe from 2.5 mL to the 5 mL to electrospin one layer of material (2 mL) (Figure 25). Fiber morphology was considerable improved by only changing the syringe. Fiber diameter became constant along each fiber and bead presence was remarkably reduced. Moreover, it was decided to electrospin two layers of material in the same electrospinning process to create the desired scaffold. To do so, a first layer of material (2 mL) was electrospun over the drum collector at 0 rpm (using the established conditions for 5.0 mL syringe). A second layer of material (2 mL) was then electrospun at 400 rpm. This process was performed also for the 2.5- and 5.0-mL syringes.
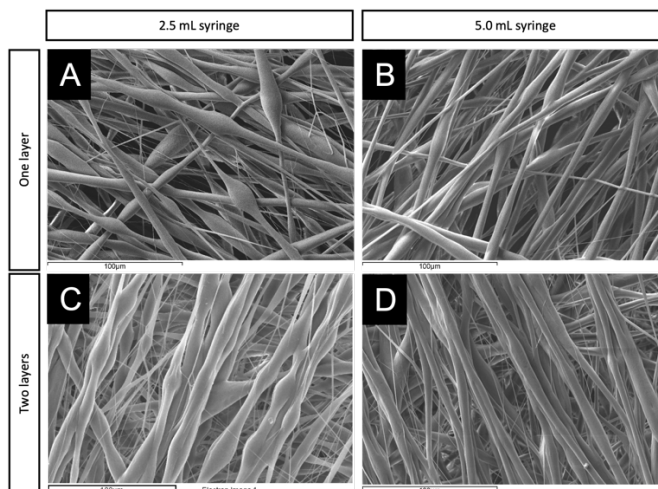
Figure 25. SEM images obtained using two different syringe volumes: 2.5 mL and 5 mL; using the drum collector in all cases. All the images were taken at the same magnification (550x). A and C images correspond to the samples obtained with the 2.5 mL syringe. B and D images correspond to the samples obtained with the 5 mL syringe. A and B correspond to only one layer of material and, C and D correspond to two layers of material (same drum collector speed was used in all cases, 400 rpm)

Qualitatively, fibers tended to be aligned when using the 5 mL syringe and when two layers of material are electrospun in the same sample. Thanks to ImageJ this tendency was quantified. All samples represented in Figure 25 were further analyzed by ImageJ software to compare the changes by using different volume syringes and layers of material while keeping invariable all the other electrospun parameters (Figure 26).
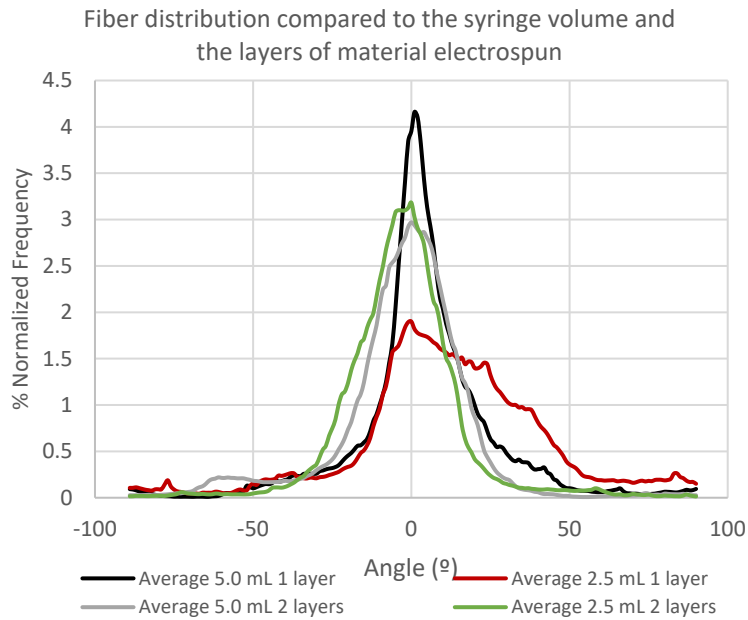
Figure 26. Fiber distribution compared to the syringe used to manufacture each sample and the layer of material electrospun in each case.

The analysis evidences the differences in fiber orientation. Electrospinning 1 layer of material (2 mL) resulted in a very poor alignment of the fibers compared to the great alignment produced with the 5.0 mL syringe. When two layers of material were electrospun, there were no differences in the fiber alignment compared to the 2.5- or 5.0-mL syringes. This effect is thought to be because the random layer stabilizes the electrostatic charges of the sample, and the alignment is consequently better.

The Young's modulus was not measured for all samples because the focus was the fiber orientation. The best conformation was the 2 layers mat electrospun with the 5 mL syringe because using the 5.0 mL syringe allows to manufacture both layers without stopping the process. Creating the sheet of material without stops results in a better cohesion of both layers. The Young's modulus was determined to be 1.81 ± 0.24 MPa for this sample. At this point, all the parameters were studied but there was still room for improvement. Therefore, a design of experiments was used to perform a wider optimization.

2.3.2　Optimization of fiber morphology and distribution using Simplex

The operational parameters were optimized to achieve acceptable fiber diameter, homogeneity, and alignment in both layers of the scaffold using the Simplex method (see section 5.1.8).

The variables chosen were the tip to collector distance, the concentration of PCL, the solvent used, and the rotator speed, each with its own variation step (Figure 27). The principal output was fiber diameter homogeneity. Each layer of the scaffold was manufactured using a different rotator speed; therefore, the optimization of each layer was performed separately.

Variable	V	Initial value (IV)	Variation step (VS)
Tip to collector distance	1	24.5 cm	0.5 cm
PCL concentration	2	12%	2%
Solvent (% Chloroform)	3	0.8	0.1
Rotator speed (rpm)	4	0 (Random) 400 (Aligned)	0 (Random) 50 (Aligned)

$$V = IV + VS * factor$$
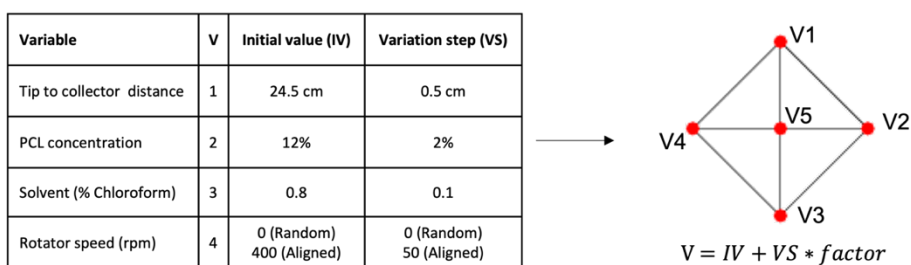
Figure 27. Simplex optimization for four variables. On the left, there is a table containing the variables studied for the optimization of the fiber morphology, their initial value, and the variation step. On the right, the geometric figure representing the simplex optimization for four variables and the equation used to calculate the values of the first optimization step.

The optimization process was also used to test the effect of introducing another solvent to the mixture, dimethyl formamide (DMF). This solvent has a higher boiling point compared to chloroform, 152.0 ºC, and higher dielectric constant, 36.7 (at 20 ºC). Although the boiling point raises with the incorporation of DMF to the solution, the dielectric constant does it too and this probably result in improving the nanofiber formation process. Changing the solvent directly affects the viscosity of the mixture and therefore the way it is electrospun. Because of that, the viscosity of all solutions was measured before electrospinning them.

The process in all the simplex optimization was the same. Solutions were prepared and their viscosity was measured using a rheometer at ambient temperature. After the electrospinning process, samples were analyzed using SEM microscopy and the Young's Modulus was calculated from tensile tests. The thickness of all samples was measured with a caliper and the fiber diameter was calculated with the ImageJ software.

The first layer optimized was the random layer. In the first electrospun sample, the distance of 24.5 cm was detected to be very high for the conditions tested (notice that the collector used in all the optimization process was the drum collector, therefore, some of the already stablished parameters needed to be re-adjusted) (Table 2 and Figure 28).

Table 2. Parameters tested in the optimization of the random fibers and the viscosity measured for each solution.

Sample	Distance (cm)	% PCL	% CHCl$_3$	Viscosity (Pa·s)
Starting point (R0)	24.5 (flat collector)	12.0	100	0.782
Random1 (R1)	20.0	12.0	80.0	0.797
Random2 (R2)	21.0	12.0	80.0	0.900
Random3 (R3)	20.5	13.7	80.0	1.415
Random4 (R4)	20.5	12.6	88.2	0.834
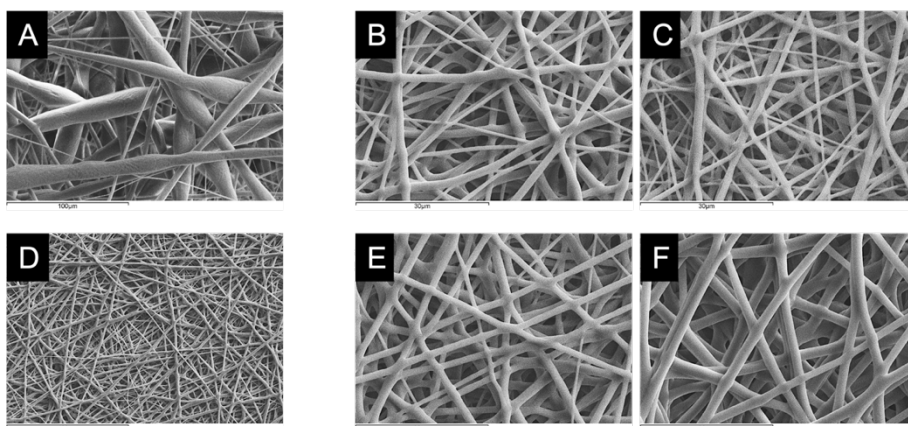
Figure 28. SEM images obtained in the optimization process of the random fibers. A and D SEM images are at 550x magnification and C, D, E and F images are at 2000x magnification. A SEM image corresponds to the starting point sample. B and D SEM images correspond to the Random1 sample, C SEM image corresponds to Random2 sample, and so on.

A great improvement was observed in the fiber's morphology in all samples. Fiber diameter size was reduced overall a 60%, the presence of beads disappeared, and fiber diameters in all samples looked more homogeneous. The visual optimization was confirmed analyzing the data with ImageJ (Table 3). The mechanical properties were also tested, and Young's Modulus increased in all the samples but was still in the acceptance range in most of the cases (Figure 29 and Figure 30).

Table 3. Thickness measured, Young's Modulus values and the fiber diameter of each sample in the simplex optimization for the random fibers.

Sample	Thickness ± SD (mm)	E ± SD (Mpa)	Fiber Diameter ± SD (µm)
Starting point	0.30 ± 0.01	2.17 ± 0.04	3.71± 0.64
R1	0.20 ± 0.01	3.84 ± 0.06	1.38 ± 0.19
R2	0.20 ± 0.01	2.77 ± 0.07	1.47 ± 0.18
R3	0.18 ± 0.01	6.40 ± 0.11	1.54 ± 0.21
R4	0.22 ± 0.01	5.02 ± 0.25	1.60 ± 0.22

Figure 29. Young's Modulus' values for random fibers in the simplex optimization.
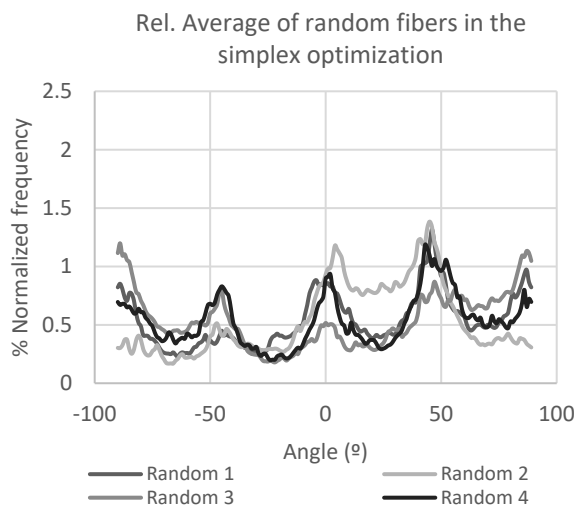
Figure 30. Fiber distribution represented for each sample in the simplex optimization for random fibers.

After the first Simplex optimization step, the objective was accomplished, and the optimization process of the random layer was stopped at this point. The best sample was decided to be the random 2, manufactured at 21.0 cm distance from the tip to the collector. And changing the solvent from the mixture of chloroform and DMF appeared to be a great solution for the homogeneity of the fiber diameter and morphology. Next step was to start with the Simplex optimization for the aligned layer. In this case, four different variables were studied since different rotator speeds were tested.

Table 4. Parameters tested in the optimization of the aligned fibers and the viscosity measured for each solution.

| Sample	Distance (cm)	% PCL	% CHCl3	Viscosity (Pa·s)
Starting point	24.50	12.00	100	0.782
Aligned1 (A1)	24.50	12.00	80.0	0.797
Aligned2 (A2)	25.00	12.00	80.0	0.900
Aligned3 (A3	24.75	13.74	80.0	1.415
Aligned4 (A4)	24.75	12.58	88.2	0.834
Aligned5 (A5)	24.75	12.58	82.0	0.797

52
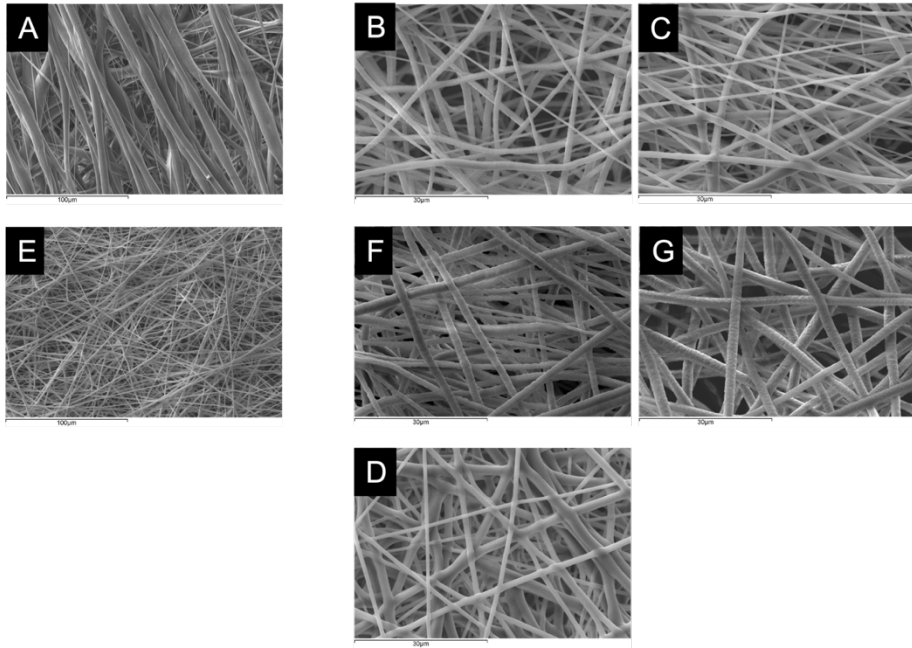
Figure 31. SEM images obtained in the optimization process of the aligned fibers. A and B SEM images are at 550x magnification and C, D, E and F images are at 2000x magnification. A SEM image corresponds to the starting point sample. B and C SEM images correspond to the Random1 sample, D SEM image corresponds to Random2 sample, and so on.

Even though fiber morphology and homogeneity were optimized, the fibers did not present the desired alignment (Figure 31). Regardless of the SEM results, ImageJ analysis was performed, and the Young's Modulus was calculated for each sample (Table 5 and Figure 32 and Figure 33).

Table 5. Thickness measured, Young's Modulus values and the fiber diameter of each sample in the simplex optimization for the aligned fibers.

Sample	Thickness ± SD (mm)	E ± SD (Mpa)	Fiber Diameter ± SD (µm)
Starting point (2 layers)	0.31 ± 0.01	1.81 ± 0.24	3.37 ± 0.32
Aligned1	0.03 ± 0.01	9.69 ± 0.36	1.23 ± 0.10
Aligned2	0.02 ± 0.01	12.55 ± 0.78	1.16 ± 0.09
Aligned3	0.07 ± 0.01	5.17 ± 0.20	1.27 ± 0.10
Aligned4	0.03 ± 0.01	6.94 ± 0.16	2.11 ± 0.58
Aligned5	0.03 ± 0.01	9.32 ± 0.14	1.51 ± 0.44

Young's Modulus for the aligned fibers in the simplex optimization
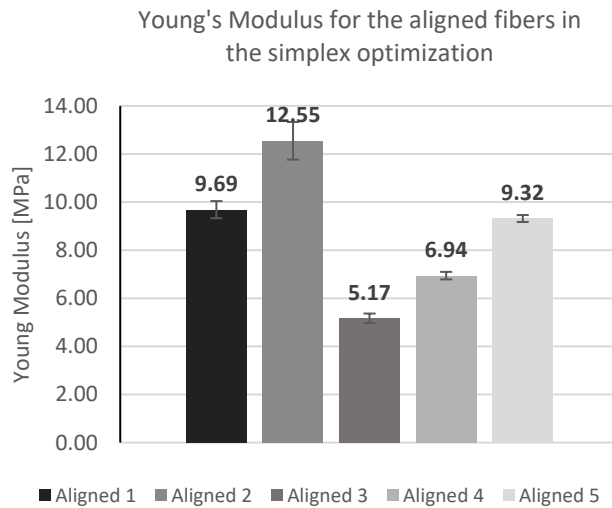
Figure 32. Young's Modulus' values for aligned fibers in the simplex optimization.

Rel. Average of aligned fibers in simplex optimzation
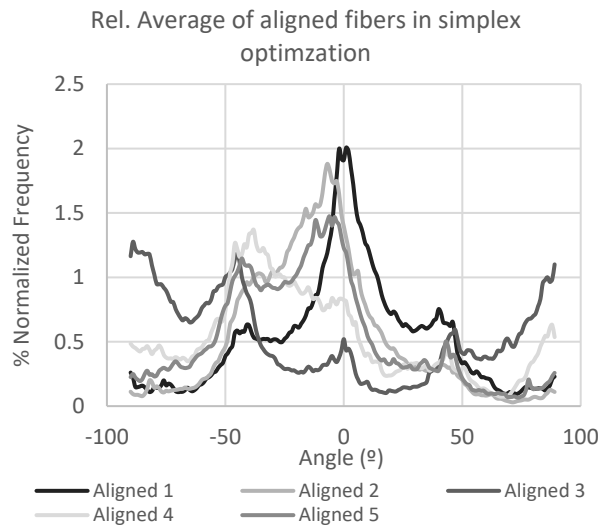
Figure 33. Fiber distribution represented for each sample in the simplex optimization for aligned fibers.

The Young's Modulus in all samples was higher than in the starting point therefore, demonstrating that the new fiber conformation generated stiffer macrostructure. On the other hand, the fiber distribution analyzed by ImageJ confirmed that, even though there were some preferred angles, fibers were not aligned in parallel. Simplex was a good starting point to optimize the fiber

morphology and homogeneity but, it was not enough to reach the level of fiber alignment required for this thesis. Therefore, we went back to the trial-and-error optimization basis. The PCL concentration (at 12% (w/v)) and the new solvent mixture (chloroform and DMF (80:20)) were kept invariable as they seemed to have a good influence in fiber morphology. For the first trial, the rotator speed was also kept invariable at 400 rpm as per the good results obtained in previous samples. Therefore, the parameter tested was the tip to collector distance. Three different distances were tested (20.0, 18.0 and 15.0 cm) using one layer of material (2 mL) (Figure 34).
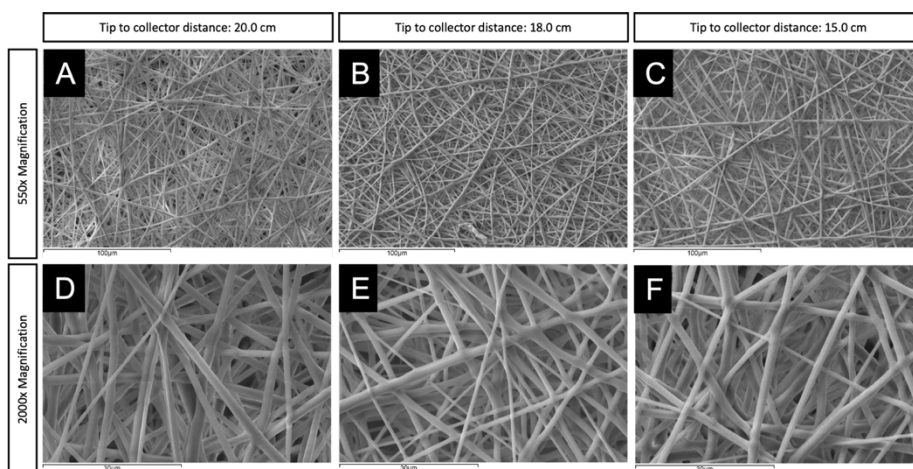
Figure 34. SEM images obtained in the optimization process of the aligned fibers at different tip to collector distances with one layer of material. A, B and C SEM images are at 550x magnification and D, E and F images are at 2000x magnification. A and D SEM images correspond to 20.0 cm distance from the tip to the collector. B and E SEM images correspond to 18.0 cm distance from the tip to the collector. C and F SEM images correspond to 15.0 cm distance from the tip to the collector.

It was clear that while fibers have a good morphology, they were still not aligned. Higher alignment was observed in previous tests when electrospinning two layers of material. Therefore, the same conditions were repeated but electrospinning two layers of material (4 mL) since this resulted in an optimized alignment in previous tests (Figure 35).
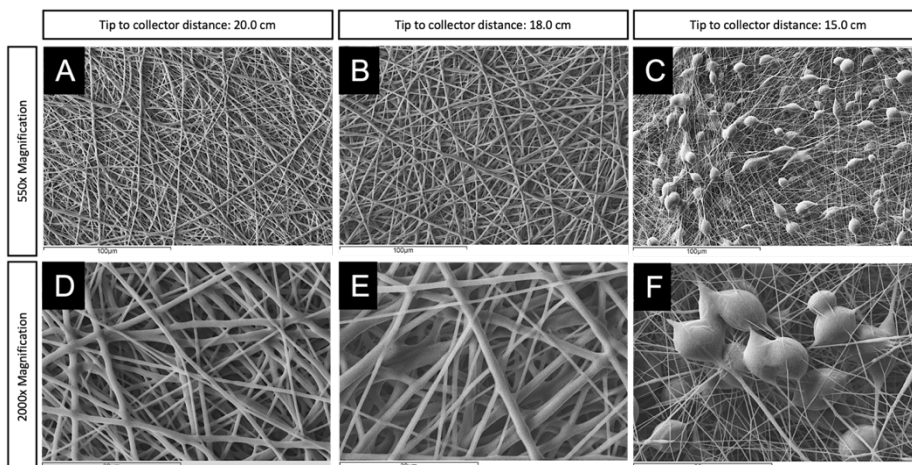
Figure 35. SEM images obtained in the optimization process of the aligned fibers at different tip to collector distances with two layers of material. A, B and C SEM images are at 550x magnification and D, E and F images are at 2000x magnification. A and D SEM images correspond to 20.0 cm distance from the tip to the collector. B and E SEM images correspond to 18.0 cm distance from the tip to the collector. C and F SEM images correspond to 15.0 cm distance from the tip to the collector.

Fiber alignment was clearly not improved after electrospinning two layers of material, so the strategy decided was to maintain the distance from the collector while increasing the speed of the rotator. Neither tensile tests nor ImageJ analysis were performed since alignment was worse than the objective. Therefore, two different speed values were tested: 1,000 and 2,000 rpm; and the other variables were: PCL concentration at 12% (w/v), the new solvent mixture (chloroform and DMF (80:20)) and the distance after the last tests was set at 18.0 cm (flow rate was always invariable at 2,000 μL/h).
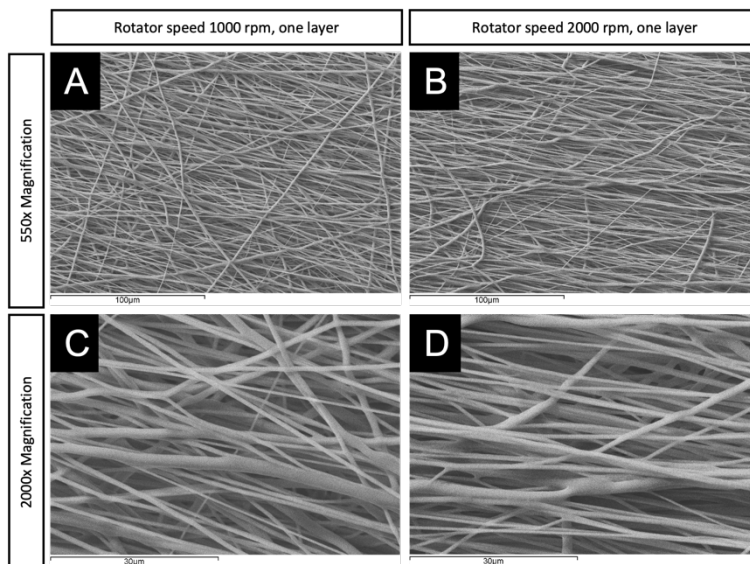
Figure 36. SEM images obtained in the optimization process of the aligned fibers at rotator's speed with one layer of material. A and B SEM images are at 550x magnification and C and D SEM images are at 2000x magnification. A and C SEM images correspond to 1,000 rpm rotator speed. B and D SEM images correspond to 2,000 rpm rotator speed.

Increasing the rotator speed resulted in the production of more aligned fibers but there was still room for improvement. Fibers at 2,000 rpm looked more aligned than at 1,000 rpm but, since we were working at machine speed limits, the sample wrinkled at the time of removing the sheet from the drum (Figure 36). Consequently, we decided to repeat the test having two layers of material and test two different rotator speed, 1,000 and 1,500 rpm (Figure 37).
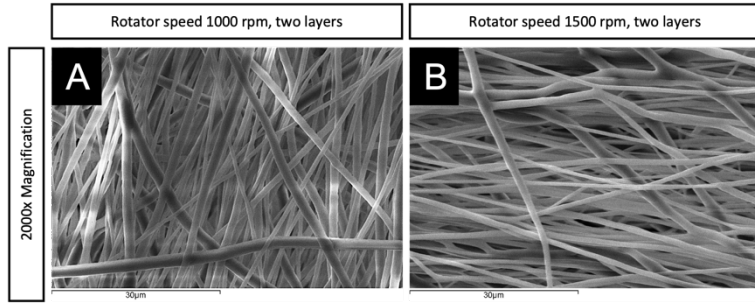
Figure 37. SEM images obtained in the optimization process of the aligned fibers at rotator's speed with two layers of material. Both SEM images are at 2000x magnification. A SEM image correspond to 1,000 rpm rotator speed and B SEM image correspond to 1,500 rpm rotator speed.
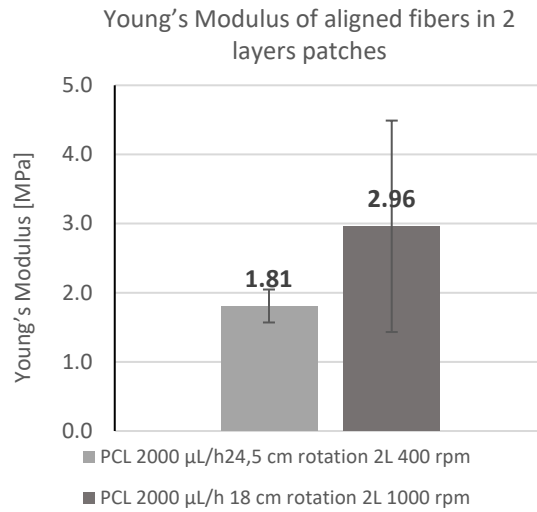
Figure 38. Young's Modulus' values for each sample in 2 layers patches.

Rel. Average of aligned fibers in 2 layers patches
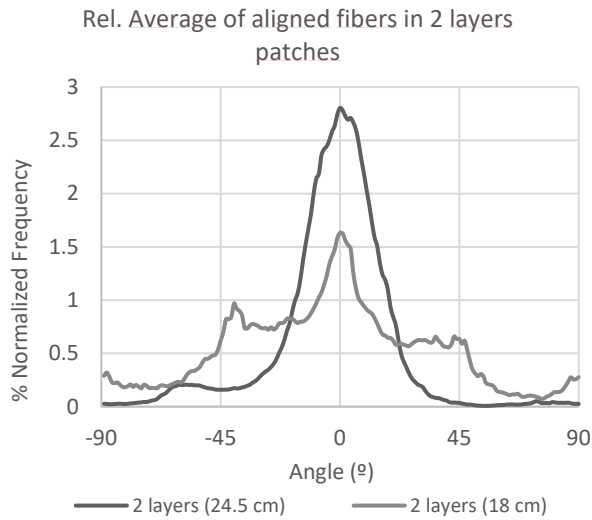
Figure 39. Fiber distribution represented for each sample in 2 layers patches.

After all, there was an improvement in fiber morphology and alignment. We decided that the sample manufactured at 1,000 rpm speed was the conformation that produced the more aligned fibers. This finding was confirmed by performing ImageJ analysis and tension tests to determine the Young's Modulus of the sample (Figure 38). The sample manufactured at 18.0 cm and 1,000 rpm had a higher Young's Modulus compared to the sample manufactured at 24.5 cm and 400 rpm, but still within the acceptance criteria. On the other side, fibers were more aligned than in all the other cases but far from the objective (Figure 39). After testing all the electrospinning parameters, it was decided to follow two different strategies: to contact an industrial partner to start manufacturing electrospinning samples that fit our requirements (see section 2.3.3) and to design a new collector especially dedicated to manufacturing aligned fibers. Inspired by the literature[83,86], we designed a collector that had two bars connected (Figure 40).
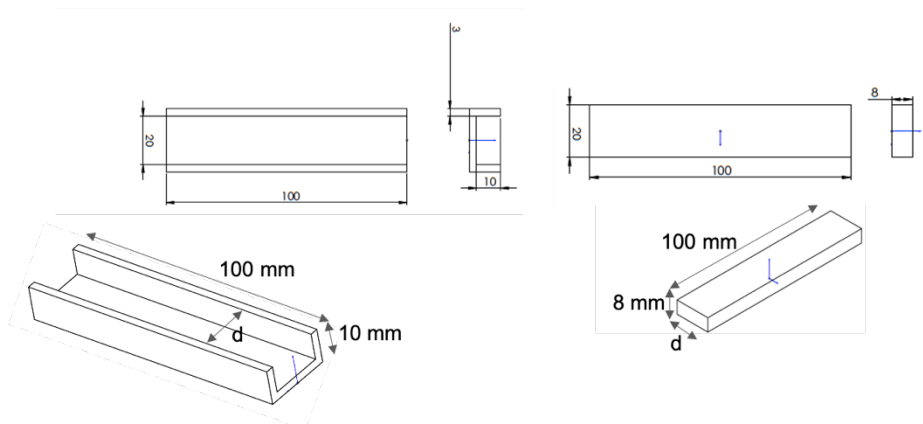
Figure 40. On the left, the double-bar collector design. On the right, the negative of the double-bar collector design.

The double-bar collector was manufactured with a conductor material such as stainless-steal. The collector was placed in a non-conductive platform and connected to ground potential using and specifically designed tweezers (Figure 41). We designed three different double-bar collectors. All of them had the same sizes except for the distance between both bars which was 2.0, 3.0 or 4.0 cm. The first collector tested was the double-bar collector of 2.0 cm distance with only one layer of material (2 mL) (Figure 41).
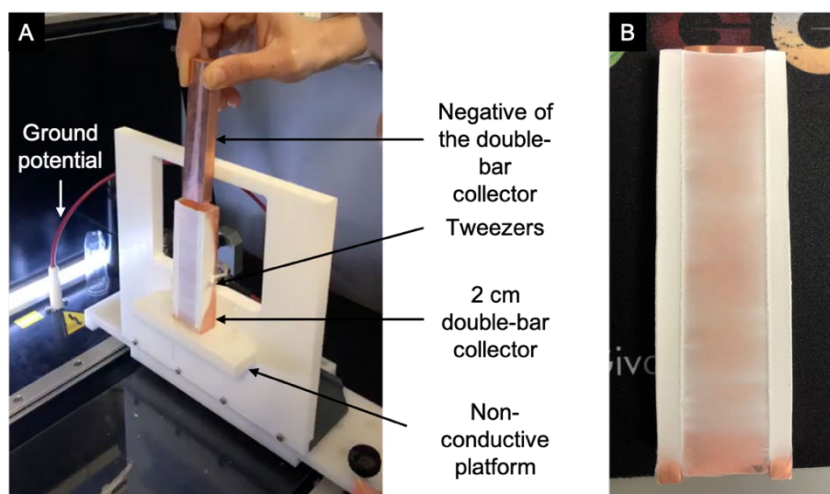
Figure 41. A) Scheme of the double-bar collector setup. B) 2.0 cm double-bar collector after the electrospinning of one layer of material.
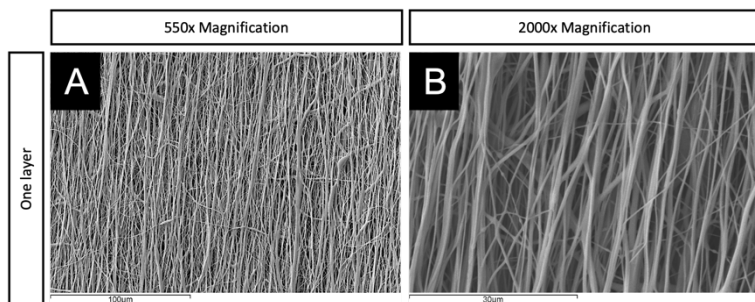
Figure 42. SEM images for the sample manufactured with the 2.0 cm double-bar collector with one layer. A SEM image is at 550x magnification and B SEM image is at 2000x magnification.

Fibers did not have the best morphology, but they presented a clearly aligned pattern. Double-bar collectors of 3.0 and 4.0 cm were then tested but this time electrospinning two layers of material (4 mL) (Figure 43).
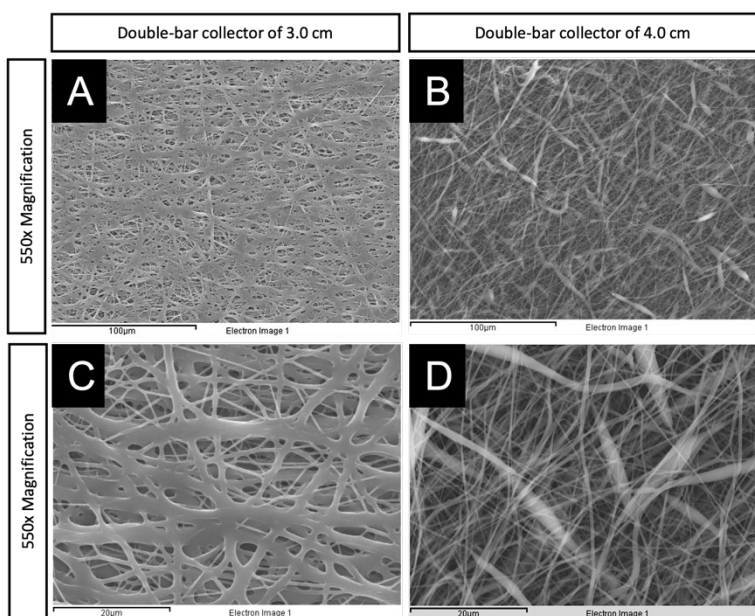
Figure 43. SEM images obtained with the double-bar collector at 3.0 and 4.0 cm bar-distance. A and B SEM images are at 550x magnification and C and D SEM images are at 2000x magnification. A and C correspond to the double-bar collector at 3.0 cm bar-distance and, B and D correspond to the double-bar collector at 4.0 cm bar-distance.

Fiber morphology and alignment were worse than with the 2.0 cm bar-distance collector. This worsening on fiber morphology may be due to using inadequate values of the other operational parameters. To facilitate the process, we decided to return to the 2.0 cm double-bar collector but electrospinning both layers at the same time (Figure 44).
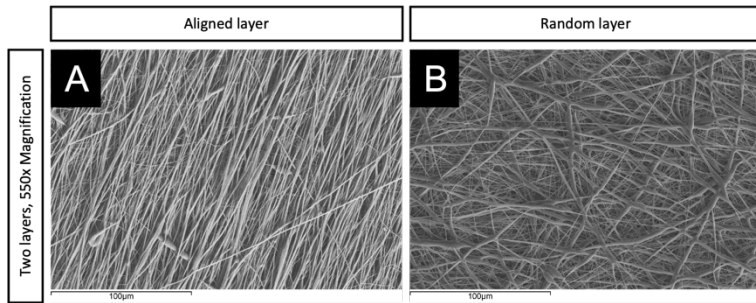
Figure 44. SEM images for the simple manufactured with the 2 cm double-bar collector with one layer of material. Both images were taken at 550x magnification.

SEM images shown in Figure 44 demonstrated that fiber morphology and alignment (Figure 45) were finally optimized and that this collector allowed to manufacture both layers of the scaffold at the same time. Last but not least, we were able to design and manufacture a unique collector.

Table 6. Fiber diameter measured in the 2 cm double-bar collector for the aligned fibers.

Sample	Fiber Diameter ± SD (µm)
2.0 cm double-bar collector	0.813 ± 0.07
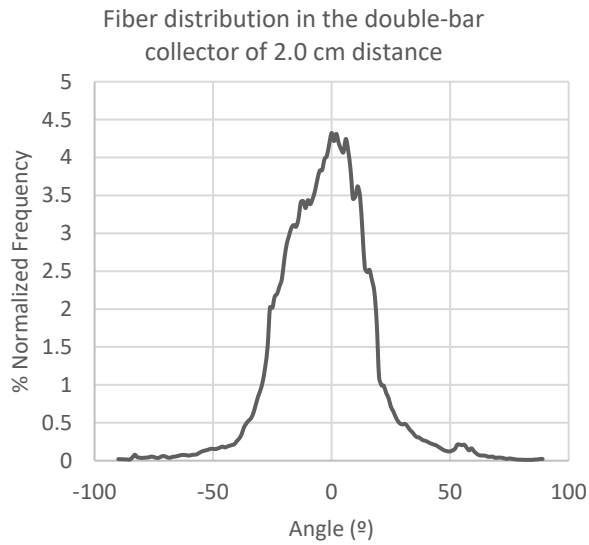
Figure 45. Fiber distribution represented for the 2.0 cm double-bar collector.

Tension tests of these samples were not performed since the samples manufactured were not long enough to perform the tests. Overall, we can conclude that we were able to manufacture at the same time the two layers of our device with the right fiber morphology and distribution.

2.3.3 Industrially scale the manufacturing of our device

The last objective of this chapter was to industrially scale the manufacturing of our device. To do so, two companies were reached out: The Electrospinning Company Limited (TECL) in the United Kingdom (UK) and, Bioinicia in Spain. The requirements of our scaffoled were established after all the design and tests were performed during this first stage of the Thesis. The device should have two different layers: one with fibers aligned and one with fibers randomly distributed. The aligned layer should have a fiber alignment of at least 80 %, and the fiber diameter should be around 1 μm. The random layer should have orthogonal morphology and the fiber diameter should range between 3 and 5 μm. The relation between both layers should be around 1:3 (aligned:random) while the total thickness of the device was not established at this point. After setting the requirements of the samples to be manufactured, each company generated their own samples. From this point on, each company is analyzed separately since their evolution and the samples they provided were different. The details of the conditions used to manufacture each sample are under company property.

2.3.3.1 The Electrospinning Company Limited (TECL)

TECL is a company based in Oxford (UK) specialized in the design, development, and manufacturing of nanofibrous biomaterials for tissue-regenerative devices. In this sense, after sharing our requirements, they manufactured the first samples. SEM images of the first sample manufactured were sent to us (Figure 46).

Figure 46. SEM images for the first trial of TECL manufactured samples. Both SEM images are taken at 500x magnification. A SEM image shows the aligned layer of the device and B SEM image shows the random layer.

The first trial of the TECL manufactured device fulfilled the requirements for the aligned layer since the fiber alignment was more than 80 % and the fiber diameter appeared to be 1.2 ± 0.35 µm. On the other hand, fibers in the random layer did not have an orthogonal morphology and their diameter was less than expected. Further research was not performed in these samples since we did not have any material but only the SEM images. After rearranging the conditions of the electrospinning process, they provided three different samples having the same aligned layer but with different conformations of the random fibers (Figure 47). In this case, we were able to perform tension tests to the samples to correlate the fiber microstructure with the mechanical properties of each sample (Figure 48).
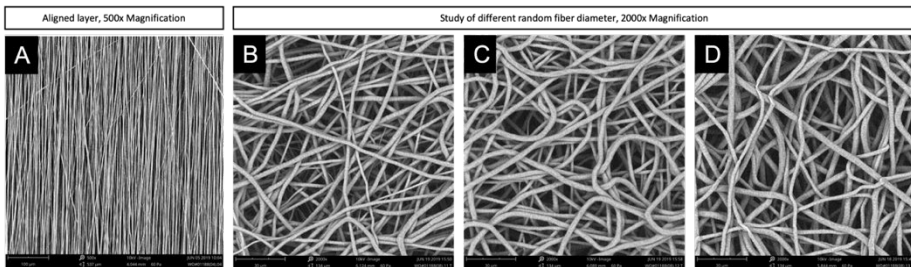
Figure 47. SEM images of the TECL manufactured samples with different random fibers conformations. All the SEM images are taken at 500x magnification. A SEM image shows the aligned layer of the device and B, C and D SEM images show the random layer with the fiber diameter of 2, 3 and 4 µm, respectively.
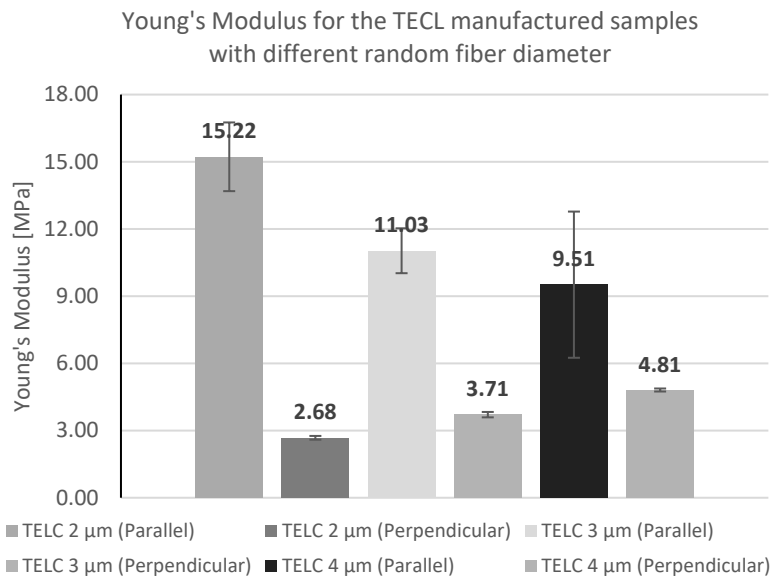
Figure 48.Young's Modulus' values for the TECL manufactured samples at different random fiber diameters. The Young's modulus was tested following the two different directions of the aligned fibers, parallel and perpendicular to the aligned fibers.

The Young's moduli of the TECL manufactured patches were slightly higher (considering only the perpendicular values of the Young's modulus) than the range of acceptance established at the beginning of the process. But this was not considered to be critical for the industrially manufactured patches because there are many parameters to be adjusted in the industrial process. After analyzing both the microstructure and the mechanical properties, it was decided that the best conformation was with the random layer having 3 μm of fiber diameter because fiber diameters were apparently more homogeneous, and the mechanical properties were close to the range of acceptance. The next step was to cut the samples to have smaller pieces of material to test in a biological environment. Moreover, the purpose of our device is to tackle only the affected segment, where the aortic tear is. In this sense, the device was had to be a patch acting as a plaster for the artery. The final shape of the patch was not defined at this point but, the different cutting options were assessed. Therefore, two types of cutting techniques were evaluated: the classical die cut and the use of a laser (Figure 49).
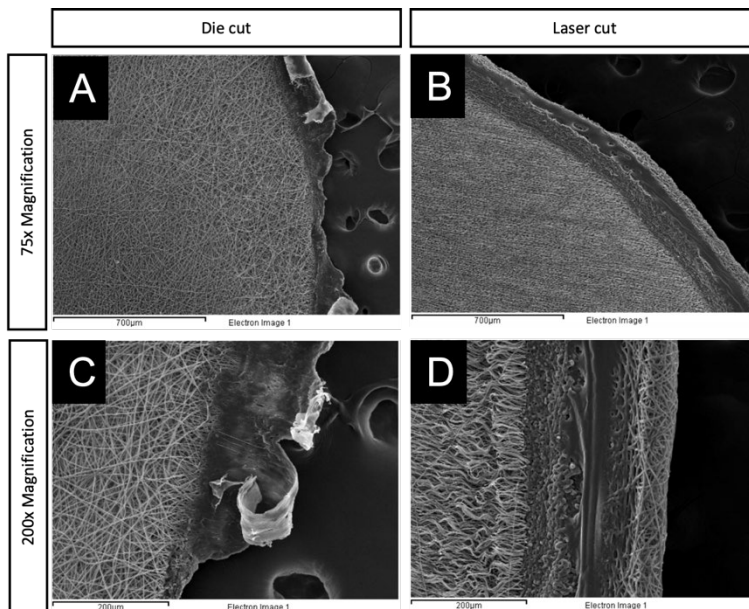
Figure 49. SEM images of the TECL manufactured samples using different cutting techniques. A and B SEM images are taken at 75x magnification and, C and D SEM images are taken at 200x magnification. A and C SEM images correspond to the classical die cut and B and D SEM images correspond to the laser cut.

These samples were used in biological tests and the subsequent results are discussed in the corresponding section.

2.3.3.2 Bioinicia

Bioinicia is a company based in Valencia (Spain) dedicated to the development and manufacture of nano- and micro-structured materials by electrospinning and electrospraying. The process of manufacturing the first sample evolved as with TECL. After sending our requirements, SEM images of the first sample manufactured at Bioinicia's facilities were sent to us (Figure 50). Notice that the first SEM images were taken at Bioinicia's facilities, therefore, the general parameters are different from the images taken at IQS.
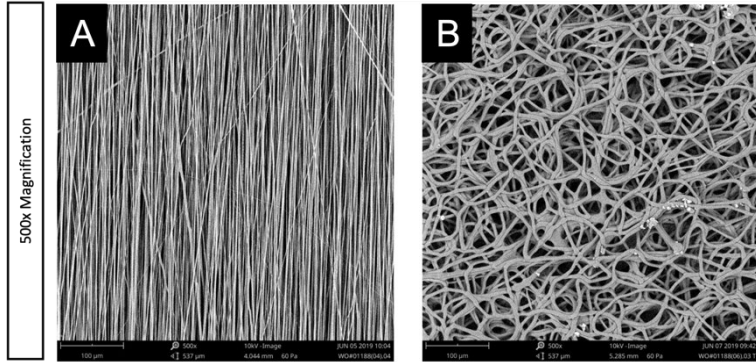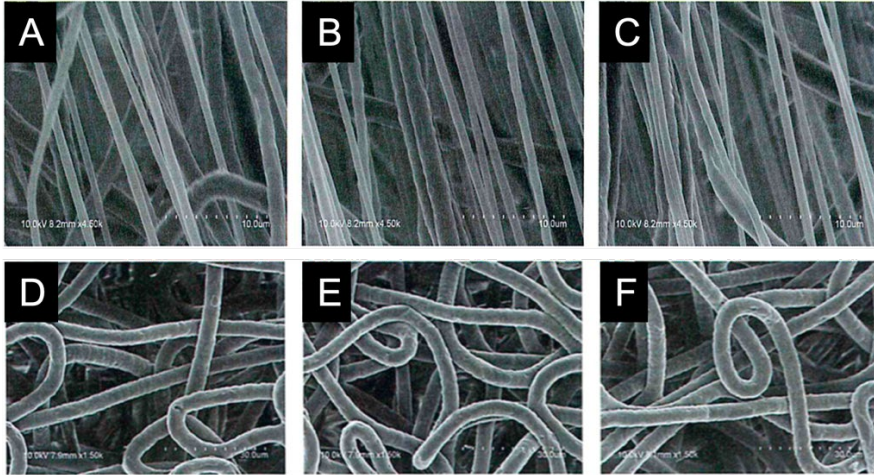
Figure 50. SEM images for the first trial of Bionicia manufactured samples. All SEM images are taken at 50x magnification. A, B and C SEM images show representative images of the aligned layer. D, E and F SEM images show representative images of the random layer.

The analysis performed of the fiber diameter with ImageJ software obtained an average fiber diameter of 4.84 µm (standard deviation of 0.36 µm) for the random fibers and an average fiber diameter of 1.24 µm (standard deviation of 0.76 µm) for the aligned fibers. Moreover, they performed an orientation analysis with the same software obtaining the histograms showed in Figure 51, demonstrating an alignment of more than 70% for the aligned fibers.
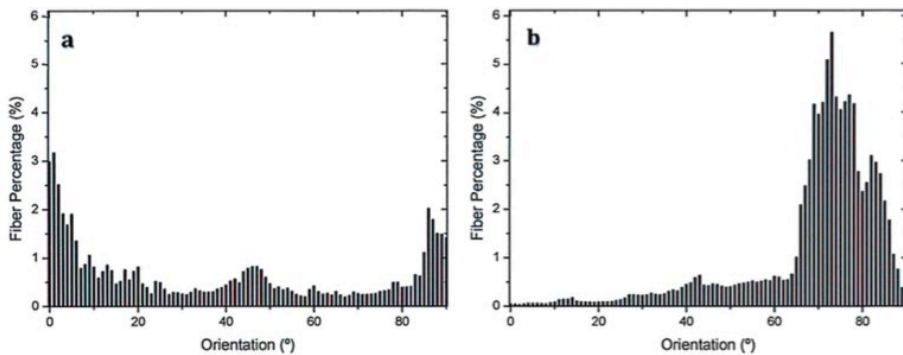
Figure 51. Histogram of the fiber orientation found in (a) Random fibers layer and (b) Aligned fibers layer.

Tension tests were performed to determine the Young's Moduli of the samples manufactured (Figure 52). In this case, stiffness was in the range of acceptance established and the samples provided were less stiff than TECL's.
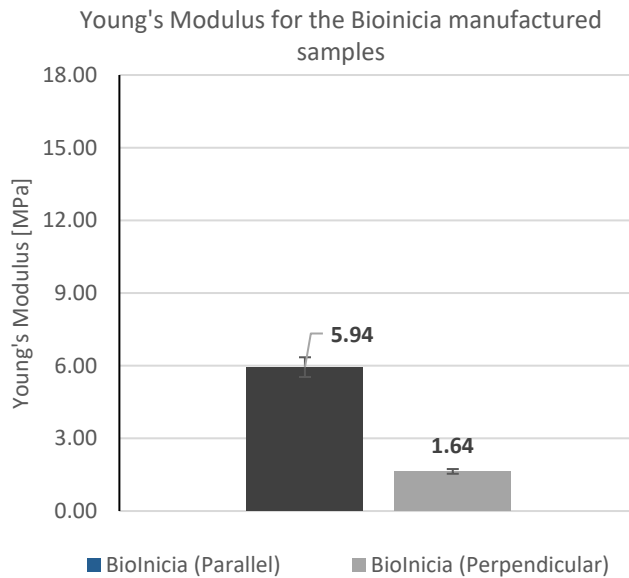
Figure 52. Young's Modulus' values for the sample manufactured at Bioinicia's facilities.

It was decided to continue with the same process and cut the samples in smaller pieces of material to test the microstructure in a biological environment. Therefore, the same two types of cutting techniques were evaluated: the classical die cut and the use of a laser and, the general microstructure was evaluated at IQS facilities (Figure 53).
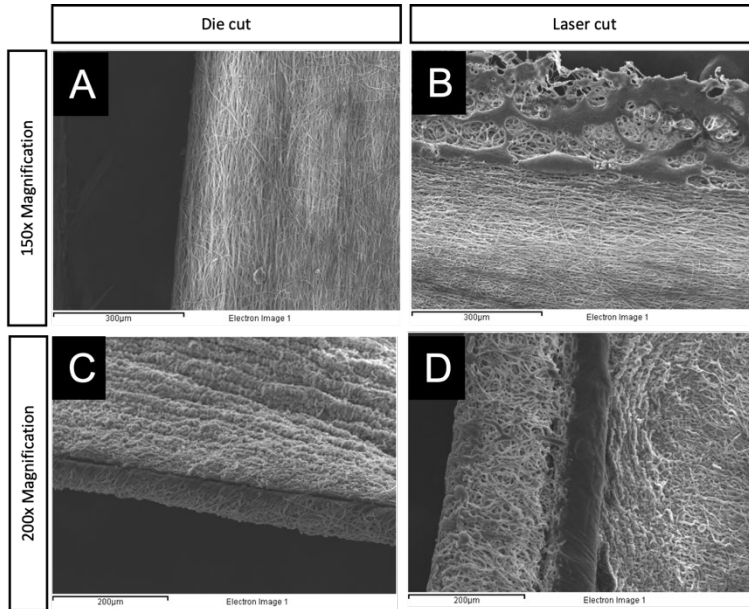
Figure 53. SEM images of the Bioinicia manufactured samples using different cutting techniques. A and B SEM images are taken at 150x magnification and, C and D SEM images are taken at 200x magnification. A and C SEM images correspond to the classical die cut and B and D SEM images correspond to the laser cut.

These samples were used in biological tests and the subsequent results are discussed in the corresponding section.

2.4   Concluding remarks

The main objective of this chapter, creating a scaffold that mimics the biomechanical environment of the aorta, has been accomplished thanks to electrospinning. In this sense, this chapter has allowed us to navigate through this technique, understand how their parameters affect the production of fibers and optimize them to create the desired scaffold.

The first goal of the chapter was to define the general parameters of the technique considering the requirements of our scaffold. Focusing on the artery's anatomy, the desired microstructure should have homogeneous fibers, with a considerably low stiffness. Both layers were first manufactured separately to optimize the fiber morphology, diameter and mechanical properties of each layer. The design of the random layer started by using the flat collector and optimizing the operational parameters such as the distance from the tip to the collector or the flow rate. But even though the obtained stiffnesses were very low, the fibers produced were not homogeneous and presented significant bead formation. Further analyzing material's parameters such as viscosity and dielectric constant of the solvent was required to produce homogeneous fibers without beads. In this sense, three different combinations of solutions were tested: PCL mixed with Sq using only chloroform as a solvent, PCL using chloroform as a solvent, and last, PCL using a mixture of chloroform and DMF as a solvent. The last combination appeared to be the best choice to electrospin homogeneous fibers, with good distribution and mechanical properties. Eliminating Sq from the mixture resulted in a production of fibers less compact in the surface and with quite homogeneous fibers. Introducing DMF resulted in an increase of the boiling point of the mixture but helped raising the dielectric constant of the global solution. This resulted to be the key factor to eliminate the formation of beads at high feeding rates.

All the findings regarding material properties were used for the design and manufacturing of the aligned layer. But manufacturing aligned fibers having an angle that differs less than 80% was complicated with the existent equipment. We designed a new collector to produce the proper aligned fibers. This collector consisted in a double-bar collector manufactured with stainless-steal, a conductor material. The distance of choice between both bars that resulted in a more aligned and homogeneous fibers was the 2.0 cm collector. More research should be performed in this field to optimize the design and electrospinning process to produce larger samples. Overall, the design and manufacturing of the 2 layers scaffold with an aligned layer with fibers aligned more than 80% with a random homogeneous porous layer was achieved.

As stated at the beginning of this thesis, the final end of this project is to provide a new treatment for patients suffering AD. The last step of this chapter was focused on finding an industrial partner that could manufacture the scaffolds with the desired biomechanical properties. Two different industrial manufacturers were found: TECL and Bioinicia, which were able to manufacture scaffolds with an improved alignment and the desired mechanical properties.

The next step was testing all the manufactured samples in an *in vitro* environment. The samples of study for the next steps were:

- IQS samples: 18.0 cm distance and 1,000 rpm speed.
- TECL samples: 2, 3 and 4 µm diameter for the random layer fibers and 1 µm for the aligned layer fibers.
- Bioinicia samples: 4.84 µm diameter for the random layer fibers and 1.24 µm for the aligned layer fibers.

3 DEVICE EVALUATION AS A FAVORABLE ENVIRONMENT FOR ENDOTHELIAL CELL MIGRATION AND PROLIFERATION

3.1 Introduction

Healthy blood vessels have an elegant three-layer structure including the *tunicae intima*, *media*, and *adventitia*, which endows them with ideal mechanics, haemodynamic and anti-thrombus properties[102]. As stated in previous chapters, these layers are formed of different components, including EC, SMC, and a combination of different proteins and macromolecules that together constitute the ECM. The interaction between cells and the ECMs plays a critical role in cell anchorage and signal transduction[103]. Even though our patch's microstructure should promote cell migration by itself, the introduction of ECM proteins may be interesting to improve this process. Moreover, cells behave different in *in vitro* culture tests compared to their natural environment. The use of ECM proteins could enhance the cell interaction with the patch *in vitro.* Therefore, making even more interesting to test the proteins of the ECM.

The patch is designed to be colonized by the two existing cell types in the aorta (ECs and SMCs), but according to the vast literature, reendothelialization[104] should be the first process to take place, due to the vital functions of EC in the vessel wall[105,106]. This chapter is focused on studying those proteins and peptides that promote EC migration, starting with fibronectin and laminins.

3.1.1 Fibronectin

Fibronectin (Fn) is one the most studied proteins of the ECM[107]. It is a dimeric multidomain glycoprotein that not only is a crucial protein of the ECM but also an abundant component of plasma (300 µg/mL) and other fluids in the body[108]. Fn is produced and secreted by multiple cell types, including SMCs, fibroblasts, ECs and chondrocytes, among others[109], and is widely distributed across the ECM[15].

Fn provides an excellent substrate for cell adhesion and spreading. Thanks to that, it promotes cell migration in different stages of a human life, starting with the embryonic development, wound healing, in tumor progression and in angiogenesis[110,111]. Fn structure is important to understand why this protein mediates a wide variety of cellular interactions. It is composed of two nearly identical subunits covalently linked by a pair of disulfide bonds. Each monomer consists of three types (I, II and II) of repeating units. Sets of repeats constitute binding domains for fibrin, FN, collagen, cells and heparin (Figure 54).
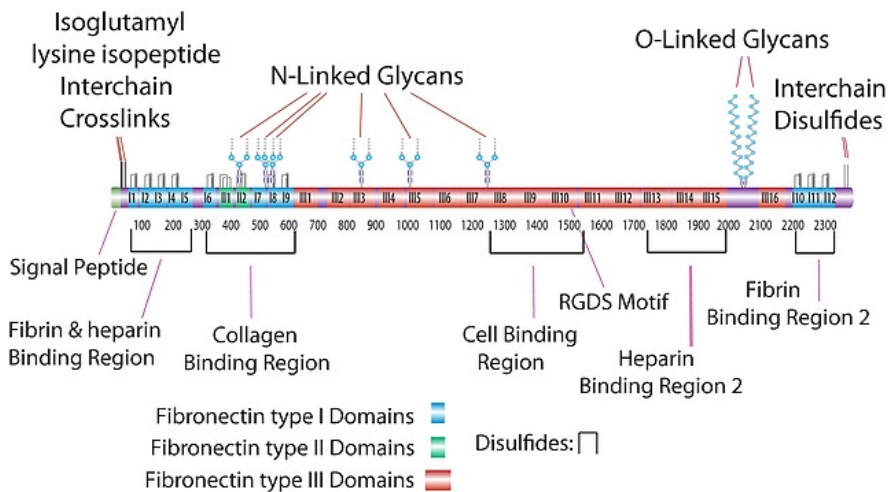
Figure 54. Fn structure[112]

It binds to cell surfaces through integrins but also to other extracellular matrix molecules such as heparin, collagen/gelatin, or fibrin. Fn is a ligand to dozens of molecules in the integrin receptor family. These are cell-surface heterodimeric receptors which link Fn with the intracellular cytoskeleton, conferring structural functions to the cell. Some of its biological activity includes mediation of cell adhesion, proliferation, and differentiation, as well as embryogenesis and wound healing.

3.1.2   Laminins

Laminins are a large family of cross-like heterotrimeric glycoproteins. These proteins can be found in almost all tissues of the body[113] since they are structural components of basement membranes[114], and in the ECM[15]. Laminins are involved in a variety of biological processes such as tissue survival, angiogenesis, or wound healing, among others. They also contribute to regulating cellular activities such as cell adhesion, migration, differentiation, and proliferation.

Laminins are composed of α-, β- and γ- subunits that are assembled into two different forms: cross-shaped or Y-shaped molecules. Currently, five α-, four β- and three γ-subunits of genes have been identified in the human genome. Therefore, each laminin is named with 3 numbers regarding its trimeric composition. Vascular endothelial cells express laminin α4 and α5 chains that combine with laminin β1 and γ1 chains to form laminins 411 and 511, respectively (Figure 55[115]). Laminin α chain distribution and expression depend on endothelial cell type, state of vessel growth and activation state[116]. Vascular SMC of large vessels like the aorta have been reported to express laminin α2, the major laminin α chain of myogenic tissues (those tissues that react to increase or decrease blood pressure to keep the blood flow within the blood vessel constant).
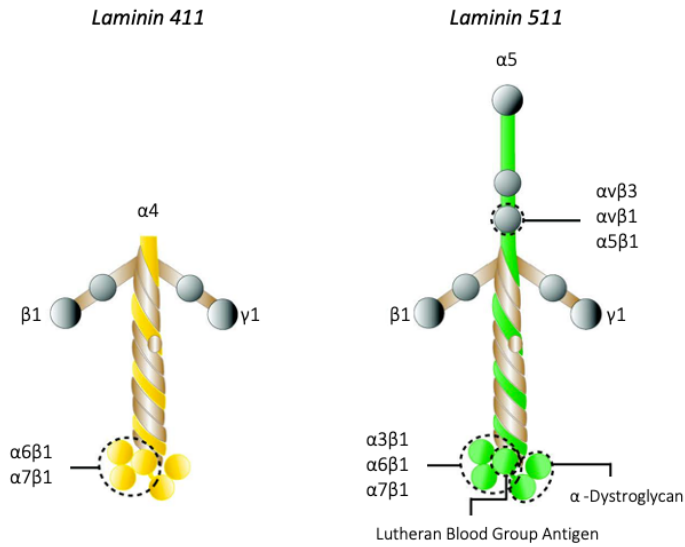
Figure 55. Endothelial Laminins structure

ECM proteins could be a great approach for creating a suitable environment for cell adhesion and proliferation. At the same time, it could be interesting to use only small parts of these proteins, their peptides, with simpler manufacturing and regulatory routes. It has been reported that the use of some derivative peptides from ECM proteins could enhance[113] the colonization process[117,118]. Some peptides that could play this role are described below.

3.1.3   Peptides from the ECM

1. RGD

   The arginine-glycine-aspartic acid (RGD) cell adhesion sequence was discovered in Fn in 1984[119].Later, this sequence was found in other cell adhesive ECM proteins and, therefore, described as a common cells recognition motif[120]. Proteins that contain the RGD attachment site constitute a major recognition system for cell adhesion. Integrins, which are a superfamily of cell adhesion receptors that recognize mainly ECM ligands and cell-surface ligands[121], serve as receptors for them. But it is difficult to achieve high binding selectivity due to the similarity of the RGD binding regions in most integrins.

2. YIGSR

   The pentapeptide tyrosine-isoleucine-glycine-serine-arginine (YIGSR) is present in the β-chain of laminins[116,122] and binds the laminin receptor. YIGSR facilitates cellular attachment.

3. VGVAPG

   Elastic fibers provide elasticity to many connective tissues such as the major arteries, lung, cartilage, elastic ligaments and skin[123]. The major component of these fibers is elastin which provides elasticity and resilience to tissues that require the ability to deform repetitively and reversibly[124]. One of the elastin-derived peptides is the hexapeptide valine-glycine-valine-alanine-proline-glycine (VGVAPG).

3.1.4 Surface modification

All these proteins and peptides of the ECM can facilitate and enhance the adhesion and migration of ECs towards the patch. But even though PCL has excellent biocompatibility and acceptable degradation kinetics, it has low surface wettability of the natural ECM[125]. Therefore, the interaction between the patch and the ECM proteins and peptides could be complicated. This interaction could be enhanced by modifying the surface of the patch since surfaces play an important role in biological systems. Most biological interactions occur at the surfaces and interfaces[103]. Surface treatment techniques, such as plasma treatment, ion sputtering, oxidation and corona discharge, affect the chemical and physical properties of the superficial layer without significantly changing the bulk material properties[126], such as the required mechanical properties and biodegradability. One of the easiest surface treatment techniques is the corona discharge (CD), which has already been used in a previous pilot project[77] which set the grounds of this thesis.

CD is a moderately low-power electric discharge that occur at or near atmospheric pressure[127,128]. The corona is invariable produced by strong electric fields associated with small diameter wires, needles on sharp edges on an electrode[127]. The stream of charged particles such as electrons and ions are inhomogeneous and requires a narrow space between the electrodes[129]. CD has been widely applied to treat the surface of polymers. It can tailor the physical and chemical properties of the surface of materials resulting in enhanced hydrophilicity of the material by incorporating a variety of polar functional groups, such as oxygen- and nitrogen-containing groups. This can act as anchors for a wide range of biological molecules and so it can be useful for our purpose.

3.2 Objectives of the chapter

The main objective of this chapter is to demonstrate *in vitro* that the patch developed provides a suitable milieu for cell migration and proliferation. In this sense, different considerations were taken. After scaffolds are implanted in the body, it is unlikely for cells to contact the surface of the scaffold instantly. The anchorage of cells to a foreign surface depends on specific proteins and extracellular instructions. The correctly presented proteins could stimulate a constructive cell response, favoring wound repair and tissue regeneration. Thus, choosing the right proteins or peptides could be critical to enhance cell response. The other consideration to be made would be to consider the intrinsic low wettability of PCL, which may lead to a low interaction with the ECM proteins and cells. Modifying the surface of the patch would be a key factor to accomplish the main objective of the chapter.

To do so, three specific goals have been established:

1. Evaluate cell adhesion kinetics onto the patch by quantifying attachment, interaction, and proliferation of human aortic endothelial cells (HAoEC) on the patches manufactured.
2. Create a cell migration model to demonstrate that cells climb on the patches and are not seeded directly on the surface of the patches.
3. Test the cell migration model towards the patch. This last part of the chapter should be used to decide which patch is the best candidate to be tested in an animal model.

3.3 Results

3.3.1 Cell adhesion onto the patch

Demonstrating that the microstructure designed provides a suitable environment for cell migration and proliferation starts by testing the simple interaction of HAoECs in contact with the patch's microstructure. Aortic endothelial cells should be deposited on top of the patch to demonstrate that the patch designed offers high biocompatibility degree. To do so, a set of experiments were performed in which the patches are attached on a cell culture plastic well using a commercial adhesive and then cells are seeded all over the patch and the cell culture well (Figure 56).
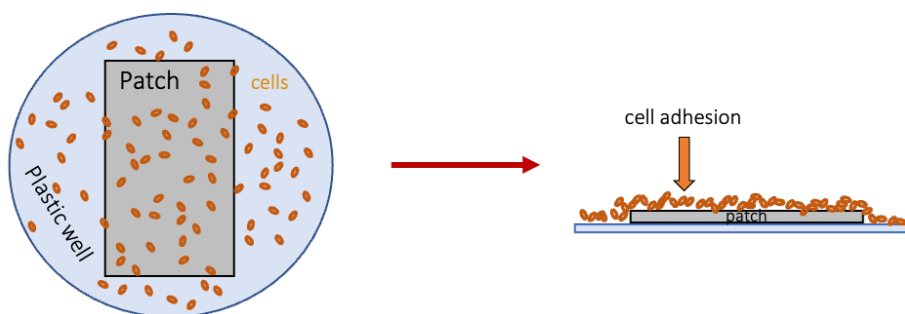
Figure 56. Cell adhesion experiments design.

Besides testing the interaction of the ECs with the patch, this interaction was also compared against different ECM protein coatings. Therefore, it was decided to study the interaction of the patch manufactured in IQS with Fn, two different laminins (Laminin411 and Laminin511) and VE-Cadherin compared to the control which was phosphate buffer saline (PBS).

The standard protocol when coating a surface with a protein, for example with Fn, is to distribute the protein over the surface of interest and let the protein deposit for 2 hours at 37 ºC. CD offers the possibility of generating a covalent bond between the protein and the surface treated. To study the effect of the CD treatment, the deposition time was reduced from 2 hours to 5 minutes and the process was performed at room temperature (Figure 57 and Figure 58).
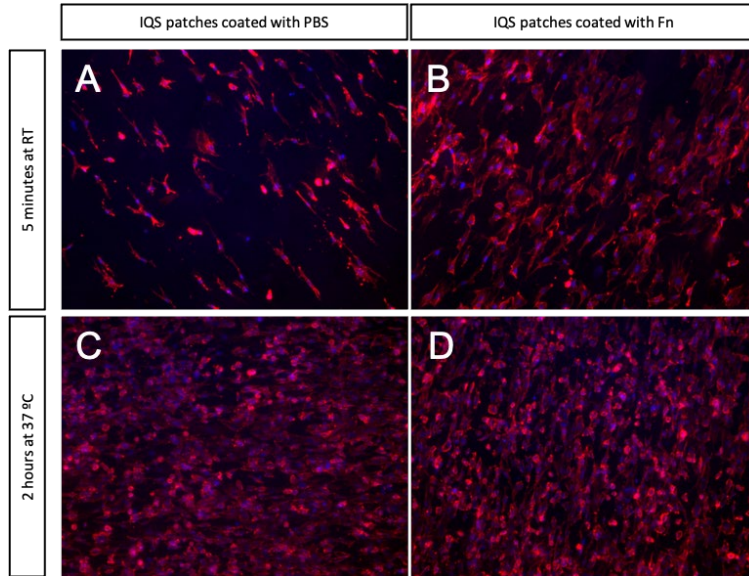
Figure 57. Comparison of cell adhesion to patches manufactured at IQS using different coating conditions. Cells were cultured for 48 h before performing the cytochemistry assay. Cell cytoskeleton marked in red using phalloidin staining and cell nuclei in blue using DAPI staining. The level of adhesion as well as the cell morphology was better when coating the patches for 2 hours at 37 ºC.

Figure 58. Comparison of cell adhesion to patches manufactured at IQS using different coating conditions. Cells were cultured for 48 h before performing the cytochemistry assay. Cell cytoskeleton marked in red using phalloidin staining and cell nuclei in blue using DAPI staining. The level of adhesion as well as the cell morphology was better when coating the patches for 2 hours at 37 ºC.

Cytochemistry results are presented in two separated figures (Figure 57 and Figure 58) to provide a clearer view of the cells' morphology. In all cases, the number of cells adhered to the surface of the patch after 48 h of cell culture was qualitatively greater when having the coating deposited for 2 h at 37 ºC. Cell morphology was also better when the protein was deposited for a longer period. Surprisingly, there was a wide number of cells, and their morphology was in accordance with healthy ECs when using PBS only as coating. This was a very promising result since it could indicate that the microstructure itself works as a guide for cells to migrate and grow. These results should be further confirmed with other tests. Last, VE-cadherin resulted to be the worst environment for cells to adhere and grow. In fact, this was an expected result since role of this protein is to promote the migration of SMC but inhibit the EC's. The number of cells attached in each sample was quantified to confirm the visual analysis (Figure 59). The results confirmed that in all cases, except in VE-Cadherin coating, the number of cells attached to the patch was greater when having the prolonged coating. Moreover, they also confirmed that the number of cells present in the gold standard used (Fn) offered really similar results compared to the "control" with PBS.
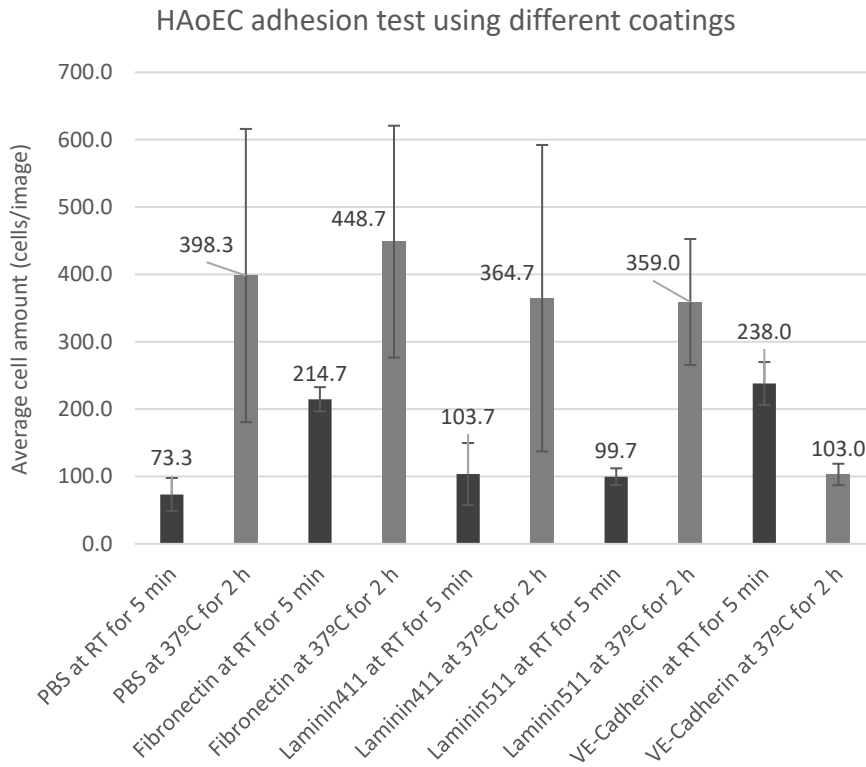
Figure 59. Average cell amount using different protein coatings and conditions.

These results evidenced that activating the surface of the patch with CD was not as effective as depositing the coating of choice for 2 h at 37 ºC. By this means, another surface treatment could have addressed this problem, but it was discarded because the results with the deposited coating were good enough for our purpose. The same experiment was repeated with the patches manufactured by the two companies, TECL and Bioinicia, to test their microstructures and compare the results with the patches designed at IQS. The same conditions and coatings were tested for this set of experiments but only for a 2-hour incubation (Figure 60 and Figure 61).
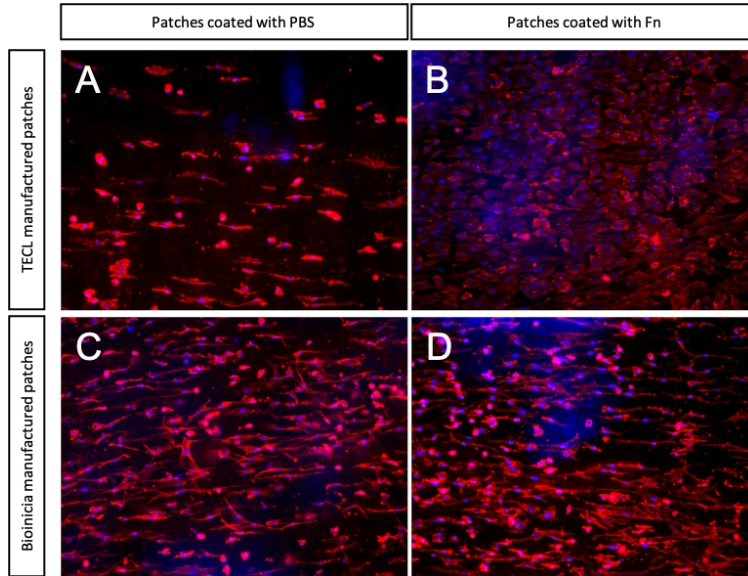
Figure 60. Comparison of cell adhesion to patches manufactured at TECL (A and B images) and Bioinicia (C and D images) using different coating conditions. Cells were cultured for 48 h before performing the cytochemistry assay. Cell cytoskeleton marked in red using phalloidin staining and cell nuclei in blue using DAPI staining. Cell morphology in TECL patches coated with Fn was in accordance with healthy EC, having the orthogonal shape. The level of cell adhesion and morphology in Bioinicia patches was similar in both conditions.
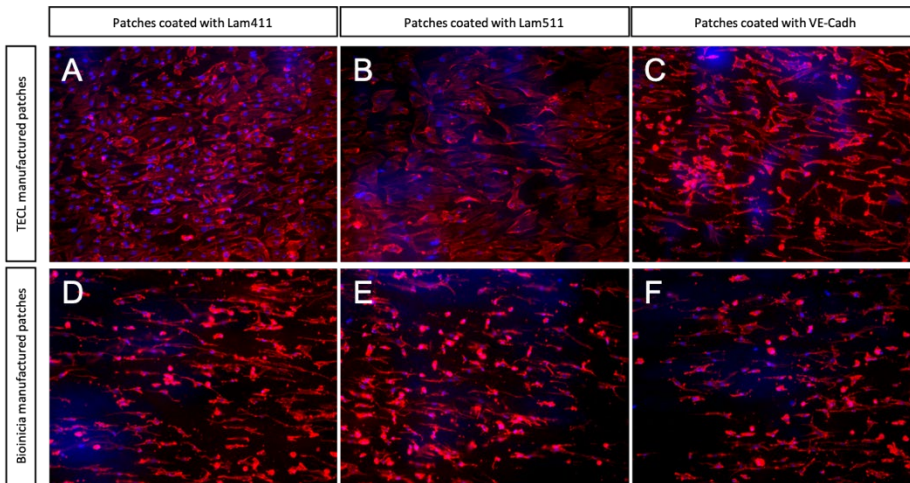
Figure 61. Comparison of cell adhesion to patches manufactured at TECL (A, B and C images) and Bioinicia (D, E and F images) using different coating conditions. Cells were cultured for 48 h before performing the cytochemistry assay. Cell cytoskeleton marked in red using phalloidin staining and cell nuclei in blue using DAPI staining. The level of adhesion as well as the cell morphology was better in all TECL patches conditions than in Bioinicia patches.
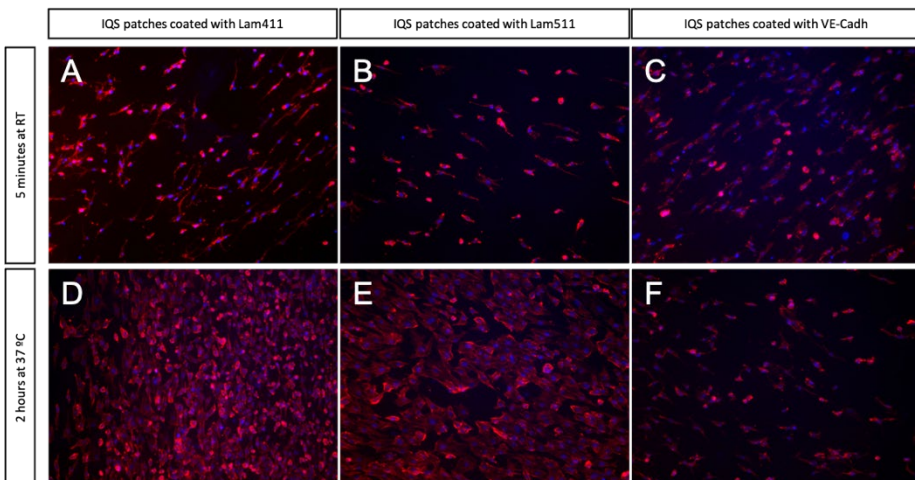
In all cases, the number of cells adhered to the surface of the patch after 48 h was qualitatively greater in the patches manufactured at TECL than at Bioinicia. Cell morphology in most conditions in TECL patches was in accordance with healthy EC which normally have hexagonal shapes (Figure 62). Unexpectedly, the number of cells attached and their morphology in the TECL patches coated only with PBS was considerably inferior but, as seen in further results, this was an artifact in the experiment. Finally, even though the number of cells present in the TECL patches coated with VE-Cadherin was qualitatively greater than with the IQS patches, the bad cell morphology indicated that the apoptosis process had begun. In the case of Bioinicia patches, the cell amount was apparently similar to the TECL patches while the morphology was worst in most cases. In the Bioinicia patches, cells tended to be more elongated and less hexagonal. The cell morphology should be in accordance with the microstructure and, this stretching process would be due to the alignment of the cells with the aligned fibers. But, since the membrane of cells was excessively elongated it was considered that cells were more likely to be in an apoptosis process.
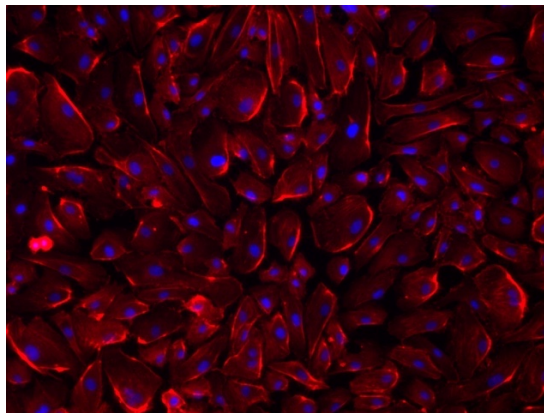
Figure 62. Morphology of healthy endothelial cells in a cell culture well. Cell cytoskeleton marked in red using phalloidin staining and cell nuclei in blue using DAPI staining.

The number of cells attached in each sample was quantified to confirm the visual analysis (Figure 63), which confirmed the qualitative results in all cases. TECL patches showed greater number of cells in all cases except for the PBS sample, which resulted in very low number of cells. In general, the best results in TECL patches were obtained with Fn and Lam411, while in Bioinicia patches, PBS exhibited the best results, and all the other conditions presented no significant differences. Moreover, in all cases the number of cells was less than with the IQS patches.
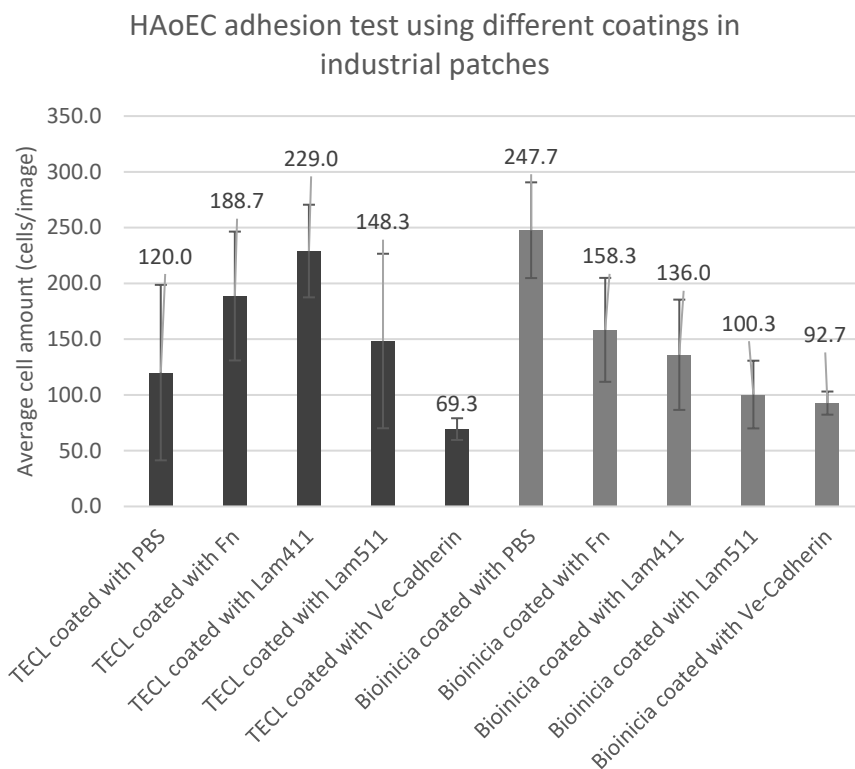
Figure 63. Average cell amount using different protein coatings in industrial patches.

These results indicate that even though some patches and coating conditions provide a better environment for cell growth, all patches presented a good environment for cells to grow on. The best conditions were both Laminins, Fn and PBS. It was decided to only continue testing the Lam511 for logistical reasons.

3.3.2 Creation of a cell migration model

The main objective of the patch is to cover the AD tear and to provide a suitable environment for cells to grow and regenerate, to, at some point, completely colonize the patch. But, at the beginning of the re-endothelization process, no cells will be present on the patch's surface. In fact, it would be interesting to replicate the re-endothelization process in an *in vitro* model. This model would allow to demonstrate *in vitro* that ECs are able to climb from the cell culture plate to the top of the patch. This migration process would take days or even weeks and the patch's microstructure should enhance this process.

The first stage of this chapter, section 3.3.1, consisted in testing the cell behavior when cells are seeded directly on the surface of the patch. On the contrary, to evaluate the capability of cells to migrate towards the patch, no cells would be seeded on the surface of the patch in these set of experiments. A hydrophobic surface was designed and manufactured to prevent cells from depositing to the patch's surface while seeding them. This surface consisted of a silicone plug of the same shape and size of the patch. The plug was an easy, fast and cost-effective way to prevent the cells to deposit onto the patch while seeding them, and it would be easy to remove after the first deposition hours.

The development of the migration assays would take place the same way as in the adhesion tests but, before seeding the ECs, the patch would be covered with the silicone plug. The silicone plug would be removed after 12 h and the migration of the cells was evaluated at different timepoints (Figure 64).
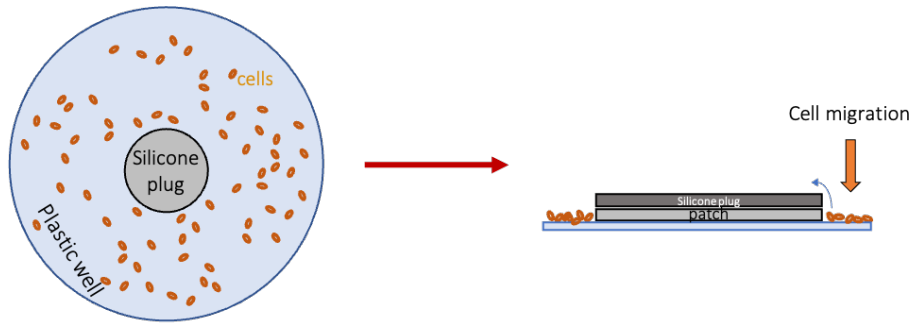
Figure 64. Cell migration model in the presence of the patch.

Prior to perform the migration assays and to have an estimation of the time that cells would take to migrate through the patch, we designed an experiment in which cells were seeded on a plain cell culture well containing only a silicone plug (Figure 65).
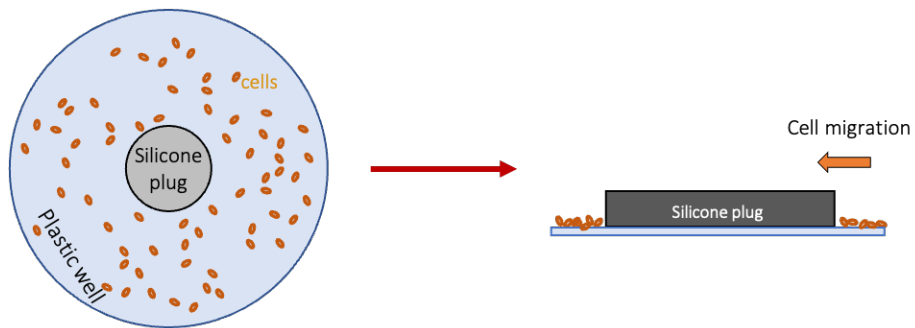
Figure 65. Cell migration model without patch.

Cells were seeded all over the well except for the surface covered by the silicone plug. The plug was removed 12 h after seeding, leaving an unseeded zone in the center of the well, called the "plug area". Live images were taken at different timepoints to observe the progression of cells colonizing the plug area (Figure 66).

A Days after plug removal

6 days | 10 days

17 days | 21 days
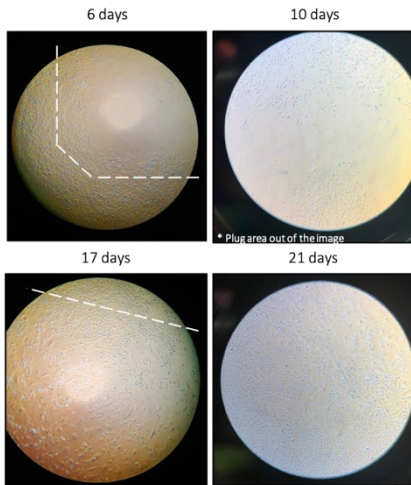
B Colonization pattern can be represented with an S-curve graph
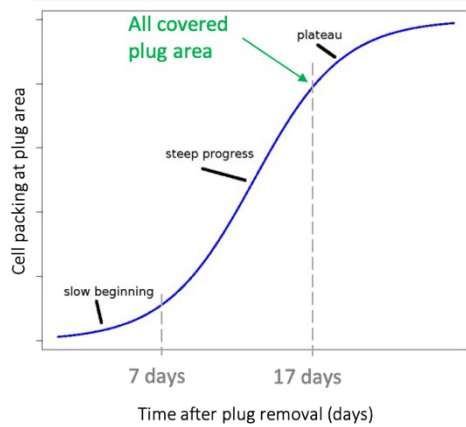
Figure 66. A) image corresponds to the cell migration in vivo images after plug removal. The dashed lines indicate the borders of the plug area. In some cases, the plug area was difficult to identify. After 17 days the plug area was completely covered. On B) image there is the correlation between the area covered by EC and the cell progression.

From this experiment, we concluded that 17 days were needed to completely cover the plug area. At the beginning, the colonization process is slow, then cells gradually grow until reaching the plateau stage by the day 17th. But those are the ideal conditions. Colonizing the cell culture well would be easier and faster than would be to colonize the patch, but still this experiment was very useful to know the pattern of cell migration and progression.

3.3.3   Cell migration towards the patch

The last stage of this chapter was to combine the results of the previous sections to study the EC migration and proliferation onto the different manufactured patches. The first patches tested were the IQS patches using the best conditions that resulted from the adhesion tests (PBS and Laminin511) and a new condition using only CD right before the seeding process. Moreover, as discussed before, not only ECM proteins could enhance the cell migration but also the small peptides that constitute these proteins. The peptides tested at this point were: the widely studied RGD, the peptide present in the β-chain of laminins, YIGSR; and the elastin-derived peptide, VGVAPG.
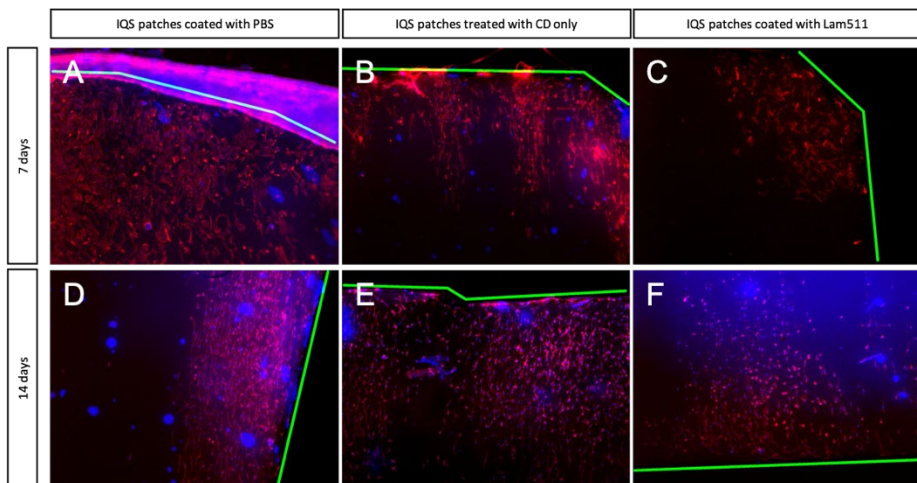
Figure 67. Comparison of cell migration for 7 and 14 days onto patches manufactured at IQS using different coating conditions. Cell cytoskeleton marked in red using phalloidin staining and cell nuclei in blue using DAPI staining. The boundaries of the patch are marked with a green line. All images were taken at 4x magnification. Cells migrated in all cases and their morphology was aligned with the patch's fibers.

Treating the samples only with CD and without depositing any other component (protein, peptide, or PBS) resulted in the best migration results. All samples were treated with CD before being coated with the corresponding component. At both endpoints, CD presented the best migration results. At 7 days, all other conditions presented low colonization rate, lower than with PBS. Notice that images in Figure 67 and Figure 68 represented the best migration results from this experiment. At 14 days, laminin511 and YIGSR provided good results compared to CD only, and apparently the number of cells was higher than PBS. In all cases, cells migrated through the aligned fibers (the ones that were facing up during the experiment) adapting their morphology to the fiber morphology. This tendency was already observed in previous tests but cell alignment here was greater. This alignment was more remarkable in these experiments because cells were migrating towards the patch through the fibers, and their cytoskeleton was in accordance with that. This matter could be interesting since the alignment would contribute to achieve the cell migration and complete re-endothelization with less time.
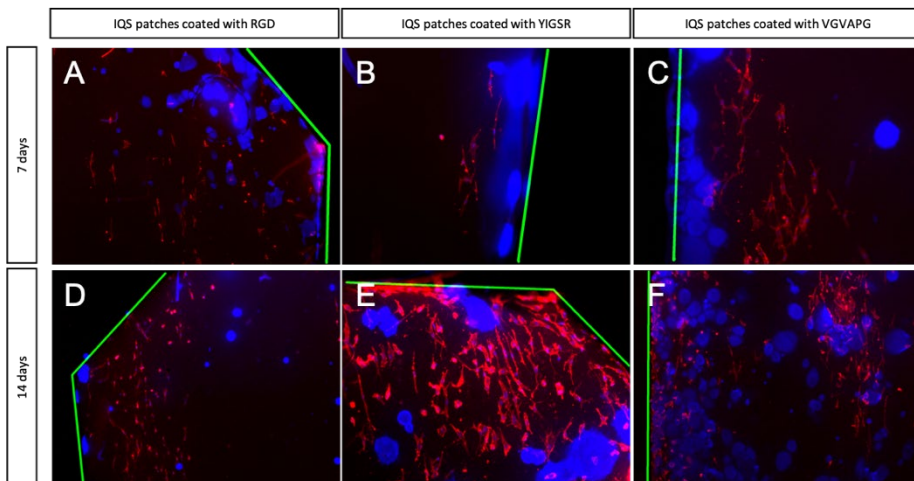
Figure 68. Comparison of cell migration for 7 and 14 days onto patches manufactured at IQS using different coating peptides. Cell cytoskeleton marked in red using phalloidin staining and cell nuclei in blue using DAPI staining. The boundaries of the patch are marked with a green line. All images were taken at 4x magnification. Cells migrated in all cases and their morphology was aligned with the patch's fibers.

After performing these experiments, it was noted that the corners of the patch got detached from the well bottom along with the time. This could result in lower colonization rates since cells were unable to reach the edge of the patch and start the colonization. Other adhesives were tested to improve the adhesion of the patch in a wet surface but none of them resulted in a better adhesion. The adhesive used was not part of this study, therefore, the limitations derived from it were considered when analyzing the results, but no improvement was done.

The next step was to repeat the migration assays with the outsourced patches. The only conditions tested for these patches were the CD treatment and the use of PBS after CD treatment. The main reason behind this choice was the difficulties experienced to maintain the patch attached to the well and the low migration rates obtained in all the peptide-coatings. Moreover, this was a way of reducing the number of experiments to simplify the operational process.
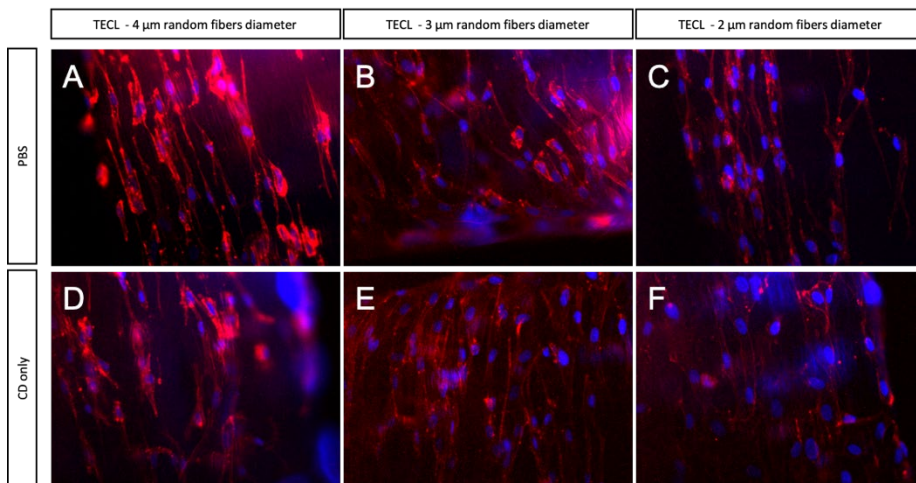
Figure 69. Comparison of cell migration for 7 days onto patches manufactured at TECL having different random fiber diameter. Only two conditions were tested: PBS and CD only. Cell cytoskeleton marked in red using phalloidin staining and cell nuclei in blue using DAPI staining. All images were taken at 20x magnification. Cells migrated in all cases and their morphology was aligned with the patch's fibers. A great number of cells was founded in all cases. The results shown were the best migration existent images.

Three different TECL patches were tested (Figure 69). All of them had the same aligned fiber layer but different fiber diameter for the random layer (2, 3 and 4 µm diameter). In all cases, patches demonstrated really good results in terms of number of cells able to start colonizing the patch. When comparing the three samples, 3 µm diameter for the random layer exhibited the best results in terms of number of migrated cells. Even though cells were migrating through the aligned layer, the mechanical properties and cohesion of the fibers in the different random diameters were different and affected the general migration of the ECs. Comparing these results with the IQS manufactured patches, it could be observed that the cell aspect on all TELC patches was more elongated, and the cytoskeleton was thinner than on IQS patches with only CD treatment. This could be caused by the greater alignment of the fibers in the TECL patches since aligned fibers in both samples (TECL and IQS) were similar in diameter, around 1 µm for the TECL fibers and 1.6 µm for the IQS aligned fibers.
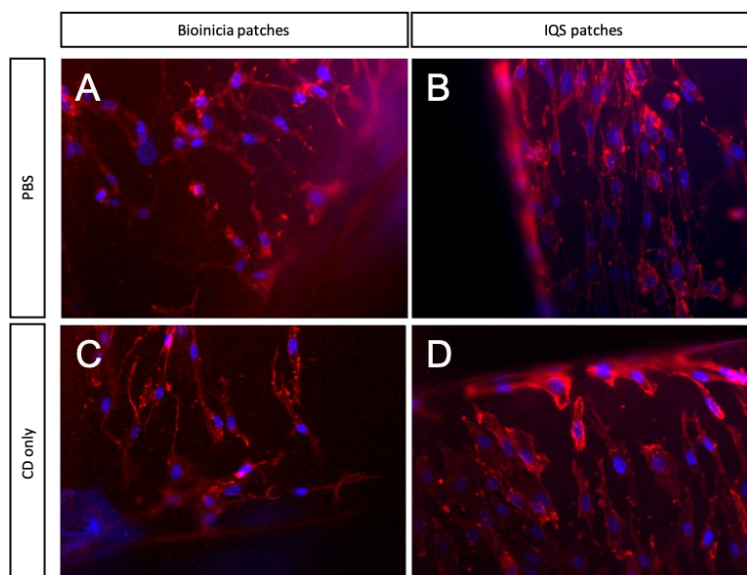
Figure 70. Comparison of cell migration for 7 days onto patches manufactured at Bioinicia and IQS (control). Only two conditions were tested: PBS and CD only. Cell cytoskeleton marked in red using phalloidin staining and cell nuclei in blue using DAPI staining. All images were taken at 20x magnification. Cells migrated in all cases, but the number of cells was qualitatively lesser in the Bioinicia patches. The results shown were the best migration existent images.

Less cells colonized the patch in Bioinicia patches. Their cytoskeleton tended to be stretched but not aligned with the microstructure. This could be observed when comparing cell morphology of images C and D in Figure 70. In image C, cells were stretched but spread in all directions. In image D, cells were more hexagonal in shape, but spread in an aligned pattern. It was a strange finding since Bioinicia fibers were more aligned than IQS fibers and more similar to TECL aligned fibers besides their migration results were different.

All tests performed until this point considered EC migration towards the targeted layer, the aligned layer. It was also interesting to study the interaction of EC when the migration was produced through the random layer. These experiments would determine if EC preferred migrating towards a microstructure or the other. Therefore, the tests were replicated but this time having the random layer facing up while studying the migration towards the random layer (Figure 71, Figure 72 and Figure 73).
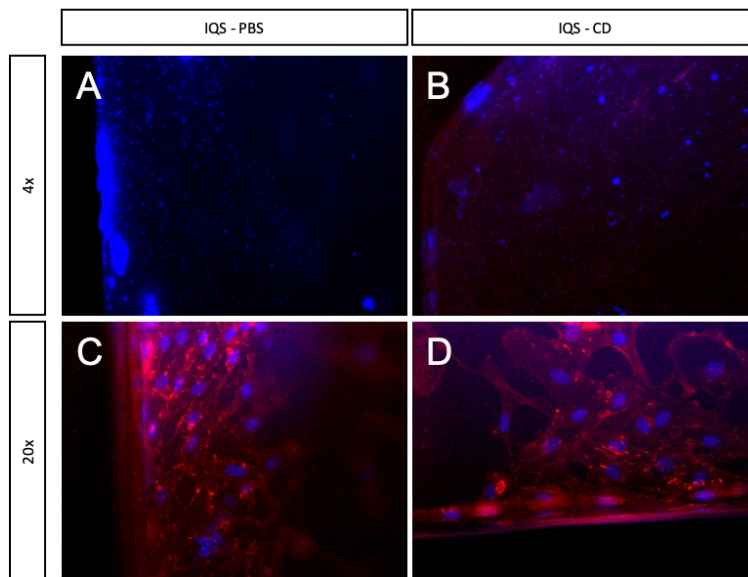
Figure 71. Comparison of cell migration for 7 days onto patches manufactured at IQS. Only two conditions were tested: PBS and CD only. Cell cytoskeleton marked in red using phalloidin staining and cell nuclei in blue using DAPI staining. The images were taken at 4x and 20x magnification. Cells migrated in all cases, but the number of cells present was lesser than when fibers are aligned. The results shown were the best migration existent images.
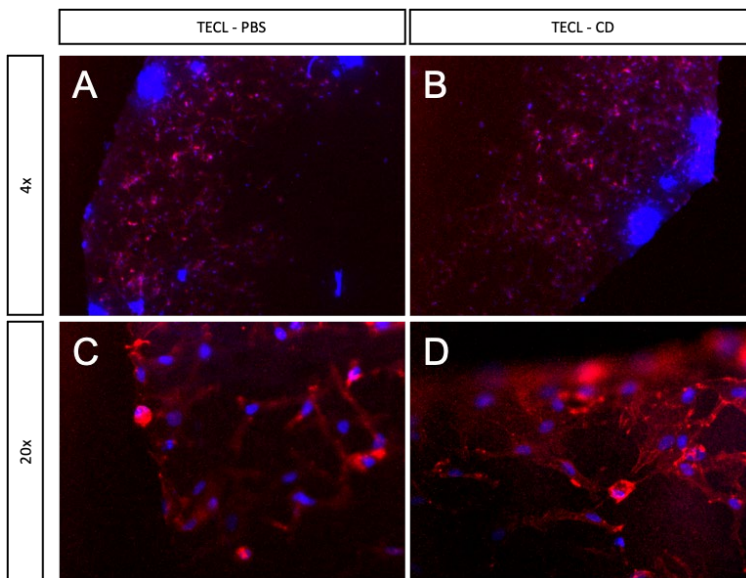
Figure 72. Comparison of cell migration for 7 days onto patches manufactured at TECL. Only two conditions were tested: PBS and CD only. Cell cytoskeleton marked in red using phalloidin staining and cell nuclei in blue using DAPI staining. The images were taken at 4x and 20x magnification. Cells migrated in all cases, but the number of cells present was lesser than when fibers are aligned. The results shown are the best migration existent images.
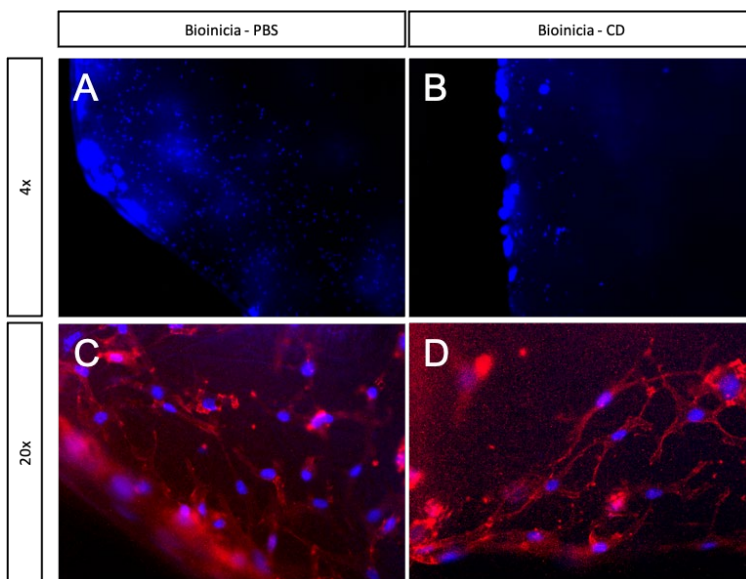
Figure 73. Comparison of cell migration for 7 days onto patches manufactured at Bioinicia. Only two conditions were tested: PBS and CD only. Cell cytoskeleton marked in red using phalloidin staining and cell nuclei in blue using DAPI staining. The images were taken at 4x and 20x magnification. Cells migrated in all cases, but the number of cells present was lesser than when fibers are aligned. The results shown are the best migration existent images.

Endothelial cells migrated in all cases, but the number of cells present was qualitatively less than when fibers are aligned. The highest colonization rate was with the patches manufactured at TELC, having 4 μm of random fiber diameter, when only using CD treatment. Patches manufactured at IQS exhibited a similar cell number when only treated with CD. Although cells migrated through the different patches in variable ratios, in all of them it was evidenced that cells were different in morphology. In these tests, cells tended to spread in all 2D directions, still having a stretched cytoskeleton due to the migration and proliferation processes. These tests demonstrated that the aligned microstructure resulted in a higher migration rate guided by the fibers. This process would be enhanced in an *in vivo* process thanks to blood flow.

At this point, cell migration was demonstrated in all kinds of manufactured patches, at different time rates and testing different coating conditions. Both patches, the one designed in this thesis, IQS patches, and the manufactured by TECL, exhibited similar behavior in terms of cell density and morphology. On the contrary, Bioinicia patches presented lower colonization rates in all conditions.

The last step of this section was to test the different cutting techniques and evaluating the migration rates that arise from them. Back in section 2.3.3, two different cutting techniques were studied: the classical die cut and the laser cut. In this set of experiments, the IQS manufactured patches were not tested since it was not possible to cut them using a laser.
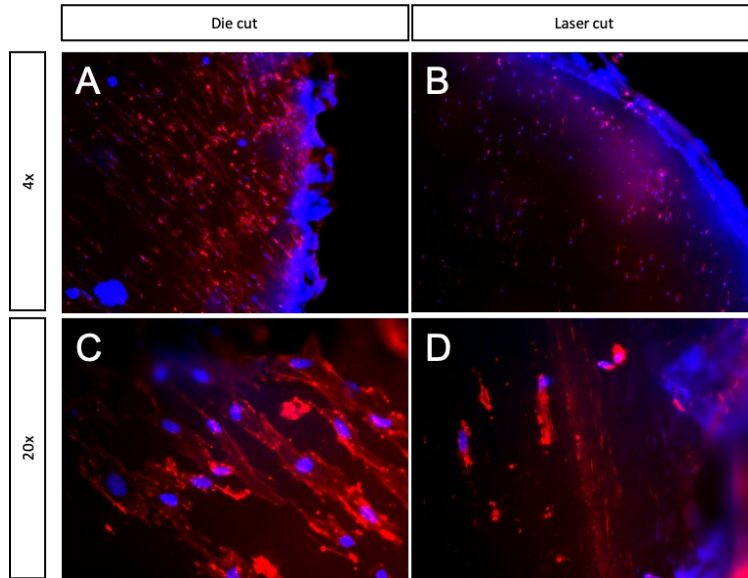
Figure 74. Comparison of cell migration for 7 days onto patches manufactured at TECL. CD only was the condition tested to rapidly compare two different cutting techniques. Cell cytoskeleton marked in red using phalloidin staining and cell nuclei in blue using DAPI staining. The images were taken at 4x and 20x magnification. Cells migrated in both cases, but die cut resulted to have the greater number of migrated cells.

The die cutting technique exhibited better results in terms of cell migration compared to the laser cut. This difference is evident when comparing images A and B in Figure 74 where there is a greater number of cells in image A than in B. The cell morphology in the die cutting patches was in accordance with the previous tests, stretched and enlarged but still polyhedric.
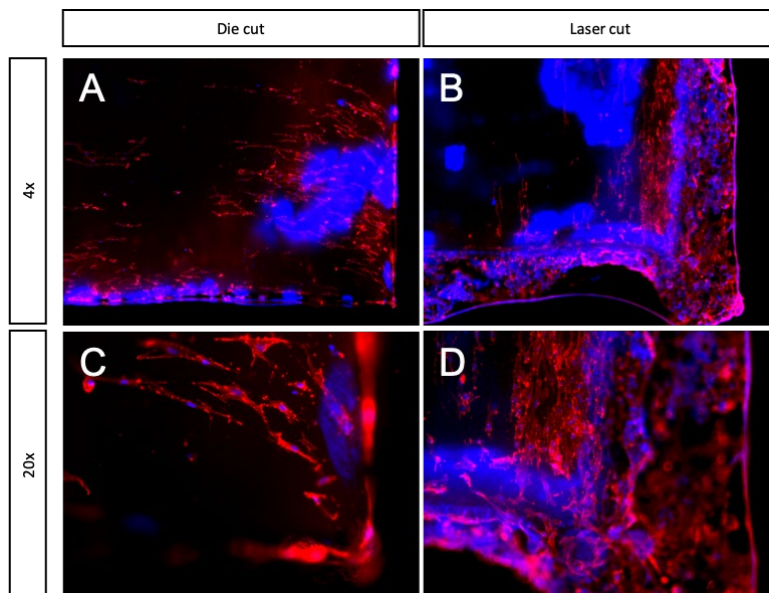
Figure 75. Comparison of cell migration for 7 days onto patches manufactured at Bioinicia. CD only was the condition tested to rapidly compare two different cutting techniques. Cell cytoskeleton marked in red using phalloidin staining and cell nuclei in blue using DAPI staining. The images were taken at 4x and 20x magnification, excluding image D that was taken at 10x. Cells migrated in both cases, but die cut resulted to have the greater number of migrated cells. The migration rates were lesser compared to the TECL manufactured patches.

Cell migration between both conditions was not that evident in Bioinicia patches, and the results in migration rates were similar. In these tests, cell cytoskeleton was stretched and enlarged with the alignment of the fibers (Figure 75). Overall, the migration rate was lower, and cell morphology was worse when compared to IQS and TECL patches. At this point, we decided that Bioinicia patches did not fall into the specifications, the results obtained in the migration assays were decisive to discard this manufacturing company.

After discarding Bioinicia patches, a last experiment was performed. In all past experiments, patches were rinsed after they were attached to the cell culture plate. This aimed at avoiding biocompatibility problems involving the adhesive. After rinsing, patches were treated with CD and, in some cases, a protein or just PBS were added to enhance cell interaction with the patch. In this last experiment, it was decided to avoid any treatment to the patch before seeding the cells, even avoiding the rinsing process (Figure 76).
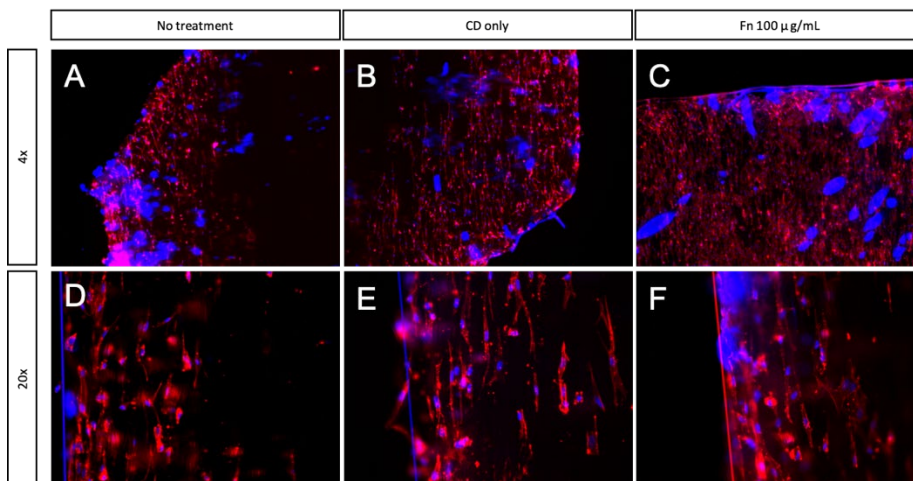
Figure 76. Comparison of cell migration for 7 days onto patches manufactured at TECL. Three different treatments were evaluated: no treatment (no rinsing, no CD, no PBS; it's been the whole time in a dry RT environment), CD only and the gold standard, Fn at 100 μg/mL. Cell cytoskeleton marked in red using phalloidin staining and cell nuclei in blue using DAPI staining. The images were taken at 4x and 20x magnification. Cells migrated in all cases, but CD and the gold standard resulted to have the greater number of migrated cells.

The results were really encouraging since cells were able to start the colonization process even when no treatment was applied to the patch. This way it was demonstrated that the microstructure designed provides a great environment for ECs to grow and colonize the patch. The patches manufactured in the field of this thesis exhibit comparable results, when comparing with the TECL manufactured patches, and even better than patches manufactured by Bioinicia. TECL manufactured patches would be used for the last section of this thesis.

3.4   Concluding remarks

It has been possible to accomplish the main objective of the chapter by demonstrating that the patch designed was a suitable milieu for cell migration and proliferation. To facilitate this process, biocompatibility and cell interaction with the different patches was only tested in contact with EC.

The easiest way to demonstrate the cell interaction with the patch's microstructure was through adhesion tests involving the use or not of different protein coatings and surface treatments. In this sense, the first patches tested were the patches manufactured at IQS. It was demonstrated that coating after CD treatment resulted in a greater cell adhesion when incubated for 2 hours at 37 ºC. PBS and the gold standard, Fn, exhibited the greater number of cells attached to the patches and with the morphology more in accordance with ECs. Both laminins tested, Lam411 and Lam511 exhibited good and similar results in terms of cell adhesion ratio and morphology. VE-Cadherin, as expected, exhibited the lowest adhesion rate. Overall, cell interaction with the patches proved excellent and the best conditions were the incubation of the coating after the CD treatment for 2 hours. The cell adhesion was also tested in patches manufactured by TECL and Bioinicia. Cells in TECL patches exhibited a more aligned cytoskeleton due to the alignment of their fibers, with good cell adhesion ratio and morphologies. In the case of the Bioinicia patches, they exhibited lower colonization rates and cells presented the most stretched morphology.

In a second phase of the chapter, a migration model was designed and evaluated. It was proven that cells needed 17 days to completely colonize the surface of the patch in an ideal test. This period would be a good guidance to develop the migration tests *in vitro* and in future *in vivo* tests.

Migration tests at 7 and 14 days were performed in accordance with the model designed. In all cases, cell migration towards the patches was achieved. The use of protein-derived peptides was introduced as a new condition in these tests, but none exhibited better results than the already tested, PBS or Fn. In this sense, it was decided to avoid the use of proteins or peptides in this phase of the project. EC migration was more effective through the aligned layer which reinforces the accomplishment of one the main objectives of this thesis, to have a microstructure that acts as a guidance for cells to migrate. In this sense, the patches manufactured at IQS exhibited similar migration ratios compared to the patches manufactured by a contract manufacturing organization, TECL. The best conditions were the use of PBS as a coating or even with only treating the surface with CD. Last, the classical die cutting resulted in an easy surface for cells to climb while laser cut resulted in a boundary.

After the migration tests, the Bioinicia patches were discarded for further research since the migration ratios were lower than in the other cases and the cell morphology was the worst. On the contrary, patches manufactured by TECL have been used in the following steps of this thesis.

4 *IN VIVO* IMPLEMENTATION

4.1 Introduction

As stated eariler, *in vitro* systems enable high throughput testing but fail to reflect the complexity of the organism[130]. This happens because the behavior of the vascular wall, both mechanically and biologically, is very characteristic and can only be truly investigated *in vivo.* When compared to clinical studies, *in vivo* animal studies can provide full access to tissues, cells, and highly invasive measurements. *In vivo* animal models are, therefore, absolutely required to assess the biological implications of having the patch attached to the artery for days and months.

4.1.1 Animal model

For the success and validity of the patch developed in this thesis, it was crucial to identify the most appropriate animal model. Selecting the best model "reduces and refines" and improves research[131]. Rodent models, such as rats, mice, and hamster, are the most widely used animal model for research. These models are cheap, easy to handle and to house in large numbers and, therefore, more suitable for high-throughput studies. But rodent models do not mimic the complex hemodynamics found in a human aorta. Moreover, the size of these animals makes impossible to handle the patch's implantation. Even though the size of the patch itself can be readjusted; the device used to implant the patch cannot. Larger animals are hence required.

Large animals are expensive and require substantial resources for housing and care. Furthermore, investigations in larger animals are more limited due to ethical considerations[132]. Nevertheless, large animal models have been preferably used when the presence of the regulatory and homeostatic mechanisms is important, which is indeed the case we were facing (Table 7). Some of the main advantages of using large animals are that the phylogenetical gap is smaller when extrapolating the results into human patients; they allow chronic studies to be undertaken and they are amenable

to almost all the techniques and measurements made in humans. Because primates are usually excluded because of the cost, dogs and pigs have been the most frequently used species for experiments of cardiovascular diseases. Dogs (and other larger animals) are more likely to be used when exploring new cardiac treatments. Commercial swine have been proposed as a good model of human physiology because of the similarity in body weight and their lesions are more like human disease[133]. This was the main reason for choosing the commercial swine as the animal model for the acute experiments of the patch and the whole system.

Table 7. Advantages and limitations in small and large mammals[130].

	Small mammals	Large mammals
Cost		
Data	High reproduction rate; Short mean lifespan; Possibility of genetic modification	Requirement of space for breeding
Clinical Relevance	Phylogenetical distance from human Homogenous genetic background	Similarity to humans in size Allowing longitudinal studies & chronic models

Each animal model[134] has its own limitations and there is no single experimental model sufficient for the investigation of a disease. This is especially true for the treatment of AD, because the precise pathophysiological mechanisms responsible for the development of aortic dissection remain unclear and it is a disease very related to human behavior hard to replicate in animals (aging, hypertension, smoking, etc.). [135,136].

We aim to evaluate the body and tissue response after patch implantation over time. The patch designed will degrade over the months and years and it would be of great interest to study this process. But prior to that, the patch's viability should be tested at short end points, such as acute, sub-chronic and chronic. 30 minutes post-implantation was the timepoint chosen for acute response. These experiments would allow to evaluate the adherence of the patch to the artery and to briefly test the inflammatory response. 7 days post-implantation was the other timepoint chosen, as sub-chronic response. These tests would verify not only the adherence of the patch one week after implantation but also the progression of cells towards the patch and the immune response of the body. 1- and 3- months post-implantation were the chronic timepoints.

Pigs are a good model for acute experiments since they are very similar to humans and are cheaper than other large animals. But pigs continue growing and gaining weight for a very long time. Considering the duration of the chronic experiments, the swine model may not be the best model for prolonged experiments for two reasons. As the animal continues to grow, the aorta would do too, and the results of the experiments may be compromised because the regenerative response may be untranslatable and also the aorta may stretch the patch unrealistically over time. The other reason is more practical: housing and handling such big animals becomes really complicated in all stages of the process, starting with the implantation process.

Consequently, we decided to explore another animal model: sheep and rams. Contrary to pigs, ovine only grow until reaching adult age, making them more suitable for chronic studies. Moreover, the sheep is an excellent model for the study of major physiological systems, such as the cardiovascular, respiratory, renal, reproductive and endocrinological systems[137]. The baseline anatomy and physiology of sheep has been well defined, its size allows for good access

for the insertion of physiological monitoring and sampling devices, and it is a species that recovers quickly from general anesthesia and invasive surgery. Considering all these factors, we decided to explore and consider both animal models depending on the experimentation stage.

4.1.2   Creation of the AD animal model

The other important factor when designing an *in vivo* assay is to explore the options to recreate the disease model. Experimental animal models have been used to investigate the formation, development, and progression of all kinds of diseases for decades[138]. There are a few *in vivo* models to generate type B aortic dissections, while type A is very difficult to replicate. However, surgical models have important limitations due to their invasiveness. Another disadvantage is that the dissection flaps created often expand unpredictable and uncontrollably[139], either with very short length or with undefined propagation and low reproducibility in subsequent experiments. Besides, most existing techniques require invasive surgical procedures such as cutting and suturing on the outer layers of aortic wall, which would inevitably destroy the inherent aortic wall integrity[135]. Moreover, since the surgery necessary to create those AD models is complicated and stressful for the animal, it leads to aorta rupture or heart failure in many the cases. Thus, current methods for development of an AD animal model are too complex, time-consuming, and difficult to follow, or are not similar to the characteristics of typical human AD[134]. The successful rates in creating a model to replicate an aortic dissection are, therefore, very low. Consequently, it was decided to avoid the creation of the false lumen and just test the tissue reaction by implanting the patch on undamaged aortae. In parallel, we created an *ex vivo* model to test the patch behavior under physiological conditions to test the implantation strategy.

4.1.3   Imaging methods

After choosing the animal model to test the patch developed in this thesis, it was important to consider the different options that would be used to evaluate the patch apposition/attachment and integration in the aortic wall. In this sense, it was interesting to consider the clinical tools used for the diagnostic evaluation, treatment decision and management of AD from the clinical perspective. The main imaging techniques used for the diagnosis of AAD[2] are computed tomography (CT), magnetic resonance imaging (MRI), and transesophageal echography (TEE). A less used imaging method but useful in the animal setting is simple vascular echography. A brief description of all these techniques can be found below.

- Computed tomography (CT) plays a central role in the diagnosis, risk stratification, and management of aortic diseases. Its advantages over other imaging modalities include the short time required for image acquisition and processing, the ability to obtain a complete 3D dataset of the entire aorta, and its widespread availability[2]. The simpler version of CT is the X-ray C-arm frequently used in surgical procedures. The main differences between CT and C-arm is that CT uses a narrow beam of X-rays that quickly rotate around the body, producing signals that are processed by the machine's computer to generate cross-sectional images, or "slices" of the body[140]; while the C-arm does not rotate around the whole body and only 2D images can be obtained. As with all X-rays, dense structures within the body, such as bone, are easily imaged, whereas soft tissues vary in their ability to stop x-rays and, thus, may be faint or difficult to see. For this reason, safe intravenous (IV) contrast agents are used during surgery. As polycaprolactone is not visible under X-ray, this technique shall not be used to visualize the implant in vivo. However, the contrast between

blood and the artery wall may make the patch visible "by signal difference" and hence this alternative has also been explored for follow-up during this thesis.

- Magnetic resonance imaging (MRI) can delineate the intrinsic contrast between blood flow and vessel wall, so MRI is well suited for diagnosing aortic diseases. In the acute setting, MRI is limited because it is less accessible, it is more difficult to monitor unstable patients during imaging and has longer acquisition times than CT. Magnetic resonance imaging does not require ionizing radiation or iodinated contrast and is therefore highly suitable for serial follow-up studies in (younger) patients with known aortic disease. It is very likely that our patch will be easily visualized with MRI, but this technique will be considered for future follow-ups in the human tests.

- Vascular echography uses the ultrasound imaging method to visualize the blood vessel directly in the desired place. This technique is not useful when considering an endovascular repair since the probe must be placed in contact the exposed vessel. As the distance is minimal towards the sample location, imaging has little noise. In theory, it should allow for both longitudinal and transversal imaging of the patch.

- Transesophageal echography (TEE) is based on ultrasound imaging, where a probe is introduced and navigated trough the esophagus and oriented towards the desired location. The relative proximity of the esophagus and the thoracic aorta permits high-resolution images with high frequency TEE. However, this technique is only useful for the thoracic aorta near to the aortic arch. In humans, it is reserved for type A AD, but it can be used in the upper part of the descending aorta in animals like sheep.

These imaging techniques allow patch visualization during implantation and/or follow-up but cannot provide any information regarding the tissue response. In this sense, biological techniques have been used to characterize the tissue response and the progression of endothelial cells.

4.1.4 Patch for *in vivo* testing

The final purpose of the patch is to cover human aortic dissections. Aneurysmal aortas tend to dissect at diameters superior to 45 mm [2]. The size of the entry tear could vary, but it is strongly related to survival rates. Patients with entry tears of more than 10 mm have poor prognosis and hospitalization series indicate that patients with dissections exceeding 26 mm are unlikely to reach the hospital alive[141]. In this sense, it was decided that the human version of the patch would be of 30 mm diameter, which should be enough to tackle tears up to 10 mm. But animal aortae are not as large as human, therefore, the size of the patch should be adapted in accordance. For a human aorta of 45 mm in diameter, a 30 mm patch would cover approximately 20% of the aortic perimeter. The equivalent for a pig's artery of 15 mm approximately, is a 10 mm diameter patch. The 10 mm patch covers the same percentage of the aorta.

4.2 Objectives of the chapter

The main objective of this chapter was to demonstrate *in vivo* that the patch developed truly has similar mechanical properties compared to healthy arteries and that provides the best environment for the reendothelialization process. In this sense, the *in vivo* model that better represents the human anatomy and physiology of the aorta was chosen.

To do so, three specific goals have been established:

1. Set the protocol for *in vivo* patch implantation. To do so, a model that closely mimics the animal reality, using a phantom or an *ex vivo* system, would be used.

2. Perform acute and sub-acute *in vivo* tests to demonstrate patch attachment. Co-optimize with other team members other elements (adhesive, deployer) that affect the implantation process.

3. Perform chronic *in vivo* tests to evaluate the long-term biological response to the patch, including re-endothelization, thrombogenicity and inflammation processes.

4.3 Results

4.3.1 Protocol for *in vivo* implantation of the patch

Up to this point, the patch adherence was only tested *in vitro* on cell culture plates. It was therefore necessary, before implanting the patch in a living animal, to demonstrate that the patch attaches to a native explanted aorta, what is called an *ex vivo* test. In this process, there were two other variables affecting the patch's attachment: the adhesive and the deployer, both developed by other members of the research group and hence not part of this thesis. Briefly, the cyanoacrylate-based adhesive presents a good shelf life, great tensile shear strength and a fast-curing time at room temperature without the presence of a primer. The deployer has been especially designed to carry, deploy, and apply pressure to the patch during the attachment process in the desired dissected vessel. The deployer has the shape of a flower and it is made of nitinol, a widely used material in cardiovascular devices.

The *ex vivo* tests consisted in using an explanted aorta to evaluate the patch adherence and compliance to the tissue using different implantation conditions. The final objective of these tests would be to design and develop the protocol for animal implantation. As the *in vivo* tests would be performed in pigs and because the pig's aortae are the easiest to get from the slaughterhouse, it was decided to use them for the *ex vivo* tests. The *ex vivo* tests have evolved over time to bridge the gap the natural environment. In this sense, we designed and manufactured a chamber with an artery suspended to recreate the *in vivo* situation (Figure 77).
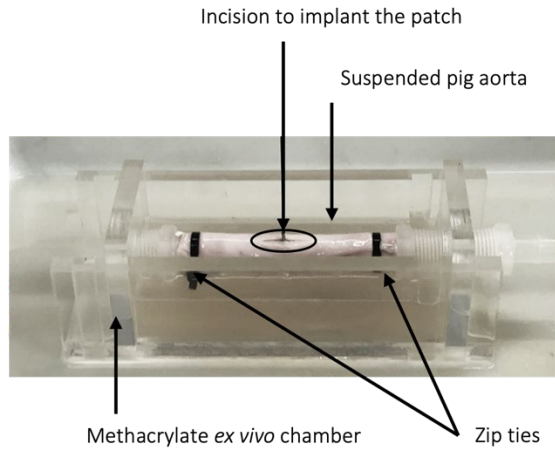
Figure 77. *Ex vivo* chamber with a suspended aorta.

The implantation process started exposing the aorta's inner luminal space with a 5 cm incision. After, the patch was implanted on the lumen using the deployer. We soon realized that the pressure applied to the patch and hence, to the artery, depended on the operator. To minimize the human contribution to the obtained results, we designed an applier system to control the force applied to the system (Figure 78).
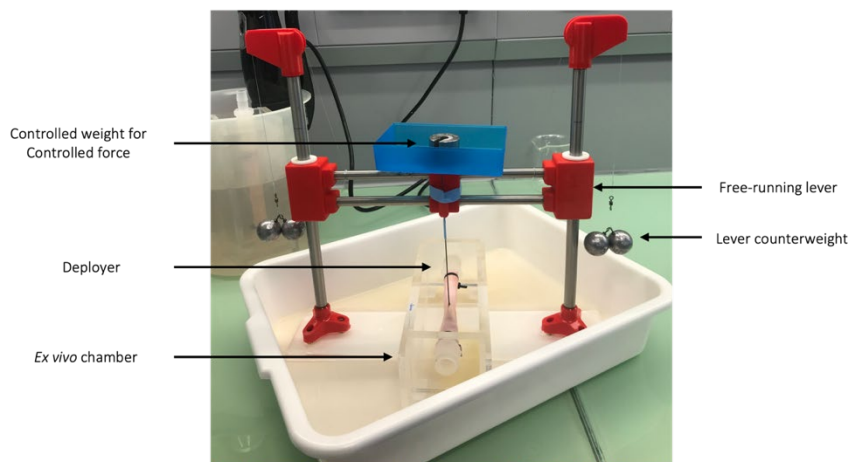
Figure 78. Pressure applier machine.

Thanks to the *ex vivo* chamber and to the pressure applier machine (PAM), the implantation conditions were established. The conditions were implanting the patch for 1 minute, holding the deployer at 90º and applying a force of 0.981 N, thanks to a 100 g weight. All this resulted in the controlled force deployer showed Figure 79 which allowed patch implantation *in vivo*.

Running guide

Controlled weight (1N ~ 100g)

Weight holder and stopper

Nitinol concave flower
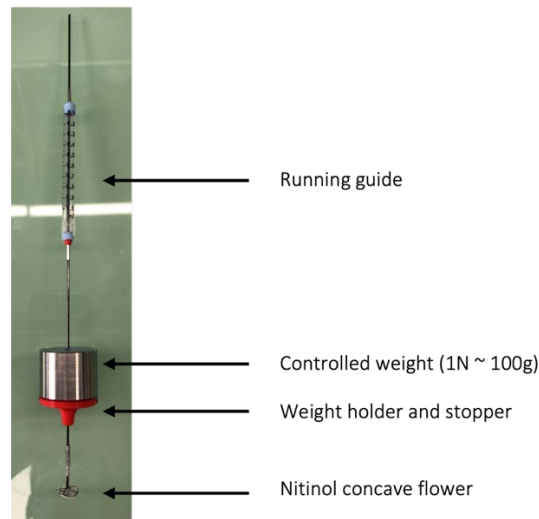
Figure 79. Controlled force deployer (CFD).

4.3.2   Acute *in vivo* tests

Regarding the surgical procedure, the patch has been designed to be implanted via an endovascular procedure. In this sense, an endovascular catheter that can navigate along the artery and approach the entry tear to smoothly display and attach the patch to the artery's wall should be designed. But since the endovascular catheter would represent a project itself, an easier approach was followed, an open surgical approach. The open surgery approach represents a simplification on the process since only the implantable parts of the device were tested: the patch and the adhesive. This thesis is focused only on the results on the patch. None of the parameters optimized for the adhesive, such as the amount or the distribution used are part of the result discussion.

4.3.2.1   Acute pig model

In every animal test, at least three animals were treated using the same conditions. In the first set of acute tests, the patch was implanted in three male swine and the experiments took place at the Serveis Integrats d'Animals de Laboratori (SIAL) at Universitat Autònoma de Barcelona. The veterinaries at SIAL performed the open surgery. This surgery consisted in a thoracotomy at the 5-6 intercostal level that allowed to expose the aorta similarly to the *ex vivo* tests. Animals were placed in right recumbency to access the descending thoracic aorta. The aorta was exposed and cross-clamped to stop blood flow during the procedure (Figure 80). Please refer to section 5.4.3 from materials and methods for a comprehensive explanation on the implantation procedure.
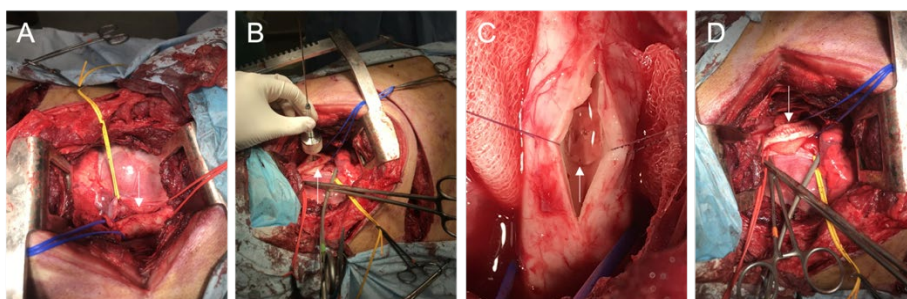
Figure 80. Implantation procedure performed with a pig model. Image A shows the process of accessing and exposing the artery, the white arrow remarks the aorta. Image B shows the exposed artery cross-clamped during the implantation process. Image C shows the aorta with an implanted patch right before suturing the artery. The arrow indicates where the presence of the patch. Image D shows the aorta sutured after the implantation process and before euthanizing the animal. The arrow remarks the sutured aorta.

All three implantations underwent similarly, and more than one attempt was needed to finally implant the patch correctly into each artery. It was usual to perform more than one implantation attempt in these procedures since the cavity was deep and difficult to access, making the operating space limited. After the 30 minutes, animals were euthanized. The part of the aorta that contained the patch was excised trying not to compromise the artery's integrity. Said part was preserved in PFA to carry out the subsequent histopathological analysis. The results of each animal are shown in Figure 81.
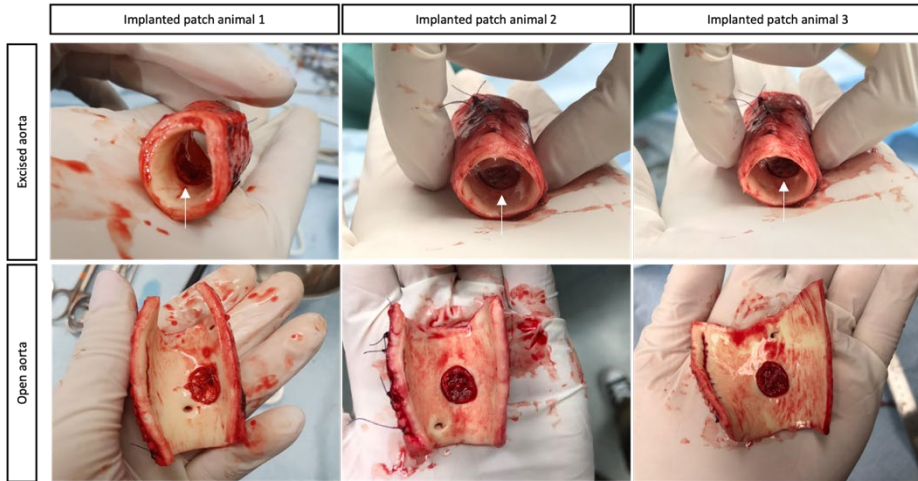
Figure 81. Excised aortae of the three swine. White arrows facilitated the visualization of the patch when the artery remains unopened.

After necropsy, the thoracic aorta at the site of patch implantation was sampled and submitted for microscopic evaluation.

4.3.2.1.1 Histological analysis

All the histological procedures and subsequent analysis was subcontracted to SIAL pathologists. The samples were processed using two different histological protocols with paraffin or cryopreservation. All sections were stained with Hematoxylin-Eosin & Saffron (HE&S). The presence of the patch was not observed in any slide due to the histological procedure.
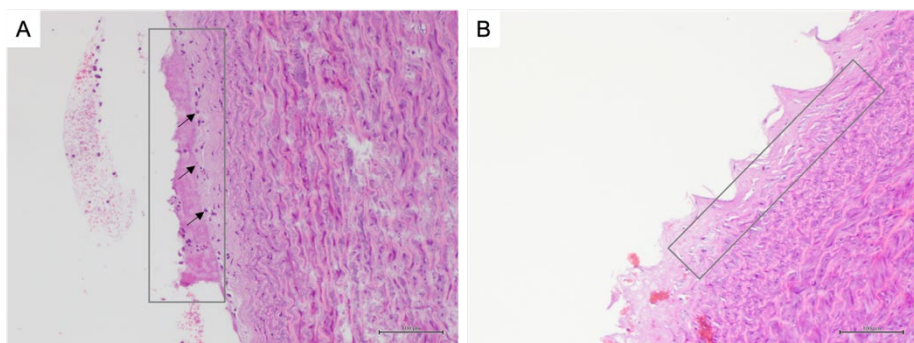
Figure 82. Histological analysis of tests performed in pigs. Image A shows a site of implantation with the presence of fibrin deposits in the rectangle area with the presence of inflammatory cells marked with arrows. Figure B shows how collagen fibers were disaggregated in the implantation site.

The main findings after analyzing the slides were that there was a minimal inflammatory reaction from the tissue with the presence of fibrin deposits and minimal inflammatory cells (Figure 82 image A). Although the patch was not present on the slides, its presence was still latent as observed in Figure 82 image B. Small epithelium waving can be observed where the patch was. Moreover, underlying smooth muscle cells were also disaggregated, may be due to an excessive pressure applied by the system during the implantation process.

4.3.2.2   Acute ovine model

After these promising results, we decided to move forward to prolonged tests. As stated in the introduction of this chapter, the animal model was changed to rams to prevent growth-related artifacts. Rams are larger than sheep and have larger aortae, which is of great interest to have enough space to implant the patch. Moreover, it was decided to continue with the tests in a different animal facility, the Institute Mutualiste Montsouris Recherche (IMMR), a worldwide leader in testing cardiovascular devices.

An acute test was repeated with the new animal model before proceeding with the sub-chronic experiments. The surgical procedure was really similar to the one performed at SIAL, but the ovine cavity is not as deep as the pig's cavity; therefore, it was easier to reach the aorta with the deployer without touching the walls of the aorta. The results obtained for the rams are shown below (Figure 83). After explanting the first aorta (post 30 minutes test), a coagulation excess was detected inside. Consequently, the veterinaries from IMMR decided to duplicate the dose of heparin, from 0.5 mg/Kg to 1.0 mg/Kg. As in the previous procedure, the excised aortae were fixed in PFA to carry out the subsequent histopathological analysis.
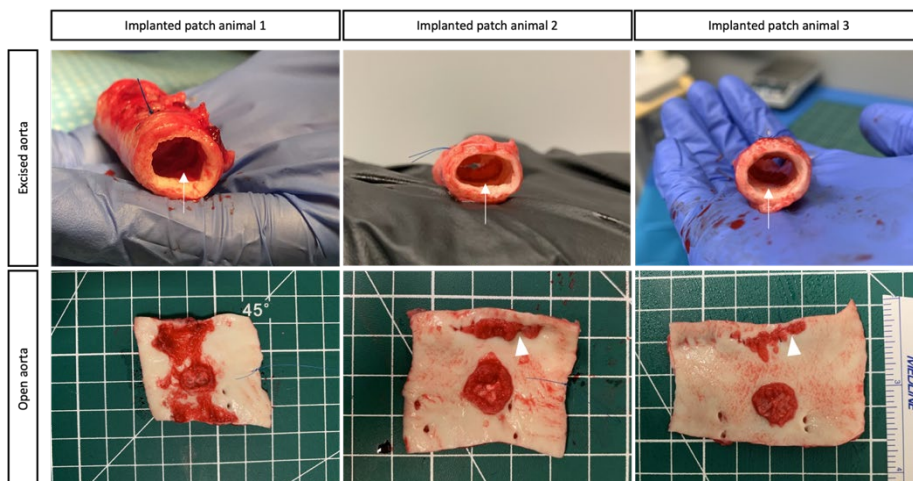
Figure 83. Excised aortae of the three rams. On top images, white arrows facilitated the visualization of the patch when the artery remains unopened. On the bottom images, white arrowheads indicate the platelet accumulation around the sutured incision. The accumulation in the first animal was all over the incision site.

At necropsy, the thoracic aortae at the site of patch implantation as well as at the site of the aortotomy and suturing were sampled and submitted for microscopic evaluation.

4.3.2.2.1 Histological analysis

All histological procedures and subsequent analysis were subcontracted to IMMR pathologists. In this feasibility study, as the implanted patch was a thermosensitive scaffold and the regular paraffin melts at approximately 65 ºC (PCL's melting point is 60 ºC), different histological protocols were tested to investigate the best way to preserve the patch. Frozen sections with or without 10% Neutral Buffered Formalin (NBF) fixation and routine paraffin sections were then performed. Frozen sections were stained with HE&S. Paraffin sections were stained with HE&S and Movat Pentachrome. All sections stained with HE&S and Movat Pentachrome were microscopically screened for histopathological changes. Microscopic changes were identified from each section, qualitatively described and (if applicable) semi-quantitatively scored using distribution qualifiers (i.e. focal, multifocal, locally

extensive or diffuse) and a five-scale severity grade (i.e. 1: minimal; 2: mild, 3: moderate, 4: marked or incomplete, 5: severe or complete).

Serial samples of the aorta with an implanted patch were examined. In frozen sections, both from fixed or fresh frozen samples, the patch material appeared as an unstained, refractile and fibrillar network. The adhesive was observed as an unstained, homogeneous and refractile material on the surface of the intima. As expected, in paraffin sections, patch and/or adhesive material were very poorly observed due to melting of the thermosensitive patch material.
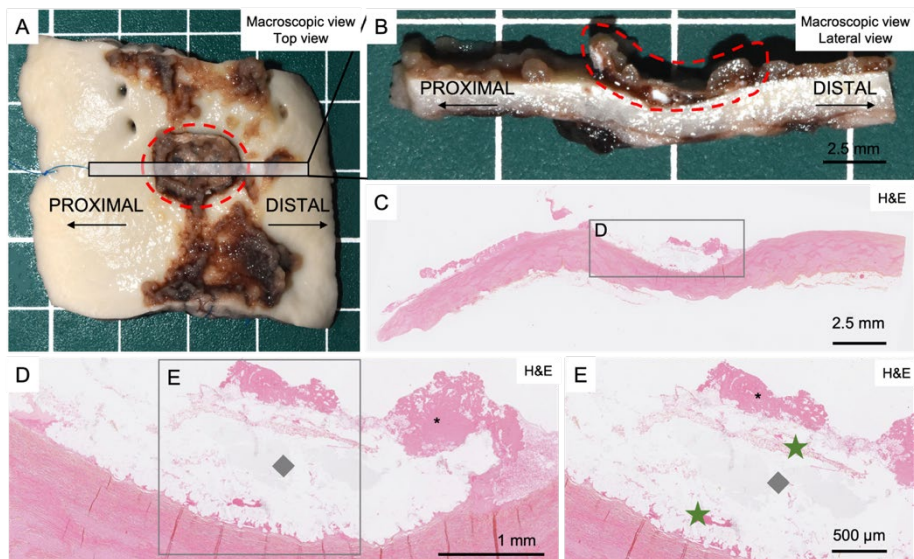
Figure 84. Histological analysis of animal 91439. Image A shows the thoracic aorta at the site of implantation with the patch attached (marked in red). Image B shows the aorta cut from proximal to distal containing the patch (marked in red). Image C shows one histological section of image B which it was stained with H&E. This image shows the place where the patch is attached, the patch is marked with a grey square. Image E evidence the presence of red blood cells (marked with a green star), the patch marked with a grey square and the fibrin deposits above it (marked with an asterisk).

The patch was detached from the adhesive in some samples, most likely due to trimming, and the adhesive was present at the intimal surface of the aorta. The intima was completely or almost completely devoid of endothelial cells in all sections due to the implantation process and posterior manipulation. Minimal to mild multifocal hemorrhages were noted within the patch in most

sections. Multifocal, minimal to mild fibrin deposits were also observed in most sections, at the intimal surface of the aorta, between the adhesive and the intima, on the surface of the patch or within the patch material. Hemorrhages and fibrin deposits would be due to the acuteness of the test (Figure 84). The evolution of these phenomena would be studied in the following tests.
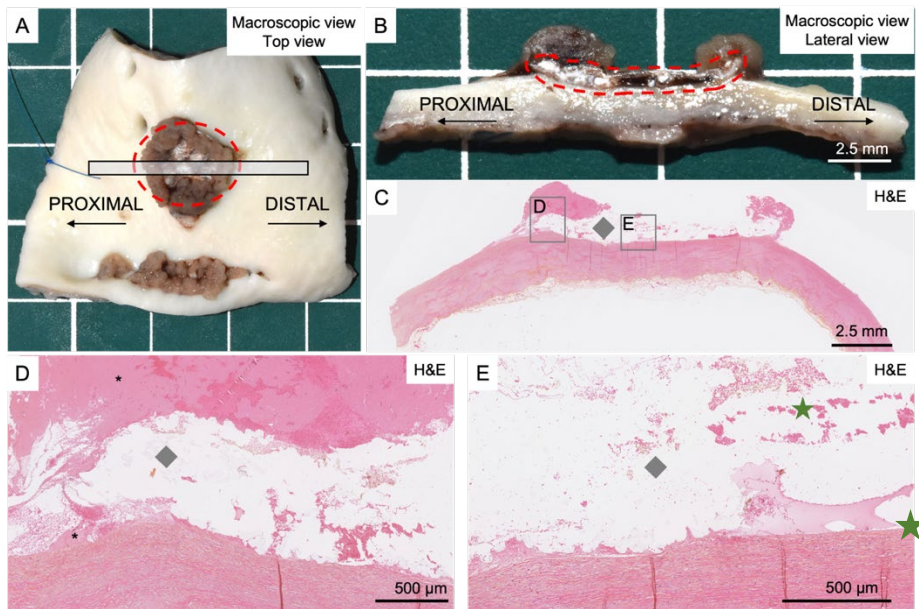
Figure 85. Histological analysis of animal 18025. Image A shows the thoracic aorta at the site of implantation with the patch attached (marked in red). Image B shows the aorta cut from proximal to distal containing the patch (marked in red). Image C shows one histological section of image B which it was stained with H&E. This image shows the place where the patch is attached, the patch is marked with a grey square and fibrin deposits are marked with an asterisk. Image E evidence the presence of red blood cells (marked with a green star) and the patch marked with a grey square.

In frozen sections, the patch was detached from the adhesive, most likely due to trimming, and the adhesive was present on the intimal surface of the aorta. Similarly to the previous slides, the intima was completely or almost completely devoid of endothelial cells in all sections (Figure 85). Microscopic findings consisted of minimal to mild multifocal hemorrhages and minimal to mild fibrin deposits at the intimal surface of the aorta, at the site of patch

implantation or of aortotomy, around the sutures, between the adhesive and the intima, on the surface or of the patch or within the patch material.

In conclusion, microscopic findings correlated with macroscopic observations at explantation. Microscopic changes were within the range of expected findings after implantation of a resorbable patch in an acute ovine model of aortotomy. The results of both acute tests are summarized in Table 8.

Table 8. Summary of histopathological results for the acute tests

Animal model	Test time	Adhesion post flow	Histology results
Pig (swine)	Acute response 30 minutes flow	3/3	Small fibrin deposits No tissue inflammation
Ovine (ram)	Acute response 30 minutes flow	3/3	Loss of endothelium Small clots and hemorrhages No tissue inflammation

4.3.3 Chronic and sub-chronic tests

4.3.3.1 Sub-chronic group 1 (7 days blood flow test)

The main difference with acute tests was that animals had to recover from surgery. Aorta clamping time became critical because, as explained in the introduction section, the aorta provides fresh blood to all the organs in the body, including the spinal cord. Following the veterinaries' opinion, a maximum clamping time of 20 minutes should not be surpassed, as it could cause fatal damage to the animal and compromise the results of the study. Moreover, procedural and material sterility became critical to prevent infections. With all these considerations, a first sub-chronic specimen, aimed at 24 h post-implantation, was performed before proceeding to longer tests.

The surgical procedure underwent analogous to acute tests, paying attention to minimize clamping time. Although everything was strictly prepared, two attempts were necessary to implant the patch. The second patch implanted was considered strong enough considering time limitation. In this case, we performed a vascular echography at the implantation site right after restoring blood flow to visualize, live, the unclamping procedure and evaluate the patch attachment once flow was restored. The patch can be perfectly identified with the vascular echography, so veterinaries closed the animal and began the recovery procedure (Figure 86).
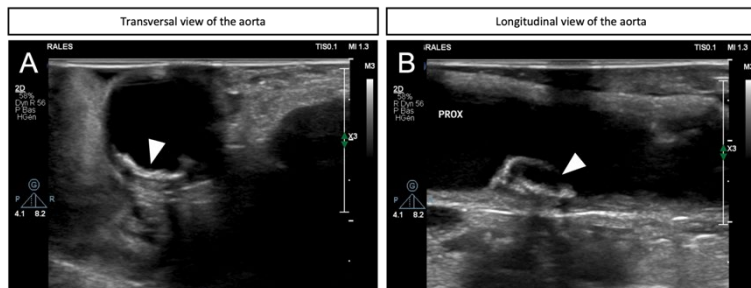
Figure 86. Vascular echography right after declamping the aorta. Arrowheads indicate where the patch is. Image A shows the transversal view of the aorta and, image B shows the longitudinal view of the aorta.

After 20 hours of the implantation surgery, the animal was not able to stand up and showed pain and immobility in its lower limbs. The main hypothesis for this symptomatology was that the artery was clamped for an excessive period, therefore causing renal failure and paralysis of the lower body. The animal died while the IMMR team was anesthetizing it for the explantation surgery. A vascular echography was performed after sacrifice; the patch was still in place and was visible. No clots nor thrombi were observed. The explantation was performed and the patch was in place presenting a small fold already observed in the first echo after the implantation process. The aorta was not opened to further perform the histopathological evaluation (Figure 87).
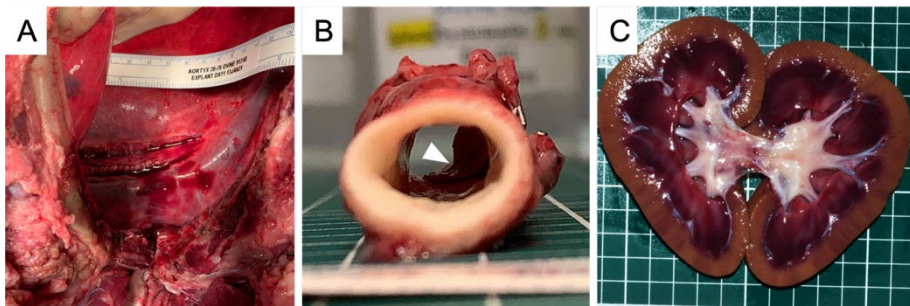
Figure 87. Explantation results of animal number 1 (Ovine 91248). Image A shows the aorta inside the animal's chest; image B shows the explanted aorta with the patch inside marked with an arrowhead; and C shows one of the explanted kidneys that shows the presence of small infarcts inside.

An autopsy was performed to determine the cause of death. The urinary bladder was full of hemorrhagic urine and both kidneys presented hydronephrosis, most probably due to spinal cord infection. Clinical examination was compatible with hyperkalemia (very high level of potassium in blood), and the main hypothesis was that clamping of the collateral and thoracic arteries induced spinal cord damage. After a discussion with the IMMR team, we decided to repeat the same procedure trying to be committed with the 20 minutes clamping time. Depending on the results on the second animal, we would have to follow a different surgical strategy, a cardiopulmonary bypass (CPB).

We performed the same open surgical procedure to the second animal and the procedure of assessing and exposing the aorta was easy and straightforward, but the implantation was complicated. A first patch detached after implantation and the second one stood in place. The animal was clamped for 15 + 25 minutes, much more than the optimal 20 minutes for a proper recovery of the animal. After implantation, a vascular echography perfectly identified the patch in the implantation zone before and after declamping (Figure 88).
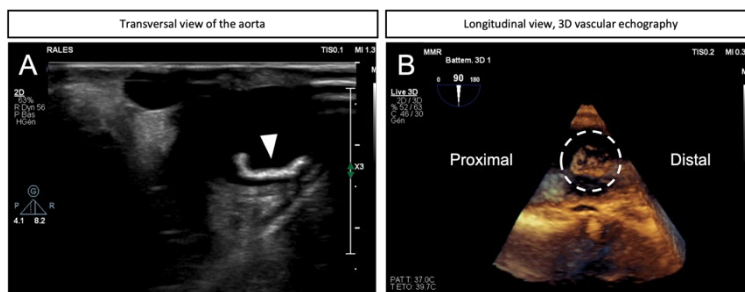
Figure 88. Vascular echography right after declamping the aorta. Arrowhead and doted circle indicate where the patch is. Image A shows the transversal view of the aorta and, image B shows the longitudinal view of the aorta.

After 18 hours post-implantation the animal was immobile, unable to urinate and showed pain in its lower limbs. The animal was euthanized by the IMMR team for ethical reasons. No vascular echography was performed before explanting the aorta. The explantation was performed and the patch was observed in place without any flap or detachment. There was no visible thrombus over the patch or the implantation area. The aorta was not opened to further perform the histopathological evaluation.
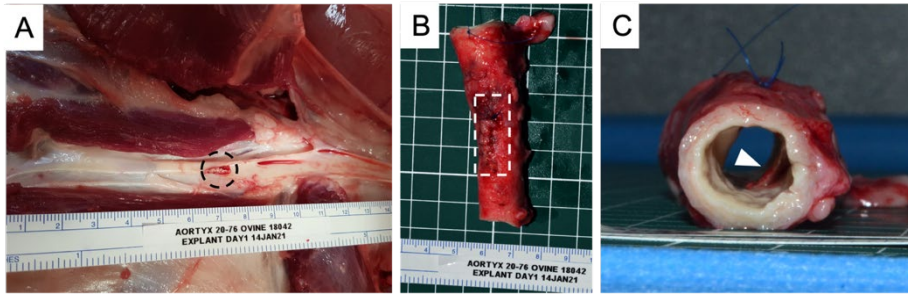
Figure 89. Explantation results on animal number 2 (Ovin 18042). Image A shows the embolized patch in one of the femoral arteries. Image B shows the explanted aorta with the sutured incision marked with the doted rectangle. Image C shows the lateral view of the aorta with the patch inside marked with the arrowhead.

The first attempt patch that was embolized the day of implantation, was found in the left iliac artery. No lesion nor thrombus were observed so blood was able to flow through this vessel despite the presence of the patch.

It is remarkable that, although animals were not able to stand up and had urinary problems after surgery, the patch was still in place after the blood flow test in both cases. The post-surgical problems were due to the duration of the clamping procedure, so we decided to change the surgical procedure and implant the patches with the animal under CPB. CPB provides a bloodless field for cardiac surgeries by incorporating an extracorporeal circuit. This circuit provides physiological support in which venous blood is drained to a reservoir, oxygenated, and sent back to the body using a pump. It is a complicated surgical procedure, but that allowed implantation procedure without time limitations while avoiding post-surgical complications[142]. See section 5.4.4 for more details.

The next three animals underwent the CPB procedure. When undergoing CPB, the whole flow bypass setup was assembled and started after exposing the artery, but prior to clamping the aorta. After CPB was ready and started, the implantation process continued as in the previous tests. One patch was

implanted in each animal after one or two attempts, depending on the case, without further complications. The right attachment of the patch was checked right after declamping the artery via a vascular echography in each case. All patches looked well attached without the presence of significant flaps nor thrombi. All animals recovered from surgery without further complications, being able to stand up and urinate in the first hours post-implantation. CPB was clearly necessary to avoid post-surgical complications.

4.3.3.1.1 Follow-up 3 days post-implantation

A 3-day post-implantation follow-up sing TEE was performed to evaluate patch attachment over time. The use of this technique was possible because the patch was attached to the descending aorta right after the arch. It requires anesthetizing the animal to introduce the probe through the esophagus, but is less invasive than the vascular echography, directly performed on top of the vessel. All three animals were in good clinical condition and their wounds were healing nicely. Animals did not present sings of pain nor affection to spine; neither problems to eat nor urinate. In the first chronic animal (Ovine 91406), the patch was still visible, with the presence of a little folding. No visible thrombus over the patch were observed and the flow at the implantation zone was correct. In the second chronic animal (Ovine 91019), the patch was still visible but seems to be detached on its proximal part. An echogenic element was visible on the proximal part of the patch and was floating (moving with heartbeats). It was probably fibrin or a thrombus; but this could only be confirmed at explantation. Hematoma was observable along the suture side; no stenosis was observed, and the flow at the implantation zone was correct. For the last animal (Ovine 18088), the patch was still visible and well attached to the aorta's wall without the presence of any flap or detachment. No visible thrombus over the patch was observed and the flow of the implantation zone was correct. The most interesting finding from these follow-ups was to verify

that the patch accompanies the aorta's movements in every distention and recoil process, confirming that the mechanical properties match those of healthy arteries.
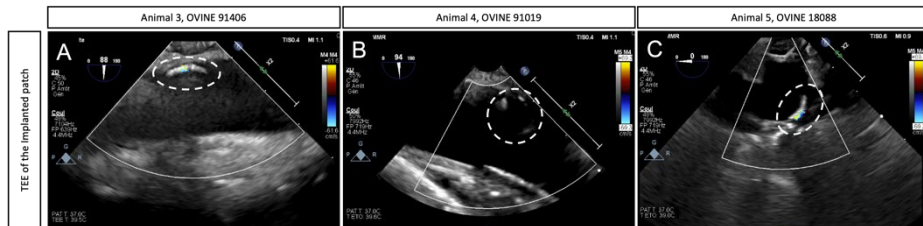
Figure 90. 3-day post-implantation follow-up via TEE Circles indicate where the patch is in each image.

4.3.3.1.2 Explantation after 7-day blood flow

Animals were in good clinical condition 7 days post-implantation. TEE follow-up was performed in each animal before euthanizing them. Once animals were euthanized, the aorta loses its flexibility and can be retracted. Therefore, TEE helps evaluating the true state of the patch before explantation and compare the results post-explantation.

The patch in animal 91406 was still visible, with the little detachment, already visualized in the follow-up echo. No visible thrombi were observed and flow at the implantation zone was correct. After euthanasia, a hematoma was visible on the surface of the aorta, most probably due to the surgery. The explantation was performed and the patch was in place with a partial detachment from the distal part. No visible thrombus was observed.

In animal 91019, the patch was still visible, but the echo showed a slightly detachment on the distal side. This detachment was confirmed during the explantation process. Even though the patch looked in place, it was partially detached from the left distal part. No thrombus around or above the patch were observed. In the last animal, 18088, TEE showed the patch well attached to the aorta's wall without any flap or detachment. The patch was in place at

explantation. After the examination, the patch was mildly detached from the middle section, and this was related to the manipulation and the contraction of the aorta after the demise of the animal and aorta extraction (Figure 91). All aortas were fixed in 10% neutral buffered formalin for at least 48 hours to proceed to histopathology. After fixation, the aorta at the site of patch implantation with the patch was sectioned longitudinally and samples were orientated along the proximal-distal axis using tissue dye. It was difficult to maintain the patch attached to the aorta during the trimming process.
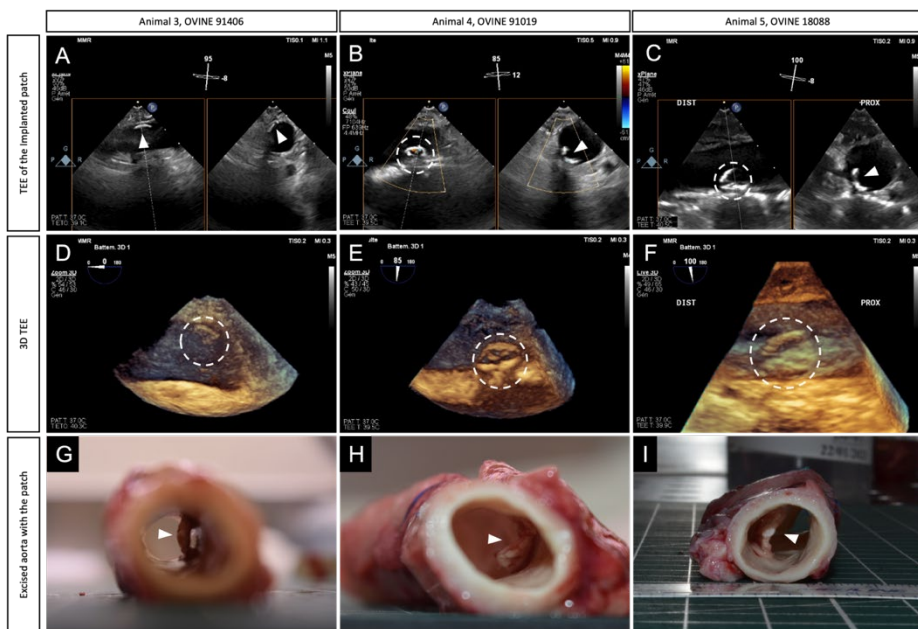
Figure 91. Explantation results of chronic group 1, 7 days test.

Other than the aorta, the other organs were macroscopically analyzed to check if the presence of the patch caused any collateral lesion. The heart, both adrenal, liver and brain of the ovine showed no macroscopic lesions. The spleen presented minimal diffuse congestion related to the euthanasia. Lungs showed acute pulmonary edema related to the euthanasia, minimal multifocal fibrosis of the pleura related to the surgery process and minimal multifocal hemorrhage most likely due to anesthesia. Both kidneys showed numerous minimal multifocal lesions related to a subacute renal infarct.

4.3.3.1.3   Histological analysis

The microscopic changes were separated into two groups: the findings on the subacute group (one day post implantation) and the findings on the sub-chronic group (seven days post implantation).

4.3.3.1.3.1   Subacute Group (one day post implantation)

IMMR was only able to analyze one sample preserving the patch attached to the aorta after all the histology process. There were minimal multifocal red blood cells and fibrin deposits within the patch, mostly on its abluminal aspect and within the adhesive (Figure 92).
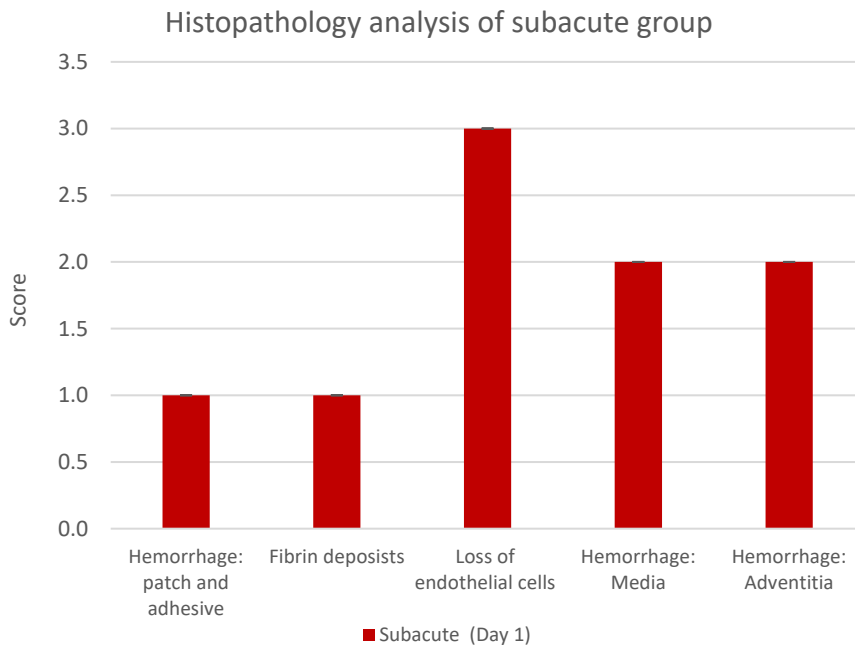
Figure 92. Subacute group. Summary of microscopic changes at the implantation site (Patch, adhesive and aorta, N=2, 2 histological sections).
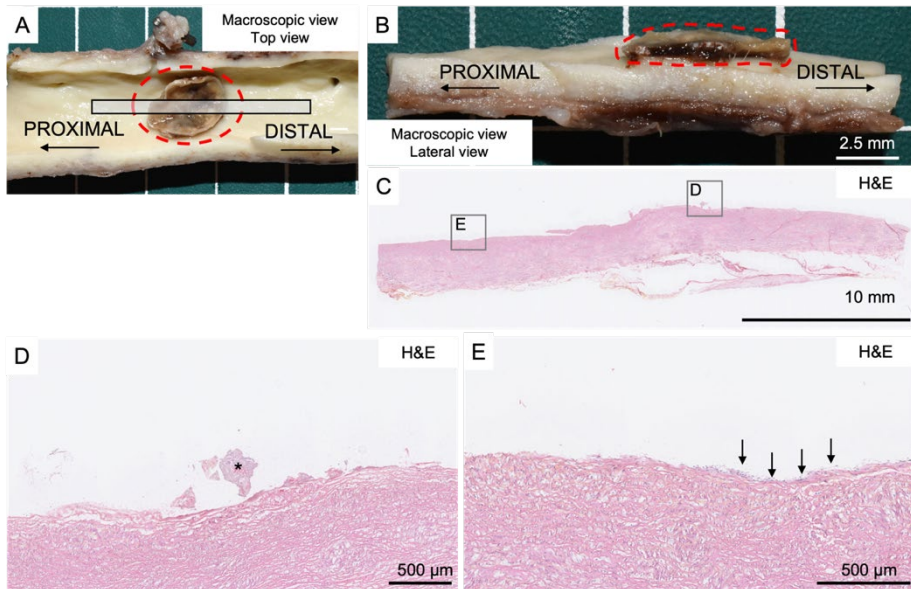
Figure 93. Histological analysis of animal 91248. Image A shows the thoracic aorta at the site of implantation with the patch attached (marked in red) having approximately 30 % of the patch detached. Image B shows the aorta cut from proximal to distal containing the patch (marked in red). Image C shows one histological section of image B. The staining used was H&E in all the images showed in this figure. Image D shows the place where the patch is attached, but the patch is rarely visible under this kind of staining. Small fibrin deposits are marked with an asterisk. Image E shows a small portion of the aorta, from left to right, loss of endothelium to presence of it (endothelial cells can be identified in blue, black arrows on top).

In animals from the subacute group, at the site of implantation of the patch, minimal multifocal fibrin deposits were observed on the luminal surface of the intima. The intima was moderately devoid of endothelial cells underneath the implanted patch in both animals. But a minimal to moderate multifocal reendothelialization (i.e. turgescent endothelial cells on the luminal surface of the intima) was observed in all sections (see image E on Figure 93). This was accompanied by a minimal and multifocal subendothelial layer of loose connective tissue in animal 91406 (Figure 93). Rare mild multifocally hemorrhages were observed in the media of the aorta. At the site of aortotomy, there was also a moderate multifocal loss of endothelial cells on

133

the intima in animal 91248 and minimal to moderate multifocal hemorrhages in the media in both animals were observed in the aorta.

4.3.3.1.3.2   Sub-chronic Group (seven days post implantation)

IMMR was only able to analyze two of the three samples preserving the patch attached to the aorta after all the histology process due to the complication of manipulating the samples. The main microscopic findings are summarized in Figure 94.
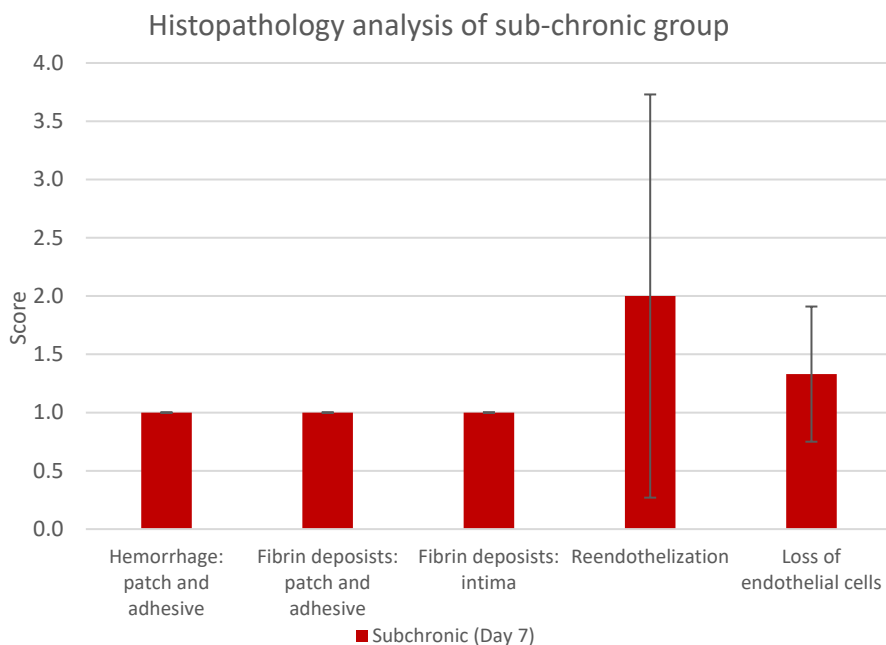
Figure 94. Sub-chronic group. Summary of microscopic changes at the implantation site (Patch, adhesive and aorta, N=2, 2 histological sections)

The patch and the adhesive allowed cell invasion as minimal red blood cells and fibrin deposits were observed inside the patch (mostly on the abluminal side) and the adhesive in all implanted animals. Minimal multifocal fibrin deposits were also observed on the edges of the luminal aspect of the patch and were equivalent on the proximal and distal edge of the patch. As no inflammatory cells were observed on the patch nor the device, local tolerance of the implanted device was considered excellent. No signs of resorption or

hyaline hydrolysis were observed on the patch nor on the adhesive. Other microscopic findings were observed in the adipose tissue and included mild multifocal hemorrhages in all sections, mild multifocal necrosis (i.e., infiltration of macrophages and large multinucleated giant cells at the periphery of fat droplets occasionally containing pale basophilic deposits corresponding to calcification) in all sections and minimal multifocal fibrin deposits.

Considering the site of implantation, the intima was minimally to mildly devoid of endothelial cells underneath the implanted patch in all animals. At the same time, there was a minimal to marked multifocal reendothelialization of the intima in all animals. However, there was no reendothelialization of the luminal surface of the patch (Figure 95).
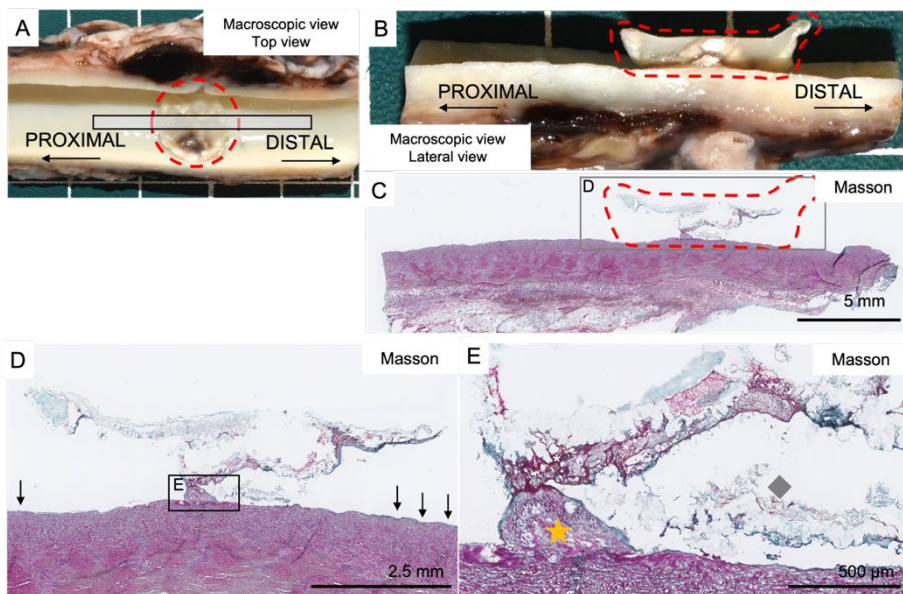
Figure 95. Histological analysis of animal 91406. Image A shows the thoracic aorta at the site of implantation with the patch completely attached (marked in red). Image B shows the aorta cut from proximal to distal containing the patch (marked in red). Image C shows one histological section of image B. The slide was stained with Masson Trichrome. Image D shows how the patch is still in place and stained in blue with Masson Trichrome. Reendothelization is marked with black arrows. Image E shows the site where there is formation of fibrous tissue (marked with a yellow star). There are also fibrin deposits marked with an asterisk and the presence of the patch is marked with a grey square.

In conclusion, microscopic findings correlated with macroscopic observations at necropsy. These changes were within the range of expected findings seven days after implantation of an absorbable device on the intima of the aorta. The local tolerance was considered excellent. No signs of resorption were observed at this timepoint. Given that there were several manipulation artifacts, it was decided to study better ways of preserving the aorta after explantation, especially those related to patch adhesion to the aorta and, therefore, to be able to study the patch-tissue interaction.

Table 9. Chronic group 1. Summary of the tests.

Animal number	Surgery type	Flow duration	Follow-up results at 3 days	Explantation results + Histopathology results
Animal 1 (Ovine 91248)	Open surgery, non-CPB	24 hours	N/A	Patch in place. Presence of minimal multifocal red blood cells and fibrin deposits. Loss of endothelium.
Animal 2 (Ovine 18042)	Open surgery, non-CPB	18 hours	N/A	Patch in place but detached in the trimming process. Presence of minimal multifocal red blood cells and fibrin deposits. Loss of endothelium.
Animal 3 (Ovine 91406)	Open surgery, CPB	7 days	Patch visible with presence of bit folding. No visible thrombus. Normal flow around.	Patch in place in all cases. local tolerance of the implanted device was considered excellent. Minimal multifocal fibrin deposits were also observed on the luminal aspect of the patch. Minimal to moderate multifocal reendothelialization of the intima.
Animal 4 (Ovine 91019)	Open surgery, CPB	7 days	Patch visible, partially detached proximal site. Presence of an echogenic element.	
Animal 5 (Ovine 18088)	Open surgery, CPB	7 days	Patch visible and well attached. No flaps. No visible thrombus	

4.3.3.2 Chronic group (30- and 90-days blood flow test)

In the view of the promising results obtained at 7 days, a chronic group was scheduled for 30- and 90-days implantation tests to evaluate the tissular and cellular reaction to the patch. Follow-ups via TEE were scheduled after 7, 14, 28, 42, 56, 70 and 90 days. The body reacts in the presence of a foreign artifact generating an immune response creating fibrin deposits etc. In this immune response it also interferes the reendothelization process[143,144].

The surgery to implant the patch in all animals was performed analogously to the 7 days experiments: open surgery under CPB. A vascular echography was performed after suturing the artery and restoring blood flow before stopping CPB (Figure 96, 30 days and Figure 97, 90 days experiments).
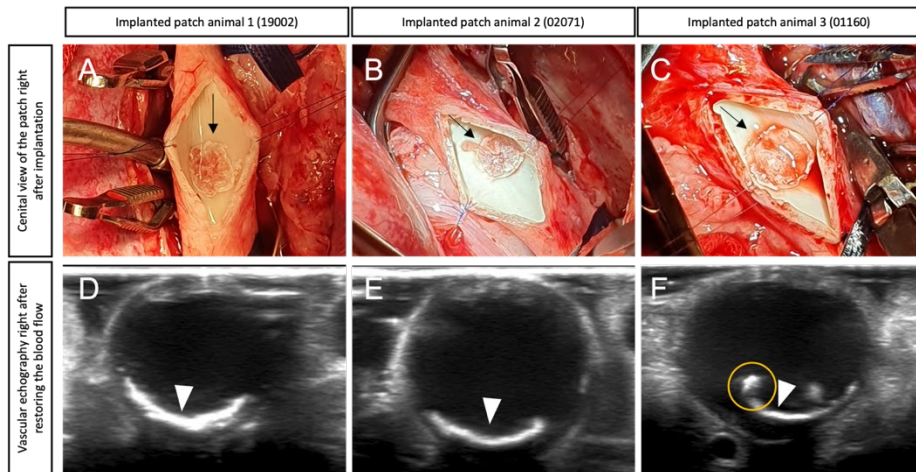
Figure 96. 30 days chronic group, implantation process. View of the patch in each animal right after implantation, before suturing the artery to restore the blood flow (images A, B and C). Black arrows indicate the direction of the blood flow, from proximal to distal. Ultrasound visualization of the patch in each animal after suturing the artery and restoring blood flood (images D, E and F). The vascular echography was performed having the animal under CPB control. The white arrow heads indicate the presence of the patch on the artery. The yellow circle indicates the partially detachment of the lateral part of the patch.

After ensuring the proper adhesion of the patch, the thoracotomy was sutured, and the animal recovered from surgery. The vascular echography showed the well apposition of the patch in animals 19002 and 02071. On the contrary, the patch in animal 01160 seemed to be partially detached from the artery on the lateral part. Since three attempts were necessary to finally implant the patch due to complications in animal's anatomy, we decided to keep the last implantation as the final one. No complications were observed for the 90 days animals.
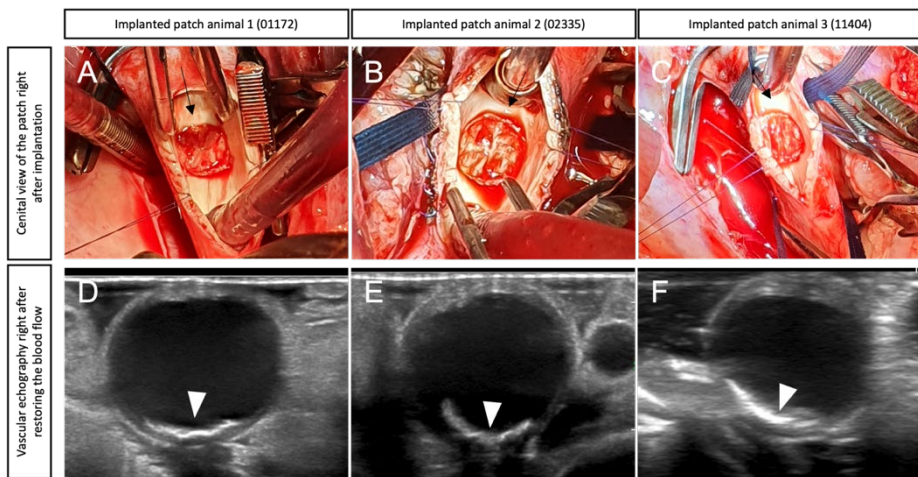
Figure 97. 90 days chronic group, implantation process. View of the patch in each animal right after implantation, before suturing the artery to restore the blood flow (images A, B and C). Black arrows indicate the direction of the blood flow, from proximal to distal. Ultrasound visualization of the patch in each animal after suturing the artery and restoring blood flood (images D, E and F). The vascular echography was performed having the animal under CPB control. The white arrow heads indicate the presence of the patch on the artery.

All the follow-ups underwent without further complications and all the patches remain in place during the flow test. The most remarkable finding in TEE follow-ups was observing how the patch accompanies the aortic motion over time. The last follow-up performed was right before euthanizing the animal at day 30 or day 90. The results of each group of animals are presented separately (Figure 98 and Figure 99).
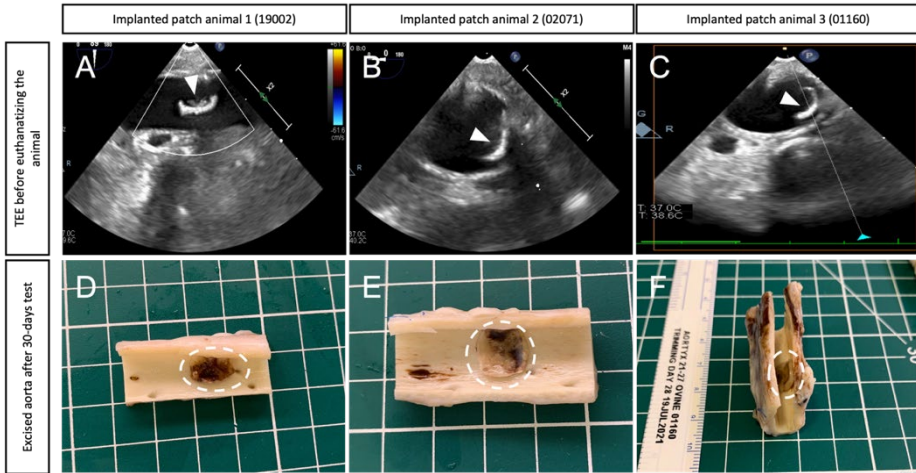
Figure 98. 30 days chronic group, explantation process. View of the patch in each animal in a TEE right after euthanizing the animal (images A, B and C). The white arrow heads indicate where the patch is located. View of each explanted aorta containing the patch marked with white discontinuous circles (images D, E and F).
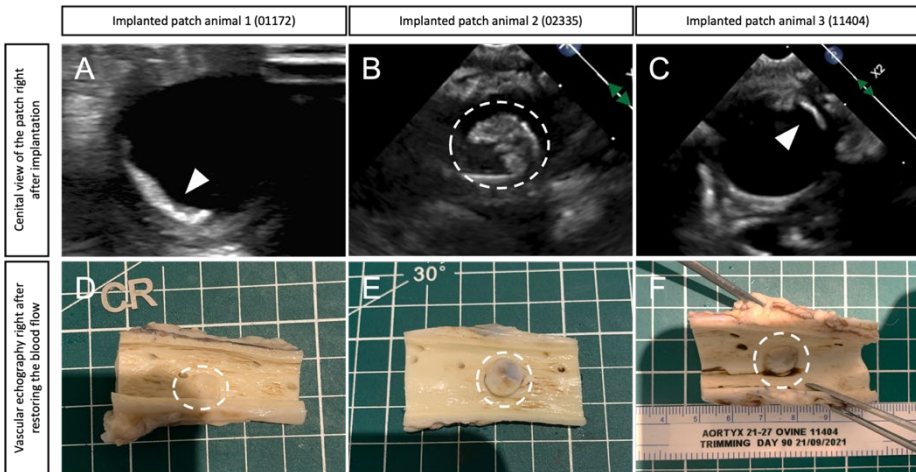
Figure 99. 90 days chronic group, explantation process. View of the patch in each animal in a TEE right after euthanizing the animal (images A, B and C). The white arrow heads indicate where the patch is located. View of each explanted aorta containing the patch marked with white discontinuous circles (images D, E and F).

While all patches remained attached for the whole flow test, there was a significant difference between the surfaces of the patches at 90 days compared to the ones stopped at 30 days. In the case of the 90 days, the patch surface was shinier, and the general color was closer to the aorta's. This could indicate an increased cellular coverage over time. Small accumulations of blood below the patch were observed in 30 days samples.

4.3.3.2.1   Histology analysis

Only the relevant microscopic findings are presented in this section. In this case, it was possible to obtain sections containing the patch attached to the artery for all the animals. Only one relevant results/animal is presented for each end point while the results presented in the subsequent tables contain a summary of all samples at each point.

Starting with the results at 30 days, the luminal layer of the patch was overall covered in all sections, but multifocally interrupted in some cases. Figure 100 shows a histological section of animal 01160, where the patch was completely covered by fibrous tissue. The formation of fibrous tissue was thicker on both edges in this section. A fibrous layer was also multifocally present between the patch and the intimal surface of the aorta, indicating consistent integration. Moreover, this fibrous tissue covering the patch started to be reendothelialized in some parts, indicating tissue growth and possible future maturation.
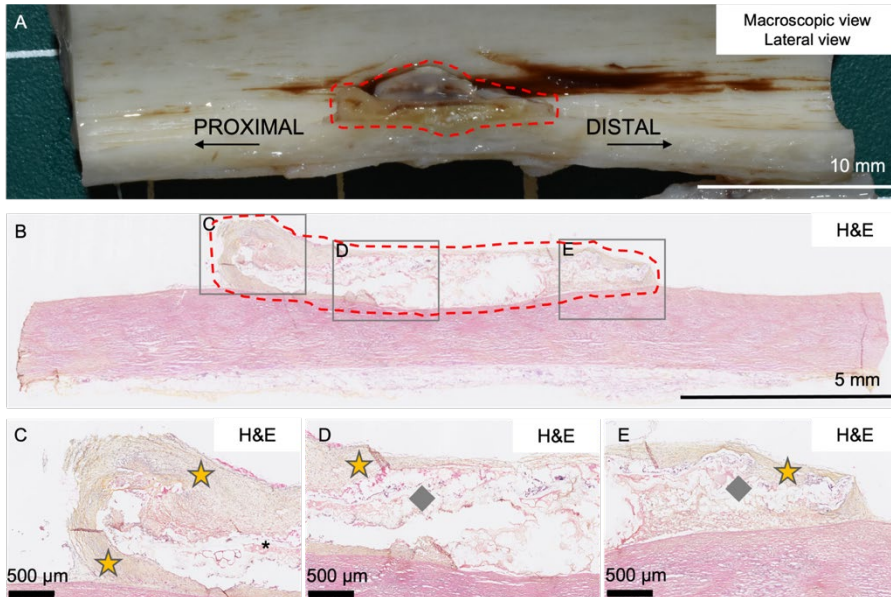
Figure 100. Histological analysis of a one-month animal (#01160). Image A shows one side of the aorta cut from proximal to distal containing the patch (marked in red). Image B shows the corresponding histological section of image A. Images C, D and E correspond to a magnification of section B. All slides were stained with H&E. Formation of new fibrous tissue is marked with a yellow star, fibrin deposits are marked with an asterisk and the presence of the patch is marked with a grey square.

There was some inflammatory response indicated by the presence of mononuclear inflammatory cells (lymphocytes and macrophages) multifocally within the fibrous tissue in some cases (60% sections). Some foreign body-type multinucleated giant cells were observed at the surface of the luminal layer of the patch material tissue (60% sections) (Figure 101). Overall, inflammation score was considered minimal when compared with other parameters such as reendothelialization (Figure 102). All scores are presented together with the data of the 90 days test.
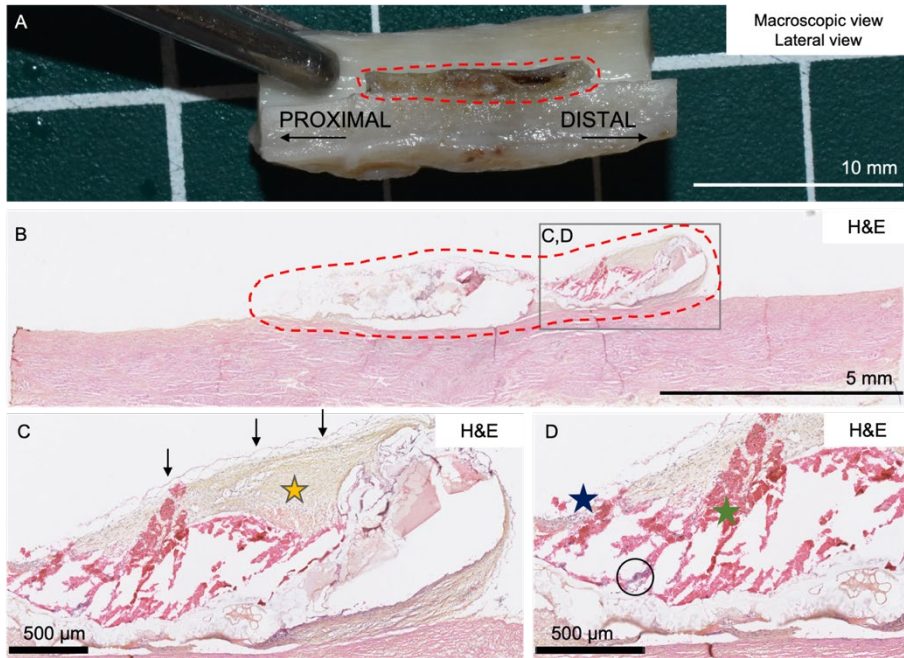
Figure 101. Histological analysis of a one-month animal (#02071). Image A shows one side of the aorta cut from proximal to distal containing the patch (marked in red). Image B shows the corresponding histological section of image A. Images C and D correspond to a magnification of section B. All slides were stained with H&E. Formation of new fibrous tissue is marked with a yellow star. Reendothelialization is marked with black arrows. Mononuclear inflammatory cells are marked with a blue star and multinucleated giant cells are marked with a circle. Red blood cells are marked with a green star.

At 90 days, the patch was present in all the sections analyzed except for one section where the patch material was missing due to a technical error during processing. The luminal layer of the patches was overall almost complete and onloy occasionally multifocally interrupted. Minimal fibrin deposits were observed multifocally within the patch in 40% of the sections as well as minimal neutrophils (20%, 1/5 sections).

A mild fibrous tissue, completely reendothelialized, covered the luminal surface of the patch in both cranial and caudal edges, and was thicker on both lateral edges. A fibrous tissue layer was also multifocally present between the patch and the intimal surface of the aorta except for areas where the patch was apposed on the intima. The fibrous tissue slightly extended along the intimal surface of the aorta on both edges of the patch.
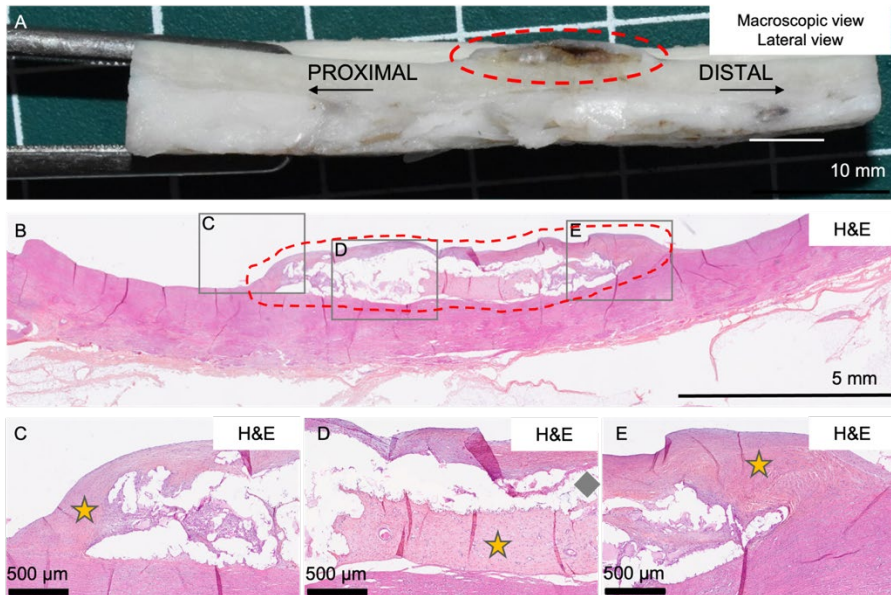
Figure 102. Histological analysis of a three-month animal (#02335). Image A shows one side of the aorta cut from proximal to distal containing the patch (marked in red). Image B shows the corresponding histological section of image A. Images C, D and E correspond to a magnification of section B. All slides were stained with H&E. Formation of new fibrous tissue is marked with a yellow star, fibrin deposits are marked with an asterisk and the presence of the patch is marked with a grey square.

Overall, minimal mononuclear inflammatory cells (mostly lymphocytes and macrophages) were noted multifocally within the fibrous tissue in all sections. Minimal foreign body-type multinucleated giant lined surface of the luminal layer of patch material in all sections.
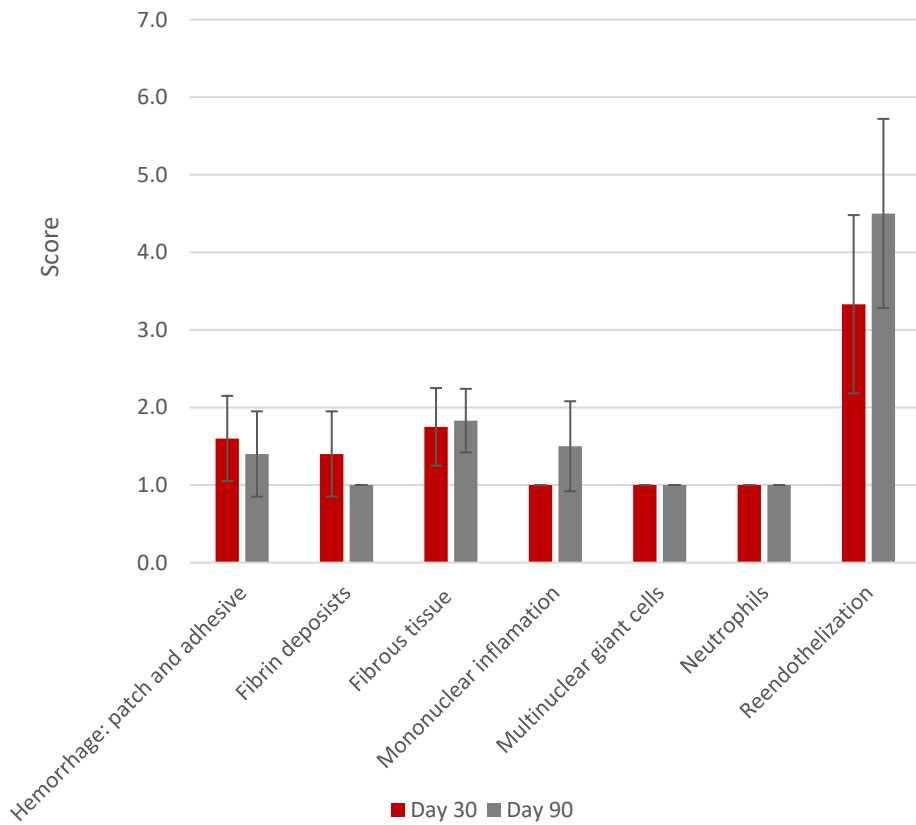
Figure 103. Summary of microscopic changes at the implantation site at day 30 or 90 respectively

Local tolerance of the patch and adhesive was considered excellent. Only minimal lymphocytes and macrophages were noted within the fibrous tissue in most sections. Minimal foreign body-type multinucleated giant cells were also observed at the surface of the luminal layer of patch material at both timepoints. These cells were rare at Day 30 then tend to line the patch material at Day 90. In addition, minimal foamy macrophages containing small vacuoles were noted within the patch around irregular, honeycomb-shaped areas that likely corresponded to remnants of the abluminal layer of the patch in one section (02335). These microscopic features were interpreted as signs of patch bioresorption.

In conclusion, microscopic findings correlated with macroscopic observations at necropsy and at trimming. These changes were consistent with very good tissue integration, fibrous tissue maturation, excellent local tolerance, null thrombogenicity initial signs of bioresorption at 3 months.

Table 10. Chronic group. Summary of the tests.

Animal number	Surgery type	Flow duration	Follow-up results	Explantation results + Histopathology results
Animal 1 (Ovine 19002)	Open surgery, CPB	1 month	Patch visible but partially detached. No visible thrombus. Normal flow around.	Patch present but curled up. Minimal thrombosis Presence of minimal multifocal red blood cells and fibrin deposits. Minimal inflammation response. Mild reendothelialization of the fibrous tissue
Animal 2 (Ovine 02071)			Patch visible and perpendicular to the aortic wall. No visible thrombus. Normal flow around.	Patch well in place, no detachment. Presence of minimal multifocal red blood cells and fibrin deposits. Minimal inflammation response. Mild reendothelialization of the fibrous tissue
Animal 3 (Ovine 01160)			Patch present, but thin with the edges thicker. Half of the patch detached No abnormal moving or deformation with the flow. No visible thrombus.	Patch present but shrunk on both sides. Detached on left and right side. Presence of minimal multifocal red blood cells and fibrin deposits. Minimal inflammation response. Mild reendothelialization of the fibrous tissue
Animal 4 (Ovine 01172)	Open surgery, CPB	3 months	Patch well apposed. No deformation. Round shape and no detachment. No visible thrombus. Normal flow around.	Patch present and still in place. No detachment under physiological flow conditions. Presence of minimal multifocal red blood cells and fibrin deposits. Minimal inflammation response. Complete reendothelialization of the fibrous tissue. Maturation of the fibrous tissue.
Animal 5 (Ovine 02335)			Patch visible and having circular shape. No visible thrombus. Normal flow around.	
Animal 6 (Ovine 11404)			Patch in place. Well apposed. Circular shape in longitudinal view. Patch was thin but slightly thicker on the ventral aspect No visible thrombus. Normal flow around.	

4.4   Concluding remarks

We have demonstrated that the patch designed in this thesis can be implanted in two *in vivo* models, pig and ovine. The patch is compliant with the natural motion of the aorta and presents excellent biocompatibility. To demonstrate so, an *ex vivo* implantation model was needed, and after several attempts, the model was successfully designed and tested. This model was used to optimize all the implantation parameters that were finally used *in vivo*.

The surgical procedure chosen to perform the *in vivo* tests was open surgery. The main reason was to study the biomechanical integration of the patch (and the adhesive) with the aorta without considering other parameters that may affect the results (such as the endovascular catheter). By these means, the first *in vivo* tests performed were acute tests and both animal models were tested at this point. Those tests were used to evaluate the early tissue response and adhesion strength of the system. For that, animals did not have to recover from surgery since the flow test performed to the attached patches was only a 30-minute test. Very promising results were obtained with both models, with minimal inflammatory response as confirmed by histological analysis. These tests helped deciding the final animal model to be the ovine model.

Testing continued with subacute (1 day) and sub-chronic (7 days) to better evaluate the patch mechanical integration. TEE was implemented as patch adhesion confirmation technique after implantation, during follow-ups technique and right before explantation. Patch visualization was optimal at all timepoints, confirming that the patch accompanies the artery in every distention and recoil cycle. Adhesion was confirmed at necropsy, and the tissue reaction and biological integration was evaluated using histological analysis. This analysis confirmed that the patch was still in place in all cases with a local tolerance of it excellent at the implantation site. There were minimal multifocal fibrin deposits observed on the luminal aspect of the patch

and minimal to moderate multifocal reendothelialization of the intima. This test was the first evidence of an encouraging cell response over the patch, but longer tests were scheduled to study the tissue response over time.

Chronic experiments were performed at 1 and 3 months. The mechanical integration was very good, and patches remain attached in all cases. Histology confirmed that the patch generated very low inflammatory response at both timepoints. At 30 days, the patch was covered by fibrous tissue in most of the cases. This fibrous tissue matured over 90 days with connective tissue loose and disorganized at 30 days but compact and oriented in parallel to the aortic wall at 90. Reendothelialization was excellent, which was critical to avoid thrombosis.

Overall, the main objective of this chapter and of the thesis was accomplished with very promising results.

5 MATERIALS AND METHODS

5.1 Patch manufacture

5.1.1 Materials and reagents

Table 11. List of materials and reagents for patch manufacturing

Material or reagent	Product code	Supplier
Chloroform	C2432	Sigma Aldrich
Dimethyl formamide (DMF)	227056	Sigma Aldrich
Polycaprolactone (PCL) 80,000 Mn	440744	Sigma Aldrich
Squalene (Sq)	S3626	Sigma Aldrich

5.1.2 Equipment

Table 12. List of instruments for patch manufacturing and characterization

Instruments	Product code	Supplier
Dynamic Mechanical Analyzer (DMA)	Q800	TA Instruments
Electronic digital caliper	C041/15	Fervi
Electrospinning machine	Fluidnatek® LE-10	Bioinicia
Luer lock plastic syringe	4617053V	Omnifix
RH/ Temperature data logger	EL-USB-2_LCD	EL
Magnetic stirrer – Agimatic N	7000243	J. P. Selecta
Rotational rheometer	AR550	TA Instruments
Scanning Electron Microscope	Jeol JSM-5310 scanning microscope	Electrometric methods lab

5.1.3 Solution preparation

PCL pellets were dissolved in either chloroform or a mixture of chloroform and DMF solution in a glass bottle with ISO screw. The final concentration of PCL was 12% in a chloroform and DMF solution (80:20). The solution was mixed with a magnetic stirrer overnight at room temperature with the bottle closed to avoid solution evaporation. The shear viscosity of the polymeric solution was measured using a rotational rheometer (AR2000ex) equipped with 40 mm cone and plate fixtures.

5.1.4   Electrospinning method

The electrospinning apparatus (Fluidnatek^{TM}, LE-10) was set up horizontally. Notice that these were the final conditions stablished to obtain homogeneous PCL fibers. Polymer solution was loaded in a 5 mL Luer lock plastic syringe and it was pumped through the syringe needle of 0.8 mm diameter. The syringe was placed on a syringe pump system and the mixture was propelled at a volumetric flow of 2000 µL/h. The syringe pump was placed horizontally, 18.0 cm away from the collector. A voltage potential from 16.0 to 20.0 kV was applied between the syringe pump and the collector. The collector used was the drum of 10 cm in diameter. The mixture was deposited on the collector for 2 hours. For the first hour the drum was maintained static and for the second hour it was rotated at a 1000 rpm speed (clockwise direction). The patch was afterwards air dried for approximately 1 hour.

5.1.5   Dynamic Mechanical Analysis (DMA)

The mechanical properties of samples prepared via electrospinning were analyzed using DMA, more precisely with uniaxial tension tests. The main objective of performing these tests was to compare the values obtained for the patches with the native tissue of the aorta. The arterial wall is a three-dimensional body. But to simplify the mechanical testing, it would be considered as two-dimensional, for example, as a membrane. Moreover, the circumferential, longitudinal and shear stresses will be considered as uniform across the wall. The uniaxial test can be performed in both the longitudinal and circumferential direction (see section 1.2).

However, the uniaxial tensile method only obtains the mechanical behavior in one direction at a time. Therefore, obtaining a single value of Young's modulus. Besides this method is not the most accurate for defining the aorta's mechanical properties, since blood vessels are characterized by a non-linear elastic behavior, it is the most widely used method and was the method of choice for this thesis.

5.1.5.1   Sample preparation

The electrospun sheets were cut into long, thin, rectangular (about 30 mm length and 8 mm width) strips. For the samples having two different layers of material, the strips were cut into two different directions: parallel to the aligned fibers or perpendicular to the aligned fibers. The width and thickness were measured at three locations along the length of each specimen using a dual caliper, averaged, and recorded.

Uniaxial tension tests

The tension test performed was a strain-stress test carried out at DMA TA Instruments. The sequence used to perform the tests was:

- Mode: Strain rate
- Test: Strain Sweep
- Tension: Film (Clamp)
- Sample shape: rectangular (l,w,t)

- Frequency: 1.00 Hz
- Pre-load force: 0.0010 N
- Initial strain: 0.90%
- Initial displacement: 10.00 μm
- Strain ramp: 5.00%/min to 30.00%

5.1.5.2   Viscoelastic tests

The viscoelastic test performed was carried out at DMA TA Instruments. The sequence used to perform the tests was:

- Mode: Muli-strain
- Test: Strain Sweep
- Tension: Film (Clamp)
- Sample shape: rectangular (l,w,t)
- Frequency: 1.00 Hz
- Pre-load force: 0.010 N
- Force track: 125%
- Soak time: 5.00 min
- Number of sweeps: 1
- Amplitude: (log) 5.00 to 200.00 μm

5.1.6   Measuring the arterial elasticity: The uniaxial tensile test

At the no-load condition, the length of the specimen is L_0, the width W_0, and the thickness H_0. Once the load is applied, the length becomes L and the stretch ratio can be obtained as the ratio of L to the initial length L_0. The load divided by the initial cross-sectional area A_0 yields the tensile stress T (Equation 1).

$$T = \frac{load}{A_0}$$

Equation 1. Tensile stress (T)

The tensile stresses at a physiological range are greater than 20 kPa and less than about 60 kPa[19]. In this range, the aorta is behaving as a linear elastic material and therefore, it obeys the Hooke's Law, and the elastic modulus can be considered as constant.
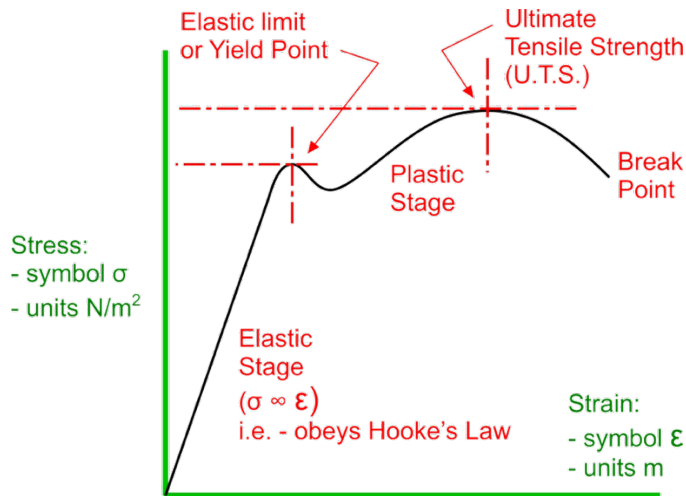
A wide amount of studies has been focused on the mechanical behavior of the arterial wall considering the regional and directional variability[146,147]. In these studies, the aorta is separated into four regions: anterior, posterior, lateral-right and lateral-left. Moreover, all the regions have been tested in both directions: longitudinal and circumferential. The data concluded the circumferential direction to be stiffer than the longitudinal direction at physiological and high stresses.

However, the uniaxial tensile method only obtains the mechanical behavior of arteries in one direction at a time. Therefore, obtaining a single value of Young's modulus. Besides this method is not the most accurate for defining the aorta's mechanical properties, since blood vessels are characterized by a non-linear elastic behavior, it is the most widely used method and has been the method of choice for this thesis.

5.1.7 Scanning Electron Microscopy (SEM)

The SEM was used to characterize the microstructure of the electrospun samples. To do so, samples were cut in small square pieces of less than 10 mm. All samples were dried, and gold sputtered before undergoing the SEM analysis.

Morphometric analysis of the electrospun nanofibers was quantitatively performed processing SEM images by ImageJ software. This is an image processing program designed for scientific multidimensional images and based on plugin series Diameter J Segment Diameter J 1-018.

Diameter J Segment plugin algorithm works by segmenting SEM image and allows selection of images. Selected segmented image/or images to best represent a sample should have the following characteristics: absence of partial fibers, fiber intersection shouldn't contain black spots/hole. When two or more images of the sample are very similar, best choice should be the one containing highest number of fibers. Super Pixel is the plugin that calculate mean fibers' diameter, using a super pixel determination (the scale length set was 202 pixels for 1 cm). Mean fibers' diameter was determined by Histogram Mean, fitting a Gaussian Curve to the radius data and finding the curves mean value. Histogram SD delineates the standard deviation of the Gaussian fit of the radius histogram. Histogram Mode and Histogram Median determine respectively the most occurring fiber diameter in the histogram and the middle fiber diameter. Histogram Min. Diam. and Histogram Max. Diam defines the smallest and the largest diameter measured. Histogram Integrated Density calculates the product of length of the fibers and the average radius, then Histogram Raw Integrated Density determines the sum of the radii at all pixels in the image or selection. Diameter Skewness measures the third order moment of the mean; Diameter Kurtosis the fourth. All analyzed data were then plotted by using Microsoft Excel.

The values of orientation were obtained analyzing SEM images with ImageJ and plugin Orientation J software, that analyzed the degree of fiber orientation distribution from −90° to +90°, of each SEM image using Fast Fourier transform (0° angle corresponded to the horizontal orientation parallel to mandrel axis and increased counter-clockwise). Analysis was performed on 6 SEM images for each electrospun matrix sample. Fiber alignment is expressed as frequency %, calculated by taking how many times same + 90 ° fiber orientation repeats during analysis of the same area of sample divided by the total number of total counted fibers in the area and multiplied by 100. The greater frequency % value the more oriented the electrospun fibers are.

5.1.8   Simplex optimization

The Simplex optimization was developed back in 1962 by *Spendley et al.*[148] and it continues to be commonly used in the present since it is among the most efficient optimization procedures, very useful in the development of analytical methods and successfully applied chemical analyses[149]. It is easy, does not require the use of complex mathematics and statistical tools and, most important, allows the optimization of various studied factors at the same time[150].

Simplex optimization is performed by the displacement of a geometric figure with k + 1 vertexes in an experimental field toward an optimal region, where k equals the number of variables in a k-dimensional domain (Figure 106). Therefore, this method requires only one additional experiment regardless of the number of factors being varied. The most important part is that this procedure reduces drastically the number of experiments required to reach the optimum[149].
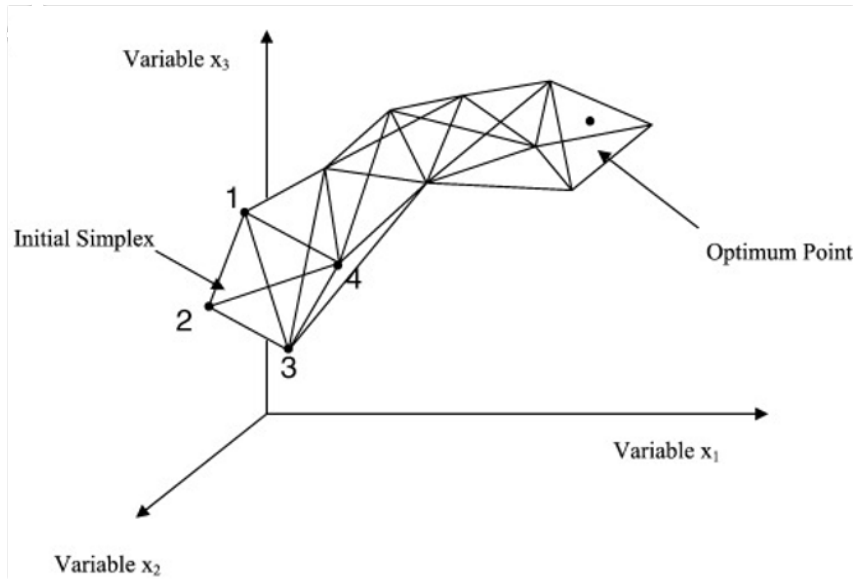
5.2 Cell culture

5.2.1 Materials and reagents

Table 13. List of materials and reagents for *in vitro* tests

Material or reagent	Product code	Supplier
Dimethyl sulfoxide (DMSO) sterile	D2650-5x5mL	Sigma
Endothelial Cell Basal Medium 2	C-22211	Promo Cell
Supplement Pack Endothelial Cell Growth Medium 2	C-39211	Promo Cell
Fetal Bovine Serum (FBS)	35-079-CV	Corning
Human Aortic Endothelial Cells (HAoEC)	C-12271	PromoCell
Phosphate Buffered Saline (PBS)	70011-036	Gibco
Penicilin (10000 u/mL)/Streptamycin 10000 µg/mL)	15140-122	Gibco
Trypsin/EDTA 1x	25300-062	Gibco

Table 14. List of peptides and proteins for *in vitro* tests

Material or reagent	Product code	Supplier
Fibronectin from bovine plasma (Fn)	F1141	Sigma-Aldrich
Laminin 411	LN411	BioLamina
Laminin 511	LN511	BioLamina
RGD (Tyr-Ile-Gly-Ser-Arg)	ab141093	Abcam
VE-Cadherin	ab27462	Abcam
VGVAPG	-	Synthesized by LipoPharm
YIGSR (laminin derived peptide) Tyr-Ile-Gly-Ser-Arg	ab141093	Abcam

Table 15. List of endothelial cell culture medium

Human Aortic Endothelial Cells (HAoEC)	Final Volume
Endothelial Cell Basal Medium 2	500 mL
FBS 5%	25 mL
P/S 1%	5 mL
Supplement Pack Endothelial Cell Growth Medium 2	Added

Table 16. List of materials and reagents for immunocytochemistry

Material or reagent	Product code	Supplier
Albumin from bovine serum (BSA)	A9647	Sigma Aldrich
DAPI (4',6-diamidino-2-phenylindole)	D1306	Invitrogen
Glycine	GE17-1323-01	Sigma Aldrich
PFA (paraformaldehyde)	P6148	Sigma Aldrich
Rhodamine Phalloidin	R415	Invitrogen
Triton-X-100	T8787	Sigma Aldrich

5.2.2   Equipment

Table 17. List of instruments for cell culture experiments

Instrument	Product code	Supplier
Adhesive spray Remount	-	3M
Bio II Advance Plus	525152	Telstar

Double cell Improved Neubauer ruled chamber	719505	Bürker-Türk
ESCO Cell Culture Incubator	CCL-170T-8-P	Esco
Centrifuge	2-16KL	Sigma
Primovert	415510-1100-000	Zeiss

5.2.3 Cell growth

1 mL aliquots of cryopreserved cells (-150 °C, liquid nitrogen cryofreezer) were thawed in a 37 °C water bath and added to T75 plates containing 12 mL preheated complete adequate medium. Each 1 mL aliquot had a concentration of approximately 1 M cells/mL and were preserved in a medium containing 60% complete medium, 30% FCS and 10% DMSO. Plates were incubated in a 37 °C, 5% CO_2 cell culture incubator. After 3 hours the attachment of cells was visually confirmed under the IM and medium was replaced with 13 mL of fresh medium to avoid toxic effects of remaining DMSO. Medium changes were performed by aspirating the used medium with the aid of a sterile glass Pasteur pipette connected to a vacuum. After removing DMSO, medium was changed every 48 h until cells reached approximately 90% confluence.

5.2.4 Trypsinization

When cells had reached around 90% confluence, they were detached from the T75 flask by trypsinization. Cell culture medium was aspirated, and cells were washed with 13 mL sterile PBS. PBS was then aspirated and 3.5 mL trypsin-EDTA solution were added. The plate was incubated in the cell culture incubator (37 °C) for 4 minutes to allow for trypsin to act. Flasks were observed under the microscope to verify detachment, and 9.5 mL STOP medium (any leftover cell culture medium containing FBS, which naturally contains trypsin inhibitors) were added. Liquid in the flask was ejected onto the surface where cells had been adhered using a serological 10 mL pipette, to recover as many

cells as possible at the bottom of the flask. The cell suspension was placed in a Falcon® tube, from which a 10 μL sample was taken for cell counting in a Neubauer chamber. The cell suspension was centrifuged for 5 minutes at 1500 rpm to obtain a cell pellet. The pellet was resuspended in the appropriate volume of complete medium for seeding in new flasks or cell tubes or cryopreserving in case of surplus.

5.2.5 Cryopreservation

Cells were cryopreserved by resuspending them at a concentration of 1 M cells/mL in a combination of 60% complete cell culture medium, 30% FCS and 10% DMSO. DMSO was added last and the suspension was quickly aliquoted in 1 mL cryopreservation vials. Vials were immediately transferred to a cryobox and frozen at -80 °C in a liquid nitrogen freezer. After 24 hours, vials were transferred to -150 °C freezer.

5.2.6 Cell culture for adhesion assays

Before starting the experiment, patches are cut of approximately the same shape and size as the silicone plugs, normally 10 mm diameter discs. The number of required patches will depend on the experimental design. Each condition should have 3 replicates/patches. For the sectioning process, use a scalpel blade and bare (clean) hands, as gloves produce electrostatic energy and patch might float off. Try to identify the aligned and random fibers sides of the patch and store the patches in a sterile plate.

The next step consists of stick the patches in cell culture plastic wells. All the steps are conducted under sterile conditions. Protect sterile hood (metal tray and glass) from the adhesive (spray) by covering surfaces with plastic. Apply adhesive spray (Remount 3M) homogenously for about 1-2 second at 15-20 cm distance on the opposite site of the patch to test (e.g. when testing endothelial cells, apply spray in the side with random fibers). During the spraying use the plastic-protected area of the sterile hood. Stick the adhesive

side of the patch to the well using the silicone plugs to gently lay the patch down. Do not press strongly as the microstructure of the patch could be affected. Keep forceps manipulation to a minimum. Wash patches with cell culture media (2 mL STOP media/well) 3x for 5 min each in the orbital shaker to remove excess of adhesive and coat the well with proteins from the serum/media. Store the stuck patches in the plate or continue with next steps.

The last step consists of adding a surface treatment onto the patches before cell seeding. This procedure starts by setting up the plasma device inside the cell culture hood. Treat one patch with plasma for 1 min using 1 ½ power. Hight of the plasma device might need to be adjusted over time, as the plasma generator heats up and it could burn the patches. Then, add 30 µL of the protein solution, PBS or no liquid, apply and extend the protein solution throughout the surface of the patch. Repeat this process with the rest of the patches so all patches have a constant duration between plasma and protein treatment. Incubate for 2 h at 37 °C. Aspirate excess of protein solution minimizing contact with the patch. Seed 300.000 cells on top of the patch and incubate at 37 °C for 48 h under steady conditions (avoid moving the plate, movements in the incubator, etc…). Refresh media every 2-3 days for the duration of the experiment. Fix cells in fresh paraformaldehyde (PFA) at 4% for 30 min at RT and wash 2x with PBS for 5 min each. Store in PBS or continue with immunocytochemistry.

5.2.7 Cell culture for migration assays

The procedure for migration assays is the same as per adhesion tests. The only difference appears before seeding the cells, where patches should be covered with the silicone plugs of the exact same shape. Then 300.000 cells are seeded in the remaining space of the well, avoiding movement. The silicone plugs are removed after 24 hours, and the media is refreshed every 2-3 days for the duration of the experiment.

5.2.8   Immunocytochemistry

For 6-well plates, the cell culture medium was aspirated, and cells were washed twice with cold PBS. Then, cells were fixed in 4% PFA for 30 minutes, and washed twice in PBS for 5 minutes each wash. Aldehydes were quenched with 0.2 M glycine in PBS for 10 minutes and washed twice for 5 minutes in PBS. Cellular membranes were permeabilized in PBS-Triton (PBS with 0.2% Triton-X) for 10 minutes and washed twice for 5 minutes in PBS. All previously mentioned steps were at room temperature. Finally, incubate with DAPI and Phalloidin for 2 hours at RT in the dark (DAPI 1:1000 and Phalloidin 1:30, 500 µL per well in 6-well-plate). After incubation in the dark, cells were washed twice in PBS for 10 minutes, and preserved in PBS for microscopic analysis.

5.3   *Ex vivo* tests

5.3.1   Materials and reagents

Table 18. List of materials and reagents for *ex vivo* tests

Material or reagent	Product code	Supplier
Aorta	Pig aorta	Gustus oliver
Deployer	-	Manufactured in house
Dextran from Leuconostoc mesenteroides	D5376	Sigma Aldrich
Fetal Bovine Serum (FBS)	35-079-CV	Corning
Hexyl cyanoacrylate (HCA)	-	Manufactured in house
Patch	-	Manufactured in house or by TECL
Phosphate Buffered Saline (PBS)	70011-036	Gibco
Polyvinyl alcohol sutures (PVA)	U2703	Coats aquamelt

5.3.2　Equipment

Table 19. List of instruments for *ex vivo* tests

Instrument	Product code	Supplier
Controlled Force Deployer (CFD)	-	Manufactured in house
Die cutting punch	X000VECYBL	Amazon
Dual phase control – Pump	MA1 55-3305	Harvard Apparatus
Heat regulator	X000ZZ9IAV	VPCOK
Methacrylate system box	-	Manufactured in house
Microman E M10 E, 1-10 µL micropipette	FD10001	Gilson
Pressure Applying Machine (PAM)	-	Manufactured in house
Surgical blade	0201	Swann-Morton – ST10
Tank	-	Aortyx
Tank plugs	2 237000 039640	Servei Estació
Tank input filter	1020-11/4	Servei Estació

5.3.3　*Ex vivo* protocol

Before starting the *ex vivo* test, an aorta was thawed in a 37.5 ºC water tank. Once thawed, the aorta was placed on an aluminum foil covered tray and the aortic arch was excised, leaving only the longitudinal section of the aorta. Then, both ends of the aorta were held using a methacrylate system box, with this system the aorta was suspended without touching any surface recreating better the *in vivo* situation. After that, an incision of about 5 to 10 cm was made (depending on the specimen geometry and size) to expose the aorta's inner luminal space. The incision was performed on top of the smooth external surface, which did not present any arterial ostia.
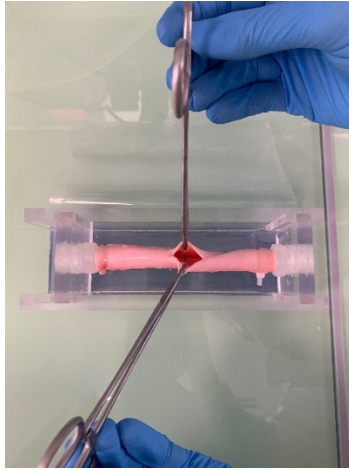
Figure 107. Methacrylate box with suspended aorta

The patch was then subjected on top of the nitinol deployer by using 4 PVA single knot stitches and with the aligned layer facing the deployer. Then, the HCA was applied on the patch by using the micropipette. Directly after adding the adhesive to the system, the patch was introduced into the inner aorta´s wall and pressed against the artery for 1 minute (in presence or absence of FBS at 37.5 ºC depending on the test) using the Pressure Applying Machine or the Controlled Force Deployer. Then, hot water (37.5 ºC) was poured on the aorta to dissolve the PVA knots for 5 minutes. After the dissolving time, the deployer was softly pulled to evaluate if all the stitches were dissolved. Once ensured, the deployer was released and the patch was visually and manually inspected to secure patch attachment to the artery. After visual approval, the aorta was manually sutured.
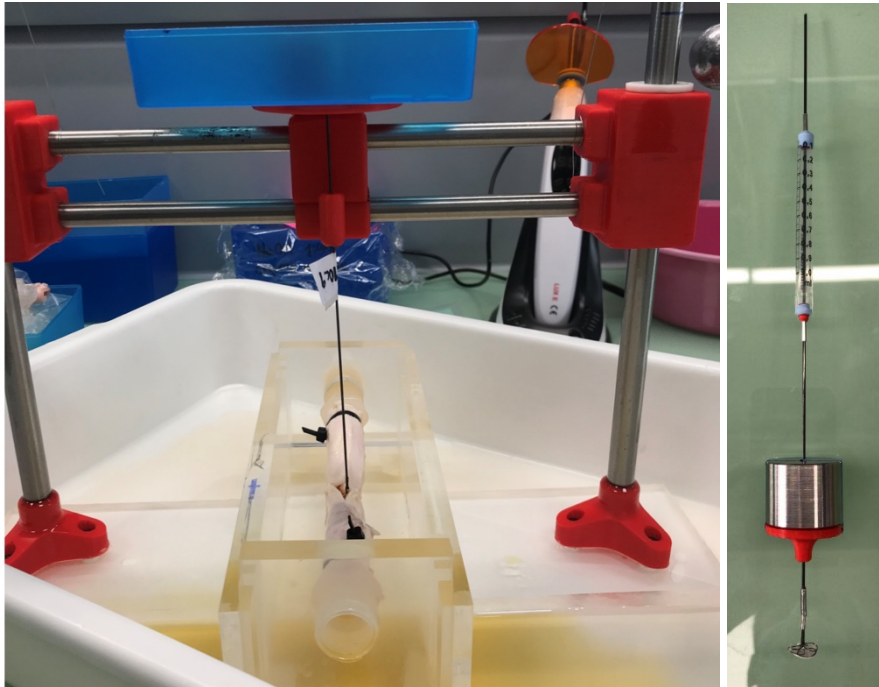
Figure 108: On the left, the Pressure Applying Machine (PAM). On the right, the Controlled Force Deployer (CFD)

Finally, and depending on the test performed the methacrylate box with the suspended and sutured aorta was connected to a continuous flow system. The system consists of a liquid tank with inlet and exit tubes, a Dual phase control pump and a thermometer-regulated heat source. The system was filled with 8 liters of fluid containing water and 20 g/L of dextran. A continuous-flow test was maintained for 5, 10 or 30 minutes (depending on the test performed) and, once the continuous-flow test ended, the aorta´s incision was opened, and the patch condition was evaluated.

5.4 *In vivo* tests

5.4.1 Materials and reagents

Table 20. List of materials and reagents for *in vivo* tests

Material or reagent	Product code	Supplier
Controlled Force Deployer (CFD)	-	Manufactured in house
Deployer	-	Manufactured in house
Hexyl cyanoacrylate (HCA)	-	Manufactured in house
Patch	-	Manufactured in house or by TECL
Polyvinyl alcohol sutures (PVA)	U2703	Coats aquamelt

5.4.2 Equipment

All the surgical equipment was provided by the animal facilities.

5.4.3 Implantation procedure/protocol acute tests

An open surgical approach was the treatment of choice to test the patch integrity during a 30 min blood flow test. The veterinaries and the anesthesiologist prepared the animal and performed the surgery, and the Aortyx team proceeded with the implantation process. The procedure began by anesthetizing the animal. The animal was placed in right recumbency to perform a thoracotomy at the 5-6 intercostal level. During surgery, the descending aorta was exposed after the arch. Before clamping the artery, 1 mg/Kg of Heparin were injected. After 5 minutes, the aorta was horizontally cross clamped cranially and caudally, the time was recorded to evaluate the procedure's duration. Then, the blood inside the artery was collected using a syringe equipped with a needle and stored at RT for later use. Once the aorta was emptied, an incision of about 3 cm was made. Two sutures were placed in each site of the incision to facilitate the opening of the artery when implanting the patch.
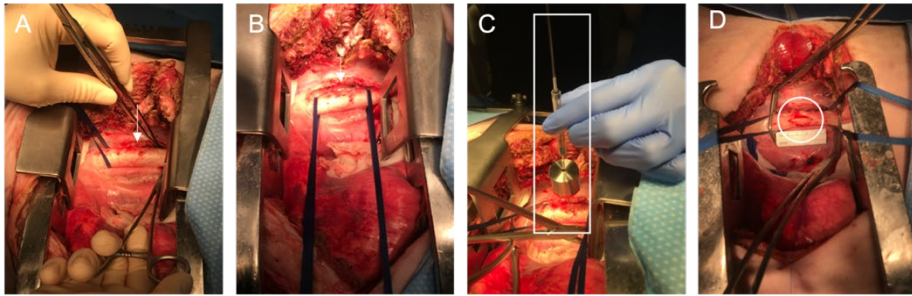
Figure 109. Aorta preparation for implantation performed with the ram model. Image A and B show the process of accessing and exposing the artery, the white arrow remarks the aorta. Image C shows the CFD apposition before clamping and opening the artery, marked with a white rectangle. Image D shows the aorta cross-clamped with the incision of 3 cm marked with a white circle.

The patch implantation process began at this point. Once the aorta was ready, 24 µL of adhesive were distributed over the surface of the patch performing a cross in the inner part and a circle in all the perimeter of the 10 mm patch using the Microman micropipette (patch was already attached to the deployer with 4 PVA square knot stitches). Next, the patch was placed in a straight single motion. The system was hold in place for 1 min and the pressure applied by the deployer was maintained homogeneous to 1 N using a weight of 100 g.
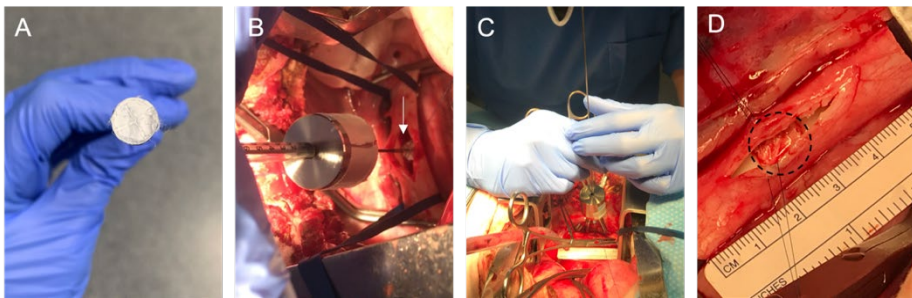
Figure 110. Implantation procedure performed with the ram model. Image A shows how the adhesive was distributed over the patch. Image B and C show the implantation process, white arrow indicate the presence of the patch below the deployer. Image D shows the patch attached to the artery before suturing the incision.

This constant force (1 N) was continuously applied for 5 additional minutes to completely dissolve the PVA stitches by applying pre-warmed (37 °C) saline solution. Then, the deployer was released and the patch adhesion was examined by gently touching the patch with tweezers. Once the complete adhesion of the patch to the aorta was confirmed, the implantation process ended, and the incision was smoothly sutured by the veterinaries. The aortic artery was carefully unclamped, and blood flow was restored, which was maintained for 30 min with the anesthetized animal. After 30 min time, another dose of heparin was administrated to the animal and then, the animal was euthanized. The part of the aorta that contains the patch was excised trying not to compromise the artery's integrity. Said part was preserved in PFA to carry out the subsequent histopathological analysis.

5.4.4 Implantation procedure/protocol sub-chronic and chronic tests

The surgical procedure to prepare the animals was the same as per the acute tests. The main difference was that animals must undergo CPB before clamping the artery to assure a proper recovery. When undergoing CPB procedure, the whole flow bypass setup was assembled and started after exposing the artery, but prior to clamping the aorta. To do so, first the CPB tubes and cannulas were prepared. After ensuring there was enough length for the tubing to reach the femoral area, the long extension tubing was mounted on the femoral artery cannula. A test suction was then performed. After that, heparin was injected. Then, arterial cannulation was performed on the carotid and femoral arteries, followed by venal cannulation of the jugular vein. Finally, normothermic CPB was started. After the CPB started, the same implantation procedure previously described was performed. Once the artery was declamped, the proper attachment of the patch via vascular echography was ensured. Then, CPB flow was stopped, and all the arterial and venal

accesses were respectively closed and sutured. Next figure exemplifies the perfusion setup when the specimen was under CPB conditions.
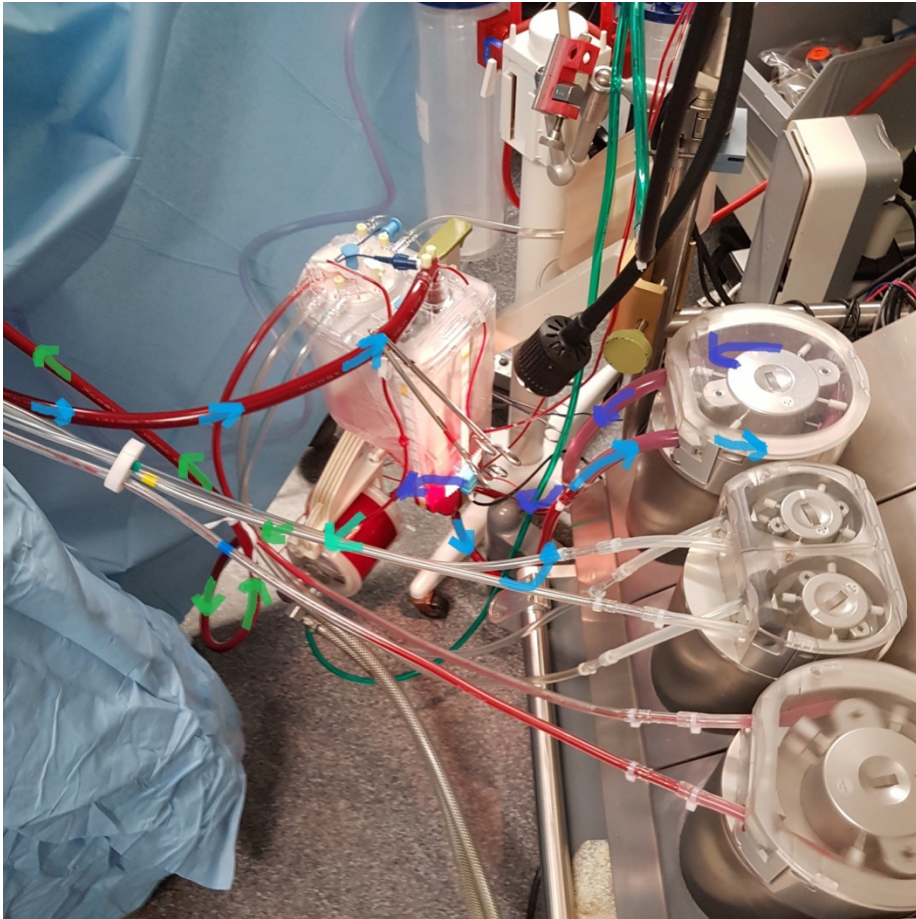
Figure 111. CPB setup. Flow lines indicate the different states of the perfused blood: light blue for deoxygenated blood coming from the ascending aorta; dark blue for deoxygenated blood after being pumped by the perfusion pump and before re-oxygenation; turquoise for blood being re-oxygenated; and light green for oxygenated blood returning to the animal.

6   CONCLUSIONS

A bioresorbable scaffold for use in a new endovascular treatment for aortic dissection patients has been developed in this thesis.

The scaffold has been designed with the shape of a circular patch, 150-200 μm in thickness and 10 mm (for animal studies) to 30 mm (for human application) in diameter. Electrospinning has been the technique chosen to achieve the mechanical properties targeted, similar to the aorta's, and to achieve attractive recellularization kinetics. A design using polycaprolactone as biomaterial and two distinctive layers, aligned in the luminal face and random in the abluminal, demonstrated enhanced fiber homogeneity and better reendothelialization *in vitro*. Endothelial cells enlarged their cytoskeleton to adapt to the fiber diameter, accelerating the colonization process. Different proteins and surface modification strategies were tested to improve cell adhesion. Despite excellent results with Fibronectin and Laminin 511, we decided to proceed without incorporating additives to facilitate the subsequent regulatory pathway. The manufacturing operational conditions were successfully transferred to two contract manufacturing organizations, but only one of them was chosen for *ex vivo* and *in vivo* testing.

An *ex vivo* system for patch testing has been put in place in collaboration with the research group. This system has minimized the need for animal assays, making this research more ethical and cost-effective. Pigs first, and rams later, were used for *in vivo* experiments, which consisted of four phases: acute, subacute, sub-chronic and chronic. Acute experiments were critical to properly establish the experimental conditions. Adhesion was strong and minimal inflammatory and thrombogenic responses were observed. Chronic experiments aimed at evaluating the mechanical and biological cohesion of the patch with the arterial wall over time. At one week, inflammatory and thrombogenic responses were negligible, but reendothelialization was minimal. At one month, inflammatory and thrombogenic responses remained low, and fibrous tissue was significant although immature, despite being

accompanied by significant reendothelialization. At three months, the fibrous tissue had matured, was aligned with the endogenous fibers of the aortic wall and was fully covered by endothelial cells. Inflammatory and thrombogenic responses remained consistently low, and the patch fibers started to show incipient resorption.

7 REFERENCES

1.   Hutchison, S. J. *Aortic Diseases: Clinical Diagnostic Imaging Atlas*. (2009).

2.   Erbel, R. *et al.* 2014 ESC guidelines on the diagnosis and treatment of aortic diseases. *Eur. Heart J.* **35**, 2873–2926 (2014).

3.   Bossone, E., Labounty, T. M. & Eagle, K. A. Acute aortic syndromes: Diagnosis and management, an update. *Eur. Heart J.* **39**, 739–749 (2018).

4.   College, O. S. *Anatomy and Physiology*. (2013).

5.   Criado, F. J. Aortic dissection A 250-Year Perspective. *Texas Hear. Institue J.* **38**, (2011).

6.   Kenneth S. Saladin. *Human Anatomy. Journal of Chemical Information and Modeling* vol. 53 (2017).

7.   Wagenseil, J. & Mecham, R. Vascular Extracellular Matrix and Arterial Mechanics. *Am. Physiol. Soc.* **89**, 957–989 (2010).

8.   Alberts B, Johnson A, L. J. E. Blood Vessels and Endothelial Cells New Endothelial Cells Are Generated by Simple Duplication of Existing. *Mol. Biol. Cell* **4126**, 24–28 (2002).

9.   Marieb, Elaine Nicpon; Mallatt, Jon; Wilhelm, P. B. *Human Anatomy*. (Benjamin-Cummings Pub Co).

10.   Yau, J. W., Teoh, H. & Verma, S. Endothelial cell control of thrombosis. *BMC Cardiovasc. Disord.* 1–11 (2015) doi:10.1186/s12872-015-0124-z.

11.   Van Hinsbergh, V. W. M. Endothelium - Role in regulation of coagulation and inflammation. *Semin. Immunopathol.* **34**, 93–106 (2012).

12.   Pober, J. S. & Sessa, W. C. Evolving functions of endothelial cells in inflammation. *Nat. Rev. Immunol.* **7**, 803–815 (2007).

13. Frantz, C., Stewart, K. M. & Weaver, V. M. The extracellular matrix at a glance. *J. Cell Sci.* **123**, 4195–4200 (2010).

14. D. Wu, Y. Shen, L. Russell, J. C. and S. L. Molecular Mechanisms of thoracic Aortic Dissection. *J Surg Res* **184 (2)**, 907–924 (2013).

15. Xu, J. & Shi, G. P. Vascular wall extracellular matrix proteins and vascular diseases. *Biochim. Biophys. Acta - Mol. Basis Dis.* **1842**, 2106–2119 (2014).

16. García-Herrera, C. M. *et al.* Mechanical behaviour and rupture of normal and pathological human ascending aortic wall. *Med. Biol. Eng. Comput.* **50**, 559–566 (2012).

17. Pejcic, S., Ali Hassan, S. M., Rival, D. E. & Bisleri, G. Characterizing the mechanical properties of the aortic wall. *Vessel Plus* **2019**, 1–12 (2019).

18. Belz, G. G. Elastic properties and Windkessel function of the human aorta. *Cardiovasc. Drugs Ther.* **9**, 73–83 (1995).

19. Fung, Y. C. *Biomechanics Mechanical properties of living tissues*. *Springer* (1993). doi:10.11239/jsmbe1963.24.213.

20. Burton, C. Relation of structure to function of the tissues of the wall of blood vessels. *Am. Physiol. Soc.* **34**, 619–642 (1954).

21. O'Rourke, M. Arterial stiffness, systolic blood pressure, and logical treatment of arterial hypertension. *Hypertension* **15**, 339–347 (1990).

22. MacEri, F., Marino, M. & Vairo, G. Age-dependent arterial mechanics via a multiscale elastic approach. *Int. J. Comput. Methods Eng. Sci. Mech.* **14**, 141–151 (2013).

23. Guo, X., Kono, Y., Mattrey, R. & Kassab, G. S. Morphometry and strain distribution of the C57BL/6 mouse aorta. *Am. J. Physiol. - Hear. Circ. Physiol.* **283**, 1829–1837 (2002).

24. Zhou, J. & Fung, Y. C. The degree of nonlinearity and anisotropy of blood vessel elasticity. *Proc. Natl. Acad. Sci. U. S. A.* **94**, 14255–14260 (1997).

25. WOLINSKY, H. & GLAGOV, S. Structural Basis for the Static Mechanical Properties of the Aortic. *Circ. Res.* **14**, 400–413 (1964).

26. C.G. Caro, T.J. Pedley, R. C. S. and W. A. S. *The Mechanics of the Circulation*. (Oxford University Press, 1978).

27. Chen, Q., Wang, Y. & Li, Z. Y. Re-examination of the mechanical anisotropy of porcine thoracic aorta by uniaxial tensile tests. *Biomed. Eng. Online* **15**, 493–506 (2016).

28. Yanagisawa, H. & Wagenseil, J. Elastic fibers and biomechanics of the aorta: Insights from mouse studies. *Matrix Biol.* **85**–**86**, 160–172 (2020).

29. Palombo, C. & Kozakova, M. Arterial stiffness, atherosclerosis and cardiovascular risk: Pathophysiologic mechanisms and emerging clinical indications. *Vascul. Pharmacol.* **77**, 1–7 (2016).

30. Oh, Y. S. Arterial stiffness and hypertension. *Clin. Hypertens.* (2018) doi:10.1161/HYPERTENSIONAHA.114.03617.

31. Nienaber, C. A. *et al.* Aortic dissection. *Nat. Publ. Gr.* **2**, 1–18 (2016).

32. Evangelista, A. *et al.* Insights from the international registry of acute aortic dissection: A 20-year experience of collaborative clinical research. *Circulation* **137**, 1846–1860 (2018).

33. Aune, D., Schlesinger, S., Norat, T. & Riboli, E. Tobacco smoking and the risk of abdominal aortic aneurysm: a systematic review and meta-analysis of prospective studies. *Sci. Rep.* **8**, 1–9 (2018).

34. Hoffjan, S. Genetic dissection of Marfan syndrome and related

connective tissue disorders: An update 2012. *Mol. Syndromol.* **3**, 47–58 (2012).

35.   Minhas, K. S. *et al.* Cardiovascular Manifestations and Complications of Loeys-Dietz Syndrome : CT and MR Imaging. (2005).

36.   Cury, M., Zeidan, F. & Lobato, A. C. Aortic disease in the young: Genetic aneurysm syndromes, connective tissue disorders, and familial aortic aneurysms and dissections. *Int. J. Vasc. Med.* **2013**, (2013).

37.   Bonser, R. S. *et al.* Evidence, lack of evidence, controversy, and debate in the provision and performance of the surgery of acute type A aortic dissection. *J. Am. Coll. Cardiol.* **58**, 2455–2474 (2011).

38.   Lemaire, S. A. & Russell, L. Epidemiology of thoracic aortic dissection. *Nat. Rev. Cardiol.* **8**, 103–113 (2011).

39.   McClure, R. S. *et al.* Epidemiology and management of thoracic aortic dissections and thoracic aortic aneurysms in Ontario, Canada: A population-based study. *J. Thorac. Cardiovasc. Surg.* **155**, 2254-2264.e4 (2018).

40.   Howard, D. P. J., Sideso, E., Handa, A. & Rothwell, P. M. Incidence, risk factors, outcome and projected future burden of acute aortic dissection. *Ann. Cardiothorac. Surg.* **3**, 278–284 (2014).

41.   Maëlle Robert et coll. Abdominal aortic aneurysms and acute aortic dissection: hospitalized patients and mortality.

42.   Pacini, D. *et al.* Acute aortic dissection: Epidemiology and outcomes. *Int. J. Cardiol.* **167**, 2806–2812 (2013).

43.   Strayer, R. J., Shearer, P. L. & Hermann, L. K. Screening, evaluation, and early management of acute aortic dissection in the ED. *Curr. Cardiol. Rev.* **8**, 152–7 (2012).

44. Lombardi, J. V. *et al.* Society for Vascular Surgery (SVS) and Society of Thoracic Surgeons (STS) reporting standards for type B aortic dissections. *J. Vasc. Surg.* **71**, 723–747 (2020).

45. Tran, T. P. & Khoynezhad, A. Current management of type B aortic dissection. *Vasc. Health Risk Manag.* **5**, 53–63 (2009).

46. http://www.aortarepair.com/type-a-aortic-dissection.html.

47. http://www.aortarepair.com/type-b-aortic-dissection.html.

48. Khan, I. A. & Nair, C. K. Clinical , Diagnostic , and Management Perspectives of Aortic Dissection *. *Chest* **122**, 311–328 (2002).

49. Booher, A. M. *et al.* The IRAD classification system for characterizing survival after aortic dissection. *Am. J. Med.* **126**, 730.e19-730.e24 (2013).

50. Garzón, G. *et al.* Endovascular stent-graft treatment of thoracic aortic disease. *Radiographics* **25**, (2005).

51. Pape, L. A. *et al.* Presentation, diagnosis, and outcomes of acute aortic dissection: 17-year trends from the international registry of acute aortic dissection. *J. Am. Coll. Cardiol.* **66**, 350–358 (2015).

52. Sueyoshi, E., Onitsuka, H., Nagayama, H., Sakamoto, I. & Uetani, M. Endovascular repair of aortic dissection and intramural hematoma : indications and serial changes. 1–6 (2014).

53. Fukui, T. Management of acute aortic dissection and thoracic aortic rupture. *J. Intensive Care* **6**, 1–8 (2018).

54. Olsson, C. *et al.* Mortality and reoperations in survivors operated on for acute type A aortic dissection and implications for catheter-based or hybrid interventions. *J. Vasc. Surg.* **58**, 333-339.e1 (2013).

55. Tang, G. H. L. *et al.* Surgery for acute type A aortic dissection in

octogenarians is justified. *J. Thorac. Cardiovasc. Surg.* **145**, S186–S190 (2013).

56.   https://www.spectrumhealthlakeland.org/lakeland-ear-nose-and-throat/ent-health-library/Content/135/72/.

57.   Trimarchi, S. *et al.* Contemporary results of surgery in acute type a aortic dissection: The International Registry of Acute Aortic Dissection experience. *J. Thorac. Cardiovasc. Surg.* **129**, 112–122 (2005).

58.   Nishida, H. *et al.* A systematic approach to improve the outcomes of type A aortic dissection. *J. Thorac. Cardiovasc. Surg.* **154**, 89-96.e1 (2017).

59.   Nienaber, C. A. *et al.* Randomized comparison of strategies for type B aortic dissection: The INvestigation of STEnt grafts in aortic dissection (INSTEAD) trial. *Circulation* **120**, 2519–2528 (2009).

60.   Swerdlow, N. J., Wu, W. W. & Schermerhorn, M. L. Open and endovascular management of aortic aneurysms. *Circ. Res.* **124**, 647–661 (2019).

61.   di Tommaso, L., Giordano, R., di Tommaso, E. & Iannelli, G. Endovascular treatment for chronic type B aortic dissection: Current opinions. *J. Thorac. Dis.* **10**, S978–S982 (2018).

62.   Nienaber, C. A. *et al.* Endovascular repair of type B aortic dissection: Long-term results of the randomized investigation of stent grafts in aortic dissection trial. *Circ. Cardiovasc. Interv.* **6**, 407–416 (2013).

63.   Matsumura, J. S. *et al.* Five-year results of thoracic endovascular aortic repair with the Zenith TX2. *J. Vasc. Surg.* **60**, 1–10 (2014).

64.   Cambria, R. P. *et al.* From the Society for Vascular Surgery A multicenter clinical trial of endovascular stent graft repair of acute catastrophes of

the descending thoracic aorta. *YMVA* **50**, 1255-1264.e4 (2009).

65. O'Brien, F. J. Biomaterials & scaffolds for tissue engineering. *Mater. Today* **14**, 88–95 (2011).

66. A.K. Bajpai, Jaya Bajpai, Rajesh Kumar Saini, Priyanka Agrawal, A. T. *Smart Biomaterials Devices: Polymers in Biomedical Sciences*. (2016).

67. Chan, B. P. & Leong, K. W. Scaffolding in tissue engineering: General approaches and tissue-specific considerations. *Eur. Spine J.* **17**, (2008).

68. Chen, G., Ushida, T. & Tateishi, T. Scaffold design for tissue engineering. *Macromol. Biosci.* **2**, 67–77 (2002).

69. Smith, L. A. & Ma, P. X. Nano-fibrous scaffolds for tissue engineering. *Colloids Surfaces B Biointerfaces* **39**, 125–131 (2004).

70. Li, X. *et al.* 3D-printed biopolymers for tissue engineering application. *Int. J. Polym. Sci.* **2014**, (2014).

71. Siddiqui, N., Asawa, S., Birru, B., Baadhe, R. & Rao, S. PCL-Based Composite Scaffold Matrices for Tissue Engineering Applications. *Mol. Biotechnol.* **60**, 506–532 (2018).

72. Wu, Y. *et al.* The regeneration of macro-porous electrospun poly(ε-caprolactone) vascular graft during long-term in situ implantation. *J. Biomed. Mater. Res. - Part B Appl. Biomater.* **106**, 1618–1627 (2018).

73. Lee, M. *et al.* Biofunctionalization of electrospun PCL-based scaffolds with perlecan domain IV peptide to create a 3-D pharmacokinetic cancer model. *Biomaterials* **31**, 5700–5718 (2010).

74. Malikmammadov, E., Tanir, T. E., Kiziltay, A., Hasirci, V. & Hasirci, N. *PCL and PCL-based materials in biomedical applications*. *Journal of Biomaterials Science, Polymer Edition* vol. 29 (Taylor & Francis, 2018).

75. Hao, J., Yuan, M. & Deng, X. Biodegradable and biocompatible

nanocomposites of poly(ε-caprolactone) with hydroxyapatite nanocrystals: Thermal and mechanical properties. *J. Appl. Polym. Sci.* **86**, 676–683 (2002).

76. Abedalwafa, M., Wang, F., Wang, L. & Li, C. Biodegradable Poly-epsilon-caprolactone (PCL) for tissue engineering applications: A review. *Rev. Adv. Mater. Sci.* **34**, 123–140 (2013).

77. Balà, N. Master thesis, Development of a poplymeric patch to promote migration and proliferation of vascular cells. *IQS URL* (2017).

78. Aranda, A. Master Thesis, Design and prototyping of a catheter tip for endovascular applications. (2018).

79. Félétou, M. *The Endothelium Part 1: Multiple Functions of the Endothelial Cells - Focus on Endothelium-Derived Vasoactive Mediators*. (Morgan & Claypool Life Sciences Publishers, 2011). doi:10.4199/C00031ED1V01Y201105ISP019.

80. https://open.oregonstate.education/aandp/chapter/10-7-smooth-muscle-tissue/.

81. Xie, J., MacEwan, M. R., Schwartz, A. G. & Xia, Y. Electrospun nanofibers for neural tissue engineering. *Nanoscale* **2**, 35–44 (2010).

82. Ferreira, J. L., Gomes, S., Henriques, C., Borges, J. P. & Silva, J. C. Electrospinning polycaprolactone dissolved in glacial acetic acid: Fiber production, nonwoven characterization, and in Vitro evaluation. *J. Appl. Polym. Sci.* **131**, 37–39 (2014).

83. Shi, X., Zhou, W., Ma, D., Ma, Q. & Bridges, D. Electrospinning of Nanofibers and Their Applications for Electrospinning of Nanofibers and Their Applications for Energy Devices. *J. Nanomater.* **2015**, (2015).

84. Qin, X. & Wu, D. Effect of different solvents on poly(caprolactone)(PCL)

electrospun nonwoven membranes. *J. Therm. Anal. Calorim.* **107**, 1007–1013 (2012).

85.   Shah Hosseini, N. & Khenoussi, N. *Structuring of electrospun nanofiber mats by 3D printing methods*. *Electrospun Materials for Tissue Engineering and Biomedical Applications: Research, Design and Commercialization* (Elsevier Ltd., 2017). doi:10.1016/B978-0-08-101022-8.00003-X.

86.   Huang, C. Y., Hu, K. H. & Wei, Z. H. Comparison of cell behavior on pva/pva-gelatin electrospun nanofibers with random and aligned configuration. *Sci. Rep.* **6**, 1–8 (2016).

87.   Xue, J., Xie, J., Liu, W. & Xia, Y. Electrospun Nanofibers: New Concepts, Materials, and Applications. *Acc. Chem. Res.* **50**, 1976–1987 (2017).

88.   Baker, S. R., Banerjee, S., Bonin, K. & Guthold, M. Determining the mechanical properties of electrospun poly-ε-caprolactone (PCL) nanofibers using AFM and a novel fiber anchoring technique. *Mater. Sci. Eng. C* 203–212 (2015) doi:10.1016/j.msec.2015.09.102.

89.   Katsogiannis, K. A. G., Vladisavljević, G. T. & Georgiadou, S. Porous electrospun polycaprolactone (PCL) fibres by phase separation. *Eur. Polym. J.* **69**, 284–295 (2015).

90.   Zargham, S., Bazgir, S., Tavakoli, A., Rashidi, A. S. & Damerchely, R. The effect of flow rate on morphology and deposition area of electrospun nylon 6 nanofiber. *J. Eng. Fiber. Fabr.* **7**, 42–49 (2012).

91.   Luo, C. J., Nangrejo, M. & Edirisinghe, M. A novel method of selecting solvents for polymer electrospinning. *Polymer (Guildf).* **51**, 1654–1662 (2010).

92.   Olaru, N. & Olaru, L. Electrospinning of cellulose acetate phthalate from different solvent systems. *Ind. Eng. Chem. Res.* **49**, 1953–1957

(2010).

93.   Dorati, R. *et al.* The Effect of Process Parameters on Alignment of Tubular Electrospun Nanofibers for Tissue Regeneration Purposes. *J. Drug Deliv. Sci. Technol.* **58**, 101781 (2020).

94.   Luo, C. J., Stride, E. & Edirisinghe, M. Mapping the influence of solubility and dielectric constant on electrospinning polycaprolactone solutions. *Macromolecules* **45**, 4669–4680 (2012).

95.   https://depts.washington.edu/eooptic/linkfiles/dielectric_chart%5B1%5D.pdf.

96.   Brewster, L. *Principles of Tissue Engineering - Blood Vessels*. (2007). doi:10.1016/b978-012370615-7/50043-3.

97.   de Beaufort, H. W. L. *et al.* Comparative Analysis of Porcine and Human Thoracic Aortic Stiffness. *Eur. J. Vasc. Endovasc. Surg.* **55**, 560–566 (2018).

98.   Okutan, N., Terzi, P. & Altay, F. Affecting parameters on electrospinning process and characterization of electrospun gelatin nanofibers. *Food Hydrocoll.* **39**, 19–26 (2014).

99.   Sánchez-Quesada, C., López-Biedma, A., Toledo, E. & J. Gaforio, J. Squalene Stimulates a Key Innate Immune Cell to Foster Wound Healing and Tissue Repair. *Evidence-Based Complement. Altern. Med.* (2018) doi:10.1155/2018/9473094.

100.   Font, C. Master Thesis, Fabricación de scaffolds mediante la tecnica del electrospinning. (2017).

101.   Fox, C. B. Squalene emulsions for parenteral vaccine and drug delivery. *Molecules* **14**, 3286–3312 (2009).

102. Liu, K. *et al.* A bio-inspired high strength three-layer nanofiber vascular graft with structure guided cell growth. *J. Mater. Chem. B* **5**, 3758–3764 (2017).

103. Jiao, Y. & Cui, F. Surface modification of polyester biomaterials for tissue engineering. **24**,.

104. Balcells, M., Martorell, J., Chitalia, V., Cardoso, A. A. & Edelman, E. R. Smooth muscle cells orchestrate the endothelial cell response to flow and Injury. **121**, 2192–2199 (2011).

105. Tahir, H. *et al.* Endothelial repair process and its relevance to longitudinal neointimal tissue patterns: Comparing histology with in silico modelling. *J. R. Soc. Interface* **11**, (2014).

106. Clopath, P., Müller, K., Stäubli, W. & Bürk, R. R. In vivo and in vitro studies on Endothelial Regeneration. *Haemostasis* 149–157 (1979).

107. Pankov, R. & Kenneth, M. Fibronectin at a glance. 3861–3863 (2002) doi:10.1242/jcs.00059.

108. Wierzbicka-patynowski, I. & Schwarzbauer, J. E. The ins and outs of fibronectin matrix assembly. (2003) doi:10.1242/jcs.00670.

109. To, W. S. & Midwood, K. S. Plasma and cellular fibronectin : distinct and independent functions during tissue repair. 1–17 (2011).

110. Manabe, R., Oh-e, N., Maeda, T., Fukuda, T. & Sekiguchi, K. Modulation of Cell-adhesive Activity of Fibronectin by the Alternatively Spliced EDA Segment. **139**, 295–307 (1997).

111. Hielscher, A., Ellis, K., Qiu, C., Porterfield, J. & Gerecht, S. Fibronectin deposition participates in extracellular matrix assembly and vascular morphogenesis. *PLoS One* **11**, 1–27 (2016).

112. https://www.sigmaaldrich.com/ES/es/technical-

documents/technical-article/cell-culture-and-cell-culture-analysis/mammalian-cell-culture/fibronectin.

113.   Ishihara, J. *et al.* Laminin heparin-binding peptides bind to several growth factors and enhance diabetic wound healing. *Nat. Commun.* **9**, (2018).

114.   Hamill, K. J., Kligys, K., Hopkinson, S. B. & Jones, J. C. R. Laminin deposition in the extracellular matrix: A complex picture emerges. *J. Cell Sci.* **122**, 4409–4417 (2009).

115.   Yousif, L. F., Russo, J. Di & Sorokin, L. Laminin isoforms in endothelial and perivascular basement membranes. 101–110 (2013).

116.   Boateng, S. Y. *et al.* RGD and YIGSR synthetic peptides facilitate cellular adhesion identical to that of laminin and fibronectin but alter the physiology of neonatal cardiac myocytes. *Am. J. Physiol. - Cell Physiol.* **288**, 30–38 (2005).

117.   Raiter, A. *et al.* Angiogenic peptides improve blood flow and promote capillary growth in a diabetic and ischaemic mouse model. *Eur. J. Vasc. Endovasc. Surg.* **40**, 381–388 (2010).

118.   Robinet, A. *et al.* Elastin-derived peptides enhance angiogenesis by promoting endothelial cell migration and tubulogenesis through upregulation of MT1-MMP. *J. Cell Sci.* **118**, 343–356 (2005).

119.   Ruoslahti, E. RGD and Other Recognition Sequences for Integrins. *Annu. Rev. Cell Dev. Biol.* **12**, 697–715 (1996).

120.   Kapp, T. G. *et al.* A comprehensive evaluation of the activity and selectivity profile of ligands for RGD-binding integrins. *Sci. Rep.* **7**, 1–13 (2017).

121.   Takada, Y., Ye, X. & Simon, S. The integrins. *Genome Biol.* **8**, (2007).

122.   Kim, Y. Y. *et al.* Laminin peptide YIGSR enhances epidermal development of skin equivalents. *J. Tissue Viability* **27**, 117–121 (2018).

123.   Szychowski, K. A., Wójtowicz, A. K. & Gmiński, J. Impact of Elastin-Derived Peptide VGVAPG on Matrix Metalloprotease-2 and -9 and the Tissue Inhibitor of Metalloproteinase-1, -2, -3 and -4 mRNA Expression in Mouse Cortical Glial Cells In Vitro. *Neurotox. Res.* **35**, 100–110 (2019).

124.   Floquet, N. *et al.* Structural characterization of VGVAPG, an elastin-derived peptide. *Biopolym. - Pept. Sci. Sect.* **76**, 266–280 (2004).

125.   Yan, D. *et al.* Plasma treatment of electrospun PCL random nanofiber meshes (NFMs) for biological property improvement. 1–10 (2012) doi:10.1002/jbm.a.34398.

126.   Ko, Y., Choi, D., Jung, S. & Kim, B. Characteristics of Plasma Treated Electrospun Polycaprolactone (PCL) Nanofiber Scaffold for Bone Tissue Engineering. **15**, 192–195 (2015).

127.   Ramkumar, M. C., Cools, P., Arunkumar, A., De Geyter, N. & Morent, R. *Functionalised Cardiovascular Stents*. (2018). doi:10.1016/B978-0-08-100496-8.00009-3.

128.   Troughton, M. *Handbook of Plastics Joining*. (2008).

129.   Ebnesajjad, S. & H. Landrock, A. *Adhesives Technology Handbook*. (Elsevier Science, 2014).

130.   Rokutan, H., Anker, S. D. & Springer, J. In vivo models of cardiac diseases: Application to drug development and screening. *Expert Opin. Drug Discov.* **5**, 65–78 (2010).

131.   Wood, M. W. & Hart, L. A. Selecting appropriate animal models and strains: Making the best use of research, information and outreach.

Aatex **14**, 303–306 (2007).

132. Balakumar, P., Singh, A. P. & Singh, M. Rodent models of heart failure. *J. Pharmacol. Toxicol. Methods* **56**, 1–10 (2007).

133. Egido, J. *et al.* Animal models of cardiovascular diseases. *J. Biomed. Biotechnol.* **2011**, (2011).

134. Jiang, D. S., Yi, X., Zhu, X. H. & Wei, X. Experimental in vivo and ex vivo models for the study of human aortic dissection: Promises and challenges. *Am. J. Transl. Res.* **8**, 5125–5140 (2016).

135. Qing, K. X. *et al.* Ex-vivo haemodynamic models for the study of Stanford type B aortic dissection in isolated porcine aorta. *Eur. J. Vasc. Endovasc. Surg.* **44**, 399–405 (2012).

136. Sommer, G. *et al.* Mechanical strength of aneurysmatic and dissected human thoracic aortas at different shear loading modes. *J. Biomech.* **49**, 2374–2382 (2016).

137. McMillen, C. The sheep - an ideal model for biomedical research? *Anzccart News* **14**, 1–4 (2001).

138. Lysgaard Poulsen, J., Stubbe, J. & Lindholt, J. S. Animal Models Used to Explore Abdominal Aortic Aneurysms: A Systematic Review. *Eur. J. Vasc. Endovasc. Surg.* **52**, 487–499 (2016).

139. Okuno, T. *et al.* Endovascular creation of aortic dissection in a swine model with technical considerations. *J. Vasc. Surg.* **55**, 1410–1418 (2012).

140. https://www.nibib.nih.gov/science-education/science-topics/computed-tomography-ct.

141. Evangelista, A. *et al.* Role of entry tear size in type B aortic dissection. *Ann. Cardiothorac. Surg.* **3**, 403–405 (2014).

142. Ali, S., Athar, M. & Ahmed, S. M. Basics of CPB. *Indian J. Anaesth.* **49**, 257–262 (2019).

143. Sheikh, Z., Brooks, P. J., Barzilay, O., Fine, N. & Glogauer, M. Macrophages, foreign body giant cells and their response to implantable biomaterials. *Materials (Basel).* **8**, 5671–5701 (2015).

144. Anderson, J. M., Rodriguez, A. & Chang, D. T. Foreign body reaction to biomaterials. *Semin. Immunol.* **20**, 86–100 (2008).

145. http://wiki.dtonline.org/index.php/Young%27s_Modulus.

146. Iliopoulos, D. C. *et al.* Regional and directional variations in the mechanical properties of ascending thoracic aortic aneurysms. *Med. Eng. Phys.* **31**, 1–9 (2009).

147. Khanafer, K. *et al.* Determination of the elastic modulus of ascending thoracic aortic aneurysm at different ranges of pressure using uniaxial tensile testing. *J. Thorac. Cardiovasc. Surg.* **142**, 682–686 (2011).

148. Spendley, W., Hext, G. R. & Himsworth, F. R. Sequential Application of Simplex Designs in Optimisation and Evolutionary Operation. *Technometrics* **4**, 441–461 (1962).

149. Michałowski, T., Rymanowski, M. & Pietrzyk, A. A simple approach to the simplex method. *Chem. Analityczna* **53**, 743–752 (2008).

150. Bezerra, M. A. *et al.* Simplex optimization: A tutorial approach and recent applications in analytical chemistry. *Microchem. J.* **124**, 45–54 (2016).